



Supplementary Material for

Revealing enzyme functional architecture via high-throughput microfluidic enzyme kinetics

C. J. Markin, D. A. Mokhtari, F. Sunden, M. J. Appel, E. Akiva, S. A. Longwell,
C. Sabatti, D. Herschlag*, P. M. Fordyce*

*Corresponding author. Email: herschla@stanford.edu (D.H.); pfordyce@stanford.edu (P.M.F.)

Published 23 July 2021, *Science* **373**, eabf8761 (2021)
DOI: 10.1126/science.abf8761

This PDF file includes:

Materials and Methods
Supplementary Text
Figs. S1 to S70
Tables S1 to S17
References

Other Supplementary Material for this manuscript includes the following:

(available at science.sciencemag.org/content/373/6553/eabf8761/suppl/DC1)

MDAR Reproducibility Checklist
Data File S1 as a separate .csv file
Data File S2 as a separate .pdf file

Contents

Materials and Methods	4
HT-MEK device fabrication	4
Construct and library generation	4
Optics, pneumatics, and custom software	8
Expressing and purifying enzymes on HT-MEK	9
Imaging and quantification of expressed enzymes	12
Synthesis of fluorogenic cMUP and MecMUP substrates	13
Multi-Tier measurement strategy	14
<i>In vivo</i> expression, purification, and assay of control WT PafA and active site mutants	15
Measuring cMUP hydrolysis on-chip	15
Analysis and quality control of cMUP hydrolysis measurements	17
Aggregating cMUP hydrolysis data across experiments	20
Testing statistical significance of measured effects	23
Probing for equilibrium unfolding, changes in Zn^{2+} affinity, and changes in enzymatic pK_a	24
Measuring methyl phosphate hydrolysis using HT-MEK	25
Measuring enzyme concentration for MeP assays	26
Quantifying enzyme activity as a function of temperature and $[Zn^{2+}]$ during expression	28
Characterization of the misfolded state	29
Deconvolving mutational effects on folding and catalysis	32
Measuring hydrolysis of the non-cognate substrate MecMUP	33
Functional Component 1: Effects through the O2 phosphoryl oxygen atom	34
Determination of residues within each K162/R164 interaction shell	35
Determination of surface-exposed residues and calculation of depth from surface	36
Measuring phosphate inhibition constants using HT-MEK	36
PafA phylogenetic analysis	38
Supplementary Text	41
S1. Equilibrium measurements to test if activity depends on [urea], $[Zn^{2+}]$, and pH	41
S2. Deriving the predicted relationship between k_{cat}/K_M for cMUP and MeP for PafA	43
S3. A two-state model of unfolding estimates mutational misfolding effects on f_a	44
S4. Estimating mutational effects on intrinsic catalytic parameters	44
S5. Identifying and classifying non-conserved auxiliary domains	45
S6. Estimating mutational effects on phospho-enzyme intermediate hydrolysis	46
S7. Evolutionary constraints revealed by comparisons between phylogeny and functional parameters	47
Figures S1 to S70	48

Tables S1 to S17	118
Captions for Auxiliary Supplementary Materials, Data S1 and S2	135
OSF Repository Data	136
References	137

Materials and Methods

HT-MEK device fabrication

Photolithographic mold production

Molding masters for flow and control layers of microfluidic devices were designed in AutoCAD (Autodesk, Inc.) and fabricated on 4" single-sided silicon test-grade wafers (University Wafer) using transparency masks printed at 30000 dpi (Fineline Imaging) via standard photolithography procedures (70, 71). Flow molds were composed of the following layers: (1) a ~5 μm uniform layer of SU-8 2005 (Microchem) covering the entire wafer surface to improve feature adhesion, (2) a ~15 μm layer of AZ50 XT (Capitol Scientific) subjected to a slow final hard bake to generate rounded valve features, and (3) a ~15 μm layer of SU-8 2015 (Microchem) to generate square flow channels. Control molds were composed of a single ~25 μm layer of SU-8 2025 (Microchem). All mask designs are available on our lab website (<http://www.fordycelab.com>).

PDMS device fabrication

Two layer "push-down" valved MITOMI polydimethylsiloxane (PDMS) devices (**Fig. S2**) were fabricated from molding masters largely as described previously (70). Prior to fabrication, silicon wafer molding masters were silanized via vapor deposition of trichloro(1H,1H,2H,2H-perfluorooctyl)silane (Sigma) for 10 min to prevent PDMS adhesion. To fabricate thick control layers, a 1:5 ratio of RTV 615 (R.S. Hughes) crosslinker:base was mixed using a THINKY centrifugal mixer for 3 min, degassed for 3 min at 4000 rpm, and then poured onto control molds positioned within an aluminum foil holder. After pouring, thick PDMS layers were degassed for ~1 h in a vacuum chamber under house vacuum. To fabricate thin flow layers, a 1:20 ratio of RTV 615 (R.S. Hughes) crosslinker:base was mixed in a THINKY centrifugal mixer for 3 min and then spin coated onto the flow mold (10 s ramp at 500 rpm, 133x acceleration; 75 s spin coating at 1725 rpm, 266x acceleration). Flow and control molds were subsequently baked at 80°C for 40 min and 60 min, respectively. After baking, the thick control layer was peeled off of the silicon wafer, individual devices were cut out of the layer using a scalpel, and control inlet holes were punched using a 20 gauge needle and a small drill press (Technical Innovations). Control layers were then aligned by eye to flow layers remaining on their molding master using a stereoscope and this entire assembly was baked for an additional 50 min. Fully baked devices were cut off of the flow wafer using a scalpel and stored for subsequent alignment to printed plasmid arrays, as described below. All fabrication was performed in the Stanford Microfluidics Foundry class 10,000 clean room.

Construct and library generation

WT and active site PafA-eGFP fusion construct generation

Wild-type PafA with truncated periplasmic signal peptide (UniProtKB/Swiss-Prot identifier Q9KJX5-1, residues 21–546 with Met start) was C-terminally tagged with enhanced

green fluorescent protein (eGFP) via a flexible glycine/serine linker (GGGSGGGGSG) and subcloned into the optimized PURExpress expression plasmid (referred to as the “DHFR control template” in the manufacturer protocol) (**Fig. S3** and **OSF Repository Data S1 (74)**; WT PafA-SerGlyLinker-eGFP nucleotide sequence and protein translation below).

WT PafA-SerGlyLinker-eGFP nucleotide coding sequence:

```

1   ATGCAAAAAACGAAT GCTGTACCAAGACCT AAACCTGTGGTAGGA CTGGTAGTTGATCAG ATGAGATGGGATTAT 75
76   CTTTACC GTTATTAT AGCAAGTATGGTGAA GGAGGTTTTAAGAGA ATGCTGAATACCGGG TATTCGTTAAATAAT 150
151  GTTCATATAGACTAT GTACCTACAGTAACT GCAATCGGACATACT TCAATTTTTACAGGT TCTGTTCCCTCCATC 225
226  CACGGAATTGCAGGA AACGATTGGTATGAT AAAGAATTAGGGAAA AGTGTTTACTGTACA TCTGATGAAACAGTA 300
301  CAACCGGTAGGAACT ACTTCTAACTCGGTT GGACAACATTACCCA AGAAACCTTTGGTCT ACTACGGTAACAGAT 375
376  CAGCTAGGTTTGCCA ACAAACTTTACTTCT AAGGTTGTGGGGGTC TCTCTGAAAGACAGA GCATCAATTCTGCCT 450
451  GCAGGGCACAACCCA ACAGGAGCATTFTGG TTCGATGATACTACA GGTAAAATTCATTACC AGTACATATTATACT 525
526  AAAGAATTACCTAAA TGGGTAAACGACTTT AATAATAAAAATGTT CCGGCTCAGTTGGTA GCTAATGGCTGGAAT 600
601  ACACTATTGCCATT AATCAGTATACAGAA AGCTCAGAAGATAAT GTGGAATGGGAAGGT TTATTAGGGAGTAAA 675
676  AAAACACCTACATTC CCTTATACAGATCTG GCTAAAGATTATGAA GCTAAAAAAGGATTA ATCCGTACTACACCA 750
751  TTTGGAAATACCTTA ACTCTTCAGATGGCA GATGCTGCAATTGAT GGTAACCAAATGGGA GTTGATGATATTACT 825
826  GACTTCCTTACAGTA AACCTTGCTTCAACG GATTATGTTGGACAC AACTTTGGTCCAAAC TCTATAGAAGTTGAG 900
901  GATACTTATCTGAGA TTAGACAGAGATTTG GCTGACTTCTTCAAT AACCTTGATAAAAAA GTTGGAAAAGGAAAC 975
976  TACCTTGTATTCCCT TCTGCGGATCATGGC GCTGCACATTCTGTG GGCTTTATGCAAGCA CATAAAATGCCAACA 1050
1051 GGCTTCTTTGTAGAA GATATGAAAAAAGAA ATGAACGCTAAGCTG AAGCAAAAATTCGGT GCTGATAATATAATT 1125
1126 GCAGCTGCGATGAAC TATCAGGTTTATTTT GACAGAAAGGTTTTA GCAGACAGCAAATTA GAATTGGATGACGTA 1200
1201 AGAGATTATGTAATG ACAGAACTTAAAAAA GAGCCATCAGTTCTT TATGTTCTTAGCAGG GATGAAATCTGGGAA 1275
1276 TCGTCTATTCGGAA CCGATAAAGTCCAGA GTAATCAATGGTTAT AACTGGAAAAGAAGC GGAGATATTCAGATC 1350
1351 ATTTCTAAAGACGGA TATCTTTCAGCATAT TCCAAAAAAGGGACA ACACACAGTGATGG AACTCTTATGATTCA 1425
1426 CATATTCCTTTACTC TTTATGGGGTGGGGT ATCAACAGGGGAGAG TCCAATCAGCCATAC CATATGACGGATATT 1500
1501 GCACCAACTGTTTCA TCATTACTTAAAATT CAGTTCCTAGTGGT GCTGTAGGTAAACCA ATTACCGAAGTTATA 1575
1576 GGAAGAGGAGGAGGG TCTGGGGGAGGAGGC AGTGGCATGGTGAGC AAGGGCGAGGAGCTG TTCACCGGGTGGTG 1650
1651 CCCATCCTGGTCGAG CTGGACGGCGACGTA AACGGCCACAAGTTC AGCGTGTCGGCGAG GGCAGGGCGATGCC 1725
1726 ACCTACGGCAAGCTG ACCCTGAAGTTCATC TGCACCACCGGCAAG CTGCCCGTCCCTGG CCCACCTCGTGACC 1800
1801 ACCCTGACCTACGGC GTGCAGTGCTTCAGC CGCTACCCCGACCAC ATGAAGCAGCACGAC TTCTTCAAGTCCGCC 1875
1876 ATGCCCGAAGGCTAC GTCCAGGAGCGCACC ATCTTCTTCAAGGAC GACGGCAACTACAAG ACCCGCGCCGAGGTG 1950
1951 AAGTTCGAGGGCGAC ACCCTGGTGAACCGC ATCGAGCTGAAGGGC ATCGACTTCAAGGAG GACGGCAACATCTG 2025
2026 GGGCACAAGCTGGAG TACAACACAACAGC CACAACGTCTATATC ATGGCCGACAAGCAG AAGAACGGCATCAAG 2100
2101 GTGAACTTCAAGATC CGCCACAACATCGAG GACGGCAGCGTGCAG CTCGCCGACCACTAC CAGCAGAACACCCCC 2175
2176 ATCGGCGACGGCCCC GTGCTGCTGCCCGAC AACCACTACCTGAGC ACCCAGTCCGCCCTG AGCAAAGACCCCAAC 2250
2251 GAGAAGCGCATCAC ATGGTCTGCTGGAG TTCGTGACCGCCGCC GGGATCACTCTCGGC ATGGACGAGCTGTAC 2325
2326 AAA 2328

```

WT PafA-SerGlyLinker-eGFP protein translation:

```
1  MQKTNVAVRP KLVVGLVVDQ MRWDYLYRYY SKYGEGGFKR MLNTGYSLNN VHIDYVPTVT 60
61  AIGHTSIFTG SVPSIHGIAG NDWYDKELGK SVYCTSDETV QPVGTTNSV GQHSPRNLWS 120
121 TTVDQLGLA TNFTSKVVG V SLKDRASILP AGHNPTGAFW FDDTTGKFIT STYYTKELPK 180
181 WVNDFNKNV PAQLVANGWN TLLPINQYTE SSEDNVEWEG LLGSKKTPF PYTDLAKDYE 240
241 AKKGLIRTP FGNLTTLQMA DAAIDGNQMG VDDITDFTLV NLASTDYVGH NFGPNSIEVE 300
301 DTYLRLDRDL ADFFNLDKK VGKGNLVFL SADHGAHSV GFMQAHKMPT GFFVEDMKKE 360
361 MNAKLRKQFQ ADNI IAAAMN YQVYFDRKVL ADSKLELDDV RDYVMTELK EPVLYVLST 420
421 DEIWESSIPE PIKSRVINGY NWKRSQDIQI ISKDGYSAY SKKGTTHSVW NSYDSHIPL 480
481 FMGWGIKQGE SNQPYHMTDI APTVSSLLKI QFPGAVGKP ITEVIGRGGG SGGGGSGMVS 540
541 KGEELFTGVV PILVELDGDV NGHKFSVSGE GEGDATYGKL TLKFICTTGK LPVPWPTLVT 600
601 TLYYGVQCF S RYPDHMQHD FFKSAMPEGY VQERTIFFKD DGNYKTRAEV KFEQDTLVNR 660
661 IELKGIDFKE DGNILGHKLE YNYNHNVYI MADKQKNGIK VNFKIRHNE DGSVQLADHY 720
721 QQNTPIGDGP VLLPDNHYS TQSALSKDPN EKRDMVLE FVTAAGITLG MDELYK 776
```

Generation of scanning mutant libraries

Mutant libraries were generated using QuikChange site-directed mutagenesis (Agilent Technologies, Inc.) in a 96-well plate format, detailed below and diagrammed in **Fig. S18**).

Mutagenic primer design Mutagenic primers optimized for QuikChange site-directed mutagenesis were designed in batch using a custom script (<https://github.com/FordyceLab/designQuikChangePrimers>). Given a desired single-residue mutation, the script chooses an optimal mutant codon based on the minimum number of nucleotide changes required and generates a series of potential primers 30–45 nt in length with the mutation site <2 nt from the center of the primer. The algorithm then scores each primer based on its annealing temperature (T_m , calculated using Primer3) (75), propensity to form hairpins, and the presence or absence of G or C nucleotides at either end. To compute a final primer score, each of these parameters was weighted by its relative importance for successful primer design, with the T_m weighted most heavily. T_m scores were assigned a maximum value for $T_m > 78^\circ\text{C}$, a half-maximal score for $77^\circ\text{C} < T_m < 78^\circ\text{C}$, and a score that linearly decreased to zero for $T_m < 77^\circ\text{C}$. The full code, weights used, and associated comments are available in the GitHub repository.

Optimized primers were ordered in 96-well plates at 10 nmol synthesis scale and purified using standard desalting (Integrated DNA Technologies, Inc.). Forward and reverse primers were premixed and normalized to 6 nmol per well. Primer pairs were re-suspended in 120 μL Milli-Q water and then diluted to working stock solutions at 1.25 μM for use in downstream PCR reactions.

PCR mutagenesis and digestion of template DNA Mutagenic PCRs were performed in 96-well PCR plates using a modified version of the QuikChange site-directed mutagenesis protocol (Agilent Technologies, Inc.). First, we added 6 μL of a 1.25 μM working primer solution to each well. Next, we added all additional components of the reaction (including PfuTurbo AD polymerase; Agilent Technologies Inc., catalog no. 600259) from a master mix prepared on ice and added immediately before thermocycling. Final reactions contained 2.5 μL 10X Cloned Pfu DNA polymerase reaction buffer AD, 300 nM forward and reverse primer, 200 μM dNTPs, 5% (v/v) DMSO, 2.5–5.0 ng template plasmid, and 1.25

U PfuTurbo AD polymerase in a total volume of 25 μ L. Reactions were heated to 94°C for 60 s and then cycled 14 times using the following parameters: a 60 s denaturation step at 95°C, a 60 s annealing step at 55°C, and a 12 min extension step at 68°C. After cycling, a final elongation step was performed for 60 s at 68°C and reactions were cooled to 4°C. For reactions that did not yield the desired mutation (assessed by Sanger sequencing, described below), repeated reactions were performed with an increased annealing temperature of 60°C. To digest remaining template DNA after PCR, we added 20 U of DpnI (New England Biolabs Inc., catalog no. R0176S) and 2 μ L CutSmart buffer (New England Biolabs Inc., catalog no. B7204S) to 10 μ L of PCR reaction and incubated at 37°C overnight.

Transformation and plasmid purification For bacterial transformation of mutant plasmids, we added 1 μ L of DpnI-digested plasmid to 5 μ L of ice-cold NEB 5-alpha competent *E. coli* (high efficiency; New England Biolabs Inc., catalog no. C2987). Cells were incubated with DNA on ice for 30 min, heat-shocked for 30 s at 42°C in a thermocycler, and then recovered on ice for 2 min. Outgrowth at 37°C was carried out for >1 h in 300 μ L SOC medium (New England Biolabs Inc., catalog no. B9020S) while shaking. We then plated the entire volume of outgrowth solution for each mutagenesis reaction on an LB agar plate containing either 100 μ g/mL ampicillin or 50 μ g/mL carbenicillin and incubated overnight at 37°C. A well-isolated single colony was picked from each plate and used to inoculate 5–10 mL of LB broth containing the same concentration of antibiotic. Plates with more than one colony were stored at 4°C in case picking additional colonies was necessary, as discussed below. Following overnight growth at 37°C, cells were pelleted at 1800 \times g for 10 min in an Eppendorf 5810R centrifuge. Plasmid DNA from cell pellets was either purified immediately or the pellet was frozen and stored at –20°C for later purification. To minimize the risk of contamination between mutants, all plasmid purifications were carried out individually using commercially available spin miniprep kits (either a QIAprep spin miniprep kit, Qiagen, catalog no. 27104, or GeneJet plasmid miniprep kit, ThermoFisher Scientific, catalog no. K0502).

Confirmation of desired mutation by Sanger sequencing Prior to mutagenesis, we sequenced the full-length (~2 kb) wild-type PafA-eGFP template construct for all stock solutions to ensure that no unwanted mutations were propagated to the entire library due to errors in the template DNA. After mutagenesis, each mutant was confirmed by Sanger sequencing using a sequencing primer designed to cover the region containing the putative mutation. While the majority of reactions (~75%) were successful on the first attempt, we encountered 3 types of unsuccessful outcomes: (1) lack of transformants after PCR and digestion, (2) transformants that harbored either the wild-type plasmid or an unanticipated mutation in the primer region (presumably due to a DNA synthesis error), or (3) a mixture of wild-type and mutant plasmids within a single colony, evident as mixed peaks in the Sanger sequencing chromatogram. In cases without transformants, we redesigned primers and/or attempted new PCR reactions using a different annealing temperature. For cases with transformants but not the correct mutation, we picked and sequenced additional colonies two or three additional times; if still unsuccessful, we redesigned mutagenic primers and began the process again.

Probability of incorporating an unwanted mutation outside of the sequencing read

As PfuTurbo is a high-fidelity polymerase with an error rate of 1.3×10^{-6} mutations/bp (76), the probability of the polymerase introducing an error in the PafA-eGFP construct outside of the primer region is approximately 0.003 per mutant (0.3%). As a result, in the course of making the 1036 mutants in this work, we expect approximately 3 errors in the entire library. Given that many nucleotide mutations would be synonymous, this provides an upper bound on the expected number of unwanted amino acid substitutions within the library.

Optics, pneumatics, and custom software

Imaging setup We imaged devices using a Nikon Ti-S Microscope equipped with a motorized XY stage (Applied Scientific Instrumentation, MS-2000 XYZ stage), cMOS camera (Oxford Instruments, Andor Zyla 4.2), solid-state light source (Lumencor, SOLA SE Light Engine), and automated filter turret equipped with an eGFP filter set (Chroma Technology Corp., part no. 49002), DAPI filter set (Semrock Inc., catalog no. DAPI-1160B-NTE), and a custom “PBP” filter set (Semrock Inc., 427/10 bandpass excitation filter, catalog no. FF01-427/10-25; 470/22 bandpass emission filter, catalog no. FF01-470/22-25; 442 nm dichroic beamsplitter, catalog no. DI03-R442-T1- 25X36; mounted in a TE2000 filter cube, catalog no. NTE). All imaging was performed using a 4X objective (CFI Plan Apochromat λ 4X NA 0.20, Nikon) at 2x2 binning (1024x1024 pixels) with exposure times as follows: eGFP, 500 ms; DAPI, 50 ms or 200 ms; PBP, 100 ms. Apparatus temperatures were measured throughout assays using a thermistor sensor (Thorlabs Inc., catalog no. TSP01, data logger; catalog no. TSP-TH NTC, external thermistor).

Pneumatic control Microfluidic devices were run using a custom-built pneumatic manifold (73) with pneumatic valve state controlled by custom open-source software (<https://github.com/FordyceLab/RunPack>).

Hardware automation and image processing software To automate device valve actuation, reagent flow, and image acquisition during HT-MEK experiments, we developed a custom, publicly-available Python package (<https://github.com/FordyceLab/RunPack>). This package provides an extensible unified hardware interface for imaging and stage control via the μ Manager (77) *MMCore* Python API; valve control using AcqPack, an in-house package for actuation of the HT-MEK WAGO-controlled pneumatic apparatus (<https://pypi.org/project/acqpack>) (78); and temperature measurement using PyVISA (<https://pypi.org/project/PyVISA/>). Images were processed using a publicly-available in-house image processing package written in Python (<https://github.com/FordyceLab/ProcessingPack>).

We analyzed images to yield progress curves and kinetic and thermodynamic binding constants using a custom suite of Mathematica notebooks (Wolfram Research, Inc.), available at https://github.com/FordyceLab/HT-MEK_KineticThermodynamicFitting. Data from each device was initially processed individually and then replicates across multiple devices

were combined and normalized using an additional notebook (*cf. Multi-Tier measurement strategy*, below). Summary CSV files containing the data from each experiment, and for each mutant across experiments, are available in the OSF Repository Data (<https://doi.org/10.17605/OSF.IO/QRN3C>) (74). Summary PDF files containing summary plots are available on the Fordyce Lab website (<http://www.fordycelab.com/publication-data>).

Expressing and purifying enzymes on HT-MEK

Printing plasmid library and aligning the device

Sequence-validated plasmid solutions were transferred directly into a series of 96-well plates for storage and array printing. For each plate, we generated a series of “daughter” plates by diluting 20 μL of each DNA solution from the “parent” 96-well plate to a final volume of 50 μL with Milli-Q water. For printing, DNA solutions (10 μL from each well of the daughter plates) were transferred from 96-well to 384-well plates using a Biomek FX Automated Workstation (Beckman Coulter, model A31843). After transfer, all 384-well plate solutions were evaporated to dryness and the DNA was re-suspended in 15 μL of 1% (w/v) BSA (UltraPure, ThermoFisher Scientific, catalog no. AM2616), 12 mg/mL trehalose dihydrate (Sigma Life Science, catalog no. T9531), and 200 mM NaCl (Sigma Life Science, catalog no. 71376). Final plasmid DNA concentrations in the 384-well plate ranged from ~ 40 –100 ng/ μL .

Plasmid DNA arrays were printed in tandem (two per slide) on custom 2" x 3" epoxysilane-coated slides (ThermoFisher Scientific SuperChip) using a custom microarrayer fitted with 75 μm silicon tips (Parallel Synthesis Technologies, catalog no. SMT-S75). To prevent carry over between spots on the array, we washed silicon tips two times after depositing each mutant for 10 s in hot water ($>70^\circ\text{C}$) followed by 8 s of drying under vacuum. After printing, PDMS devices were manually aligned to DNA arrays under a stereo microscope and then bonded to the slides for 12 h at 95°C on an aluminum hot plate (Torrey Pines Scientific). Device alignment was performed in the Stanford Microfluidics Foundry class 10,000 clean room to minimize the risk of particulates interfering with device function.

Surface patterning for enzyme immobilization

Surface functionalization was carried out largely as described previously (14), with several critical modifications (**Fig. S4**). Initial flow and control line pressures were set to 32 and 3–4 psi, respectively. To prevent premature solubilization of the DNA spots from osmotic transfer of water from the control layer, we filled control lines with a 0.55 M NaCl solution. To begin surface functionalization, the Button and Neck valves were pressurized (closed) to prevent solubilization of the plasmid DNA spots and protect Buttons and areas beneath them from fluid flow, respectively. To passivate PDMS walls and the epoxysilane surface outside of the Button valve, we introduced a 5 mg/mL BSA solution (ThermoFisher Scientific, catalog no. AM2616) throughout all channels. Solutions introduced into the device were initially primed through the inlet tree and directed to waste for ~ 5 min to purge any

air from the sample lines and inlet. After this initial purge step, solutions were flushed through the chip for 30 min with the Neck and Button valves pressurized (closed); between injections, we flowed 1X phosphate buffered saline (PBS, ThermoFisher Scientific, catalog no. 10010023) for 10–15 min to fully wash device channels. To selectively functionalize slide surfaces beneath the Button valve for recruitment and surface-immobilization of eGFP-tagged enzymes, we introduced a 2 mg/mL solution of biotinylated BSA (bBSA; ThermoFisher Pierce, catalog no. 29130) for 5 min with the Button valves pressurized (to ensure channels were filled with bBSA), then opened Button valves and continued to flow bBSA for an additional 30 min to allow binding. After bBSA introduction, we washed the entire device with PBS for 10 min. Next, we introduced 1 mg/mL neutravidin (NA) (Thermo Scientific, 31000) for 30 min to bind to the bBSA previously deposited on epoxysilane slide surfaces beneath Button valves and the Button itself, followed by another 10 min PBS wash. To saturate any NA bound outside of the Buttons, we again pressurized (closed) the Button valves (to protect NA-functionalized surfaces) and introduced bBSA for an additional 30 min, followed by another 10 min PBS wash. Finally, we depressurized (opened) the Button valves and introduced either a 100 µg/mL solution of biotinylated anti-GFP antibody (b-anti-eGFP; Abcam, catalog no. ab6658) or a mixture of biotinylated anti-GFP antibody and bBSA (final concentrations of 100 µg/mL and 50 µg/mL, respectively) for 15 min, thereby tuning the density of potential attachment sites and ultimate effective enzyme concentration (as described below). This surface patterning procedure ultimately yielded a bBSA/NA/b-anti-eGFP stack non-specifically adsorbed to epoxysilane slide surfaces (**Fig. S3**) capable of recruiting expressed enzymes to surfaces. We then again pressurized (closed) Buttons, washed with PBS for 10 min, closed the outlet valve (to prevent evaporation) and maintained the device under positive pressure to await the manual expression step. The device was stable in this state for at least 18 h.

On-chip expression of PafA-eGFP constructs

Printed PafA-eGFP mutant DNA spots were solubilized and protein was expressed using the PURExpress expression system (New England Biolabs Inc., catalog no. E6800L). To prepare the expression mixture, we mixed 10 µL of PURExpress Solution A with 7.5 µL of Solution B and allowed this mixture to incubate on ice for 30–45 min, as this incubation period increased yields of PafA-eGFP >2-fold. Immediately before flowing the reaction mixture into the chip, we added 2.5 µL of a 1 mM ZnCl₂ solution, 0.5 µL of 40 U/L RNasin ribonuclease inhibitor (Promega Corporation, catalog no. N2515), and 4.5 µL of nuclease-free water, and mixed gently. With the Neck valves closed, we flowed this expression mixture over the device for 12–15 min to ensure that PURExpress solution fully filled all channels. To introduce the PURExpress mixture into all expression chambers and solubilize the DNA, we closed the chip outlet valve, opened the Neck valve, and increased the flow pressure from 3.5 to 4–4.5 psi, thereby dead-end filling DNA chambers under pressure; the filling process was followed visually using a stereo microscope. When chambers were 90–95% full, we closed the Button, Neck, and Sandwich valves, isolating adjacent protein chambers from one another and closing the Button valves to prevent premature binding of contaminating enzyme in the case of any leakage between expression chambers within the flow path. We then placed the slide bearing the device onto a pre-warmed aluminum

hot plate (Torrey Pines Scientific) and allowed enzyme constructs to express for 45 min at 37°C. During expression, we opened the Sandwich valves and flowed 1X PafA reaction buffer (100 mM MOPS, 500 mM NaCl, 100 μ M ZnCl₂, pH 8.0) continuously through the device to counteract evaporation and wash out any enzyme leaking from expression chambers that would otherwise contaminate other chambers of the chip. Following expression, we removed devices from heat and incubated them for 90 min at room temperature in the dark to allow for maturation of the eGFP fluorophore.

Surface immobilization of expressed enzyme and subsequent buffer exchange

After enzyme expression, we removed device-slide assemblies from hot plates and mounted them on a fully automated Nikon Ti-S microscope (components described above). To bind expressed enzymes to antibody-functionalized regions of the glass protected by the Button and to the Button itself, we closed Sandwich valves (to isolate adjacent reaction chambers from one another), opened Button valves (to expose binding surfaces), and then opened the Neck valve, allowing diffusion of expressed enzyme into the reaction chamber. Binding was allowed to proceed for 15–60 min. During binding, we imaged chambers across the device periodically in the eGFP channel, and then closed Button valves to stop binding when the desired enzyme concentration ([E]) was reached.

As wild-type PafA is inhibited by inorganic phosphate (P_i), accurate measurement of kinetic rate constants requires that any P_i produced during the on-chip transcription and translation reactions be washed out prior to kinetic assays. To fully remove any remaining P_i from reaction chambers, we flushed the entire device with 1X PafA reaction buffer with the Neck valves open for 60 min immediately after completion of binding.

Removing cross-chamber enzyme contamination with surfactant washing

Accurate measurement of kinetic and thermodynamic parameters for mutants with compromised catalysis requires ensuring that chambers are free from even very low levels of contaminating WT-like enzyme molecules from other chambers non-specifically adsorbed to chamber walls or slide surfaces. Initial kinetic measurements for “empty” chambers (lacking a plasmid) were consistent with approximately 0–0.3 nM levels of contamination with WT-like enzyme molecules. To eliminate this cross-contamination, we washed each device (with Button valves closed) with four 5-min treatments of 1% (w/v) sodium dodecyl sulfate (SDS) in MES buffer at pH 6.0. This treatment lowered background enzymatic activity of non-specifically adsorbed enzyme by 50-fold (on average) while preserving the fluorescence of the enzyme-GFP fusion constructs under the Button and the activity of specifically bound enzyme. While we also tested use of chaotropes to denature non-specifically adsorbed enzyme, these agents resulted in death of Button-protected surface-immobilized enzymes. We suspect that this enzyme death under the Button occurs because the small hydrodynamic radius of these chaotropes allows them to quickly diffuse beneath the Button valve, unlike monomeric and micellar SDS.

Imaging and quantification of expressed enzymes

Imaging of eGFP signals

To detect and quantify expressed enzymes, we imaged devices in the “eGFP channel” using an eGFP filter set (Chroma Technology Corp., part no. 49002) with acquisition times of 500 ms per image. Using 2x2 binning, imaging of the full device typically required 49 tiled images with 10% overlap (~32 chambers per tile).

Automated detection of eGFP fluorescence spots

Measuring expression for a given mutant requires mapping each chamber to a unique positional index within the array (each of which contains a known spotted plasmid) and quantifying the eGFP signal beneath the Button valve in that chamber.

Initial image processing To correct for position-dependent differences in excitation intensities, we first applied a flat-field correction to each tile (79). We then generated complete images of each device by stitching the overlapped flat-field corrected tiles. After stitching, we corrected for PDMS autofluorescence by background-subtracting an image of the device acquired before construct expression. Finally, we divided each stitched image into 28x56 sub-images (stamps), each centered on and containing a single chamber, using the 4 corner chambers as reference positions. The ID of each mutant was then assigned to its corresponding stamp.

Quantification of eGFP fluorescence within each chamber Prior to the start of each kinetic assay, we quantified eGFP intensities beneath Button valves. To find the centroid positions of Button valve regions containing bound enzyme within each stamp, we used a combination of a sparse grid search (to identify the circular region of maximal summed fluorescence intensity) and a dense local grid search (to refine this position). We then summed intensities from all pixels within a fixed radius of 15 pixels, larger than the physical radius of the Button. To account for spatially-dependent differences in background intensities, we calculated a local background intensity considering pixels in an annulus concentric with, abutting, and larger than the Button bounding circle. Local background summed intensity was normalized to the Button area ($\#pixels_{Button}/\#pixels_{annulus}$) and subtracted from the summed Button region pixel intensity to yield a background-subtracted summed intensity used to quantify [E] in all downstream analyses.

eGFP intensity calibration curves

Quantitative measurement of the kinetic constants k_{cat} and k_{cat}/K_M hinges on accurate measurement of enzyme concentration ([E]). To convert measured eGFP intensities to effective [E], we patterned a device with anti-GFP antibody as described above, iteratively introduced 3 nM solutions of eGFP (BioVision, catalog no. 4999) with 2% (w/v) BSA (Ultra-Pure, ThermoFisher Scientific, catalog no. AM2616), incubated for 1200–7200 s, and then quantified bound fluorescence at saturation (**Fig. S5**). Prior to titrations, chamber walls were pre-equilibrated with eGFP by flowing a 3 nM or 5 nM solution of eGFP with 2%

(w/v) BSA (UltraPure, ThermoFisher Scientific, catalog no. AM2616) in 1X PafA reaction buffer for 10 min, washing for another 10 min with 1X PafA reaction buffer alone, and repeating this procedure three times. Control experiments in which Button valves were opened to expose anti-GFP-antibody-coated surfaces in the absence of introduced eGFP solution established that non-specifically-bound eGFP does not significantly migrate to Button surfaces and increase observed intensity. Bound fluorescence intensities underneath the Button were quantified as described above. Prior to saturation, measured summed intensities increased linearly with each additional injection of eGFP (as expected, given that the $K_D^{\alpha\text{-eGFP}} \ll 3$ nM). A linear fit to these first (typically 4–9) titration points ($\sim 0\text{--}20$ nM) yielded calibration parameters sufficient to convert measured intensity to [E] with an error of generally $< \pm 5\%$ (95% CI) in the linear fit region. We performed this procedure for every microscope and light source setup (and again upon any adjustments to the instruments), as differences in illumination intensity and optics can alter fit parameters.

Synthesis of fluorogenic cMUP and MecMUP substrates

Syntheses of cMUP and MecMUP were adapted from previously published work. For both substrates, methyl 7-hydroxycoumarin-4-acetate (Sigma-Aldrich, IDF00040) was used as the coumarinyl (phenolic) starting material, and intermediates were not purified.

To synthesize the phosphate monoester 2-(2-oxo-7-(phosphonoxy)-2H-chromen-4-yl)acetic acid (cMUP; **Fig. S10** compound **3**), we first generated the diethyl phosphate triester (compound **1**) analogously to previous reports by reacting the coumarin phenol (1.0 eq) with triethylamine (2.0 eq) in dry dichloromethane, adding dimethyl chlorophosphate (2.0 eq) dropwise while stirring under argon overnight (80). Crude products were subjected to an aqueous workup consisting of aqueous HCl, saturated NaHCO₃, and saturated NaCl, and organics were dried over MgSO₄ and concentrated to dryness under reduced pressure to afford the crude diethyl triester (compound **1**) as a golden oil. Adapted from a previously reported procedure (81), the crude phosphotriester coumarinyl methyl ester was subjected to alkaline saponification with stoichiometric LiOH monohydrate (2.0 eq) in 1:1 THF:H₂O. Products were acidified to pH 2–4 with HCl and extracted into dichloromethane. Organics were washed with saturated NaCl, dried over MgSO₄, and concentrated to dryness under reduced pressure to afford the crude deprotected diethyl triester **2** as an oily residue. Finally, deprotection of the phosphate ester was achieved with trimethylsilyl iodide (TMSI), also analogously to a previous reported synthesis (81). An oven-dried flask under an atmosphere of argon was charged with a solution of crude compound **2** in dry dichloromethane via syringe. To the stirring solution, TMSI (4.0 eq) was added via syringe, drop-wise, and the reaction was allowed to stir for 2 h in the dark. Then, the reaction was quenched by drop-wise addition into excess H₂O and adjusted to pH ~ 8 with 0.5 M NaOH. The biphasic mixture was allowed to stir, and the mixture was readjusted to pH 8 repeatedly with 0.5 M NaOH until the pH stopped dropping. The aqueous layer was separated and then washed with two portions of dichloromethane. The aqueous layer was then dried under reduced pressure in a heated bath to give a white-yellow solid of crude phosphate monoester **3** (subsequently purified and characterized, below).

The phosphate diester substrate 2-(7-((hydroxy(methoxy)phosphoryl)oxy)-2-oxo-2H-chromen-4-yl)acetic acid (MecMUP; **Fig. S10** compound **6**), was also prepared via a

phosphate triester. First, the phosphate methyl triester was prepared as described for ethyl triester (**1**), to afford crude compound **4** as an oil. Then, crude reaction products were singly deprotected with LiCl (2 eq) in refluxing acetone for 2 h, as previously reported, with altered workup as follows (82). Upon evaporation to remove solvent, products were resuspended in water and acidified to pH 2–3 with 0.5 M HCl, washed with two portions of dichloromethane, and the aqueous phase was again concentrated, yielding an oil of impure compound **5**. Finally, to generate the desired phosphodiester carboxylic acid, the carbonyl ester was deprotected by basifying an aqueous solution of crude products in water to ca. pH 8 with 0.5 M NaOH, and reacting with LiOH (2 eq) in THF:H₂O (1:1) for ~7 h at room temperature under air, analogously to deprotection of the phosphate monoester. The reaction was halted by acidifying to pH 7 with 0.5 M HCl, and solvent was removed under reduced pressure to afford crude phosphate diester **6** (subsequently purified and characterized, below).

Crude phosphate monoester and phosphate diester products were purified via semi-preparative HPLC using an Agilent 1260 HPLC equipped with a C18 reverse-phase column and eluting with a gradient of 0.1% TFA in H₂O into MeCN. Phosphate monoester substrate eluted as the largest peak (detecting absorption at 360 nm); phosphate diester substrate eluted as the second principal peak (again detecting absorption at 360 nm). Product-containing fractions were subsequently pooled and lyophilized, yielding off-white powders.

HPLC-purified material was characterized via ¹H and ³¹P NMR (externally-referenced to 85% H₃PO₄) with a Varian Mercury 400 MHz magnet or Varian Inova 500 MHz magnet and processed with MestReNova 11 (Mestrelab Research) (**Figs. S11 and S12**). Compound **3** (monoester): ¹H NMR (400 MHz, D₂O) δ 7.65 (d, *J* = 8.5 Hz, 1H), 7.16–7.19 (m, 2H), 6.37 (s, 1H), 3.94 (s, 2H); ³¹P NMR (202 MHz, D₂O, externally referenced to 85% H₃PO₄ at 0.00ppm) δ -4.00. Compound **6** (diester): ¹H NMR (400 MHz, D₂O) δ 7.66 (d, *J* = 8.7 Hz, 1H), 7.15–7.19 (m, 2H), 6.38 (s, 1H), 3.93 (app. d, 2H), 3.65 (d, ³*J*_{31P,1H} = 11.1 Hz, 3H); ³¹P NMR (202 MHz, D₂O, externally referenced to 85% H₃PO₄ at 0.00ppm) δ -2.72. Stock solution concentration determination was performed spectrophotometrically by complete hydrolysis using an *E. coli* alkaline phosphatase mutant not inhibited by P_i (R166S) and quantification of generated free leaving group (fluorogenic hydrolysis product) using a standard series of 7-hydroxycoumarinyl-4-acetic acid (cMU; Sigma-Aldrich, IDF00040).

Multi-Tier measurement strategy

Measuring kinetic constants for all mutants within the 1036 member valine and glycine scanning libraries requires the ability to accurately quantify initial rates spanning >5 orders of magnitude (Main Text **Fig. 1**). Measurements at the limits of this range pose distinct technical challenges: fast mutants require low concentrations of expressed enzyme to slow reactions to allow multiple measurements before substrate is exhausted, while slow mutants require high concentrations of expressed enzyme and have activities easily obscured by even small amounts of cross-contamination from neighboring chambers. To maximize measurements efficiency and enhance the accuracy and precision of returned catalytic and thermodynamic parameters, we therefore measured rates for all experiments using a three-Tier experimental pipeline (**Table S2**), in which mutants with similar rates were measured

in separate experiments (“Tiers”). During tier 1, we assayed all valine and glycine mutants at low enzyme concentration ([E]) (approx. 1.5 nM). During tier 2, we reprinted and assayed all mutants >10-fold down in cMUP or MeP hydrolysis, on the “Slow cMUP” or “Slow MeP” devices, respectively, using higher [E] (approx. 15 nM). In tier 3, we reprinted and assayed all mutants that remained un-resolvable during tier 2, at high [E] (approx. 15 nM).

***In vivo* expression, purification, and assay of control WT PafA and active site mutants**

To compare the Michaelis-Menten parameters determined from on-chip measurements with those from traditional off-chip assays, we recombinantly expressed wild-type PafA and 5 active site mutants, and measured their activities using the same substrates as used in on-chip assays. C-terminally Strep-tagged PafA WT and mutants were over-expressed and purified as previously described (16). Briefly, 20 mL of starter culture was prepared from plasmid-transformed SM547(DE3) *E. coli* cells in Luria Broth (LB) with 50 µg/mL carbenicillin. The starter culture was added to 2 L of Luria broth and grown at 37°C to an OD600 of 0.6. IPTG was then added to a final concentration of 300 µM to induce protein expression, and cells were incubated on a rotor overnight at room temperature. Enzymes were affinity purified from filtered cell lysate over Streptactin Sepharose resin (Cytiva, catalog no. 17511301) and purity was assessed via SDS-PAGE gels to be >95% for all preps. Enzyme kinetic measurements were collected on Synnergy H4 and Tecan Infinite M200 plate readers, as described previously (16), except the build-up of fluorescent cMU from cMUP and MecMUP reactions was followed using excitation and emission wavelengths of 365 nm and 455 nm, respectively.

Measuring cMUP hydrolysis on-chip

Imaging of fluorescent leaving group (cMU) fluorescence

To detect and quantify the fluorescent product cMU (7-hydroxycoumarinyl-4-acetic acid) of cMUP and MecMUP hydrolysis, we imaged devices in the “DAPI channel” using a DAPI filter set (Semrock Inc., catalog no. DAPI-1160B-NTE) with acquisition times ranging from 50–200 ms and using 2x2 binning.

Measuring cMU fluorescence standard curves

To convert product intensities measured during activity assays to product concentrations and correct for position-dependent intensity differences, we measured product (cMU) standard curves for each chamber of each device by sequentially introducing increasing concentrations of cMU product in 1X PafA reaction buffer (0, 2, 5, 10, 25, 50, and 100 µM) and imaging the device after enzyme expression and purification but before kinetic assays. We generated a separate standard curve for each chamber of the device in order to correct for position-dependent excitation intensity differences in the DAPI channel. For each concentration, we (1) closed the Button valves in all chambers across the device to protect

surface-immobilized enzyme. (2) We then flowed the solution over the device for 6–8 min to fully equilibrate all chambers. (3) Sandwich valves were then closed to isolate adjacent reaction chambers from one another, before opening the Button valve and iteratively imaging all chambers across the device over time.

Image processing for cMU fluorescence standard curves First, we mapped chambers and generated image stamps as described previously (*cf.*, *Imaging and quantification of expressed enzymes*). We then automatically detected chamber center positions from stamps acquired at the highest cMU concentration using a Hough circle transform via OpenCV (83). If no circles were initially found, we increased permissiveness of the Hough circle transform using a grid-search of Hough transform “accumulator threshold” and “gradient” parameters. If multiple circles were found, in either case, we selected the circle with highest median pixel intensity. For chambers in which a “best” circle was found following this procedure, we circumscribed the chamber using the center of this circle and a fixed chamber radius, and used the median pixel brightness within this region for all downstream kinetic analysis. These chamber boundaries were subsequently used for all other cMU concentrations and downstream analysis of kinetic assays.

Standard curve fitting To generate product standard curves, we identified chamber boundaries as described above, calculated the median intensity for each chamber for each product concentration, and collated these data by chamber. For each chamber, we performed a linear least-squares fit to measured intensities as a function of concentration and used these fit parameters to convert measured intensities to product concentrations in downstream assays.

Performing kinetic assays

On-chip cMUP hydrolysis assays were performed in 100 mM MOPS, 500 mM NaCl, 100 μ M ZnCl₂, pH 8.0 (1X PafA reaction buffer). Substrate concentrations used were generally 10, 25, 50, 100, 200, 500, and 1000 μ M, with the addition of 2 μ M in a subset of experiments. Before starting reactions, substrate solution was flowed for 6–8 min to fully exchange the solution in the device, with the Button valves closed. To start reactions, the Sandwich valves were closed (to separate chambers from one another and prevent leakage of product) and the Buttons were opened to expose the immobilized enzyme to substrate and start the reaction.

Assays were acquired in ascending order of [cMUP], and, when possible, we performed replicate 10 or 50 μ M [cMUP] assays after the 1000 μ M assay to check for enzyme death over the course of the full experiment.

Kinetic assay image acquisition Enzymatic turnover was quantified by acquiring a time series of images in the DAPI channel (for detection of cMU). Images were iteratively acquired for all chambers across the device over time, saving images with a timestamp that indicated the precise time of acquisition. Exposure times were either 50 or 200 ms. As for eGFP imaging, cMU imaging required 49 tiles (10% overlap, 2x2 binning), so that each

full chip image required ~ 75 s. Most assays were acquired for 65 min, but ranged from 24 min to ~ 6 h, depending on which experimental tier was being measured. To measure initial rates for both fast and slow enzyme mutants, we initially acquired images as quickly as possible (10 full images spaced 75 s apart) and then acquired images at pseudo-logarithmically increasing time intervals. For our standard 65 min assay, acquisition times were 75 ($\times 9$), 150, 300, 600, 900, and 1200 s. Actual acquisition times for each chamber are reported in the per-experiment CSV files.

Analysis and quality control of cMUP hydrolysis measurements

All code for analyzing experimental data exist in Mathematica notebooks available as part of the **OSF Repository Data** (<https://doi.org/10.17605/OSF.IO/QRN3C>) (74). To identify and flag chamber measurements likely contaminated by enzymes from neighboring chambers, we developed and applied a series of quality control procedures as described below (**Figs. S14–S16**). All data and quality control flags are included in the per-experiment CSV and PDF files in the **OSF Repository Data** and on the Fordyce Lab website (<http://www.fordycelab.com/publication-data>).

Obtaining initial rate measurements

To process images and obtain kinetic measurements for each chamber, we first calculated the median intensity at each time point using the chamber boundaries defined from the cMU standard curve (see above).

To determine initial rates, we then fit median chamber intensities as a function of time to a linear model and converted fitted rates from RFU to [cMU] using the per-chamber standard calibration curves described above. To ensure that fits consider only time-points in the linear regime, we included only timepoints at which cMU concentrations were $< 30\%$ of the initial cMUP concentration, $[S_0]$ ($[P] < 0.3[S_0]$).

Fitting Michaelis-Menten parameters

The parameters k_{cat} , K_M , and k_{cat}/K_M were determined from a non-linear least-squares fit of the initial rates at each substrate concentration to the Michaelis-Menten equation (**Eq. 1**):

$$v_i = \frac{k_{\text{cat}}[E][S]}{K_M + [S]} \quad (1)$$

In all cases, Michaelis-Menten parameters were determined using estimated enzyme concentrations from images acquired immediately prior to starting the series of kinetic assays, based on control experiments in which we measured the activity loss over the full assays series by comparing the rates of the first 10 μM [cMUP] assay to those of the replicate acquired at the end of the full series. Scaling by the enzyme concentrations determined from eGFP intensity measurements obtained immediately before each assay resulted in the rates of the replicate assay being significantly higher than the original measurement, while

the unscaled rates are in good agreement (**Fig. S8**). This indicates that the eGFP fluorescence loss is decoupled from any PafA activity loss, which itself is not significant over a single cMUP titration series. This is likely due to enzyme lost from the Button non-specifically binding the chamber walls (rather than remaining in solution and being flushed out). We therefore used the [E] measured before the first assay of the series to determine kinetic parameters.

Flagging K_M values outside the range of [cMUP] used

Accurate determination of K_M requires the ability to measure initial rates at concentrations significantly above and below this value. For measurements with fit K_M values >2 -fold lower than the lowest [substrate] ($K_M < [\text{cMUP}]_{\text{lowest}}/2$) for more than 50% of the total replicates, we set $K_M = [\text{cMUP}]_{\text{lowest}}/2$ and flagged these values as upper limits (8 mutants, including the active site mutants T79S and N100A). K_M upper limits result in k_{cat}/K_M being lower limits, while k_{cat} values can still be determined.

We applied an analogous criterion to flag as lower limits mutants with K_M values higher than the measurable range (where $K_M > 2[\text{cMUP}]_{\text{highest}}$, for more than 50% of the total replicates); however, no mutants met this criterion.

Lower limit of resolution due to non-PafA-driven hydrolysis

Hydrolysis by water and other buffer components imposes an absolute lower limit on the measurable initial rate of *enzymatic* substrate hydrolysis. To quantify rates of non-PafA-mediated hydrolysis on the device, we performed the standard on-chip surface patterning procedure, introduced a catalytically incompetent PafA mutant, T79G, expressed off chip via *in vitro* transcription/translation into one half of the HT-MEK device, and then measured rates of hydrolysis of cMUP across all chambers. To determine apparent first order rate constants, we fit the last 7 points of this time course, avoiding early timepoints in which measured intensities are significantly affected by photobleaching and diffusion between solutions within the flow and control layers of the device, resulting in negative rates. We measured first order rate constants of $\sim 5.0 \times 10^{-5} \text{ h}^{-1}$ and $1.1 \times 10^{-5} \text{ h}^{-1}$ at 500 μM cMUP for T79G-containing and empty chambers, respectively (median, $n = 671$ and 895, respectively). These observed rate constants are approximately 5-fold higher and the same as the rate expected for cMUP hydrolysis by water at pH 8.0 based on published values for para-nitrophenylphosphate (pNPP) ($9.7 \times 10^{-6} \text{ h}^{-1}$) (13), suggesting that the practical limit of resolution for on-chip reactions is largely defined by the uncatalyzed rate of hydrolysis.

Flagging based on detected PafA-eGFP expression

To flag chambers with levels of expressed PafA below the limit of accurate on-chip quantification or containing high-intensity spot artifacts resulting from dust, we automatically eliminated any chambers containing a calculated [E] $< 0.3 \text{ nM}$ (**Fig. S14**). Chambers were also manually inspected and flagged based on Button morphologies and the presence of high-intensity pixel artifacts using a scripted GUI.

Flagging 2-point initial rate fits to minimize error in measurements of fast enzymes

Imaging all chambers within an HT-MEK device requires ~ 75 s. This minimum time delay between successive images of a given chamber sets an upper limit on rates that can accurately be measured, as WT PafA and the fastest mutants may hydrolyze a significant fraction ($>30\%$) of substrate within the first 2 acquisition time-points, leading to underestimation of initial rates (**Fig. S13A**).

To determine the conditions under which systematic underestimation of initial rates leads to systematic errors on fit Michaelis-Menten parameters, we: (1) simulated progress curves for WT-like enzymes hydrolyzing cMUP for enzyme concentrations between 0.1 and 7.5 nM (**Fig. S13B**), (2) simulated sampling at different acquisition times ($t = 2$ s, 37.5 s, and 75 s, corresponding to chambers at the top, middle, and bottom of the device, respectively) (**Fig. S13B**), (3) estimated rates from either a linear fit (for simulated curves in which $<30\%$ of substrate has been hydrolyzed by the second timepoint) or from a 2 point fit (for simulated curves in which $<30\%$ of substrate has been hydrolyzed by the second timepoint), (4) compared these estimated rates to the “true” rates (**Fig. S13B**), (5) repeated this process for every cMUP concentration used in the experiment, and then (6) compared fitted Michaelis-Menten parameters to the “true” parameters used in the simulation (**Fig. S13C**). While fitted k_{cat} values were not significantly affected, chambers at the bottom of device had fitted K_M values that were inflated by $\sim 20\%$ for chambers with >5 two-point fits (of 7 total) and became progressively more inflated as the number of two-point fits increased (**Fig. S13D**).

To test if we observed these predicted trends in the HT-MEK data, we plotted the fitted K_M for all WT PafA constructs within tier 1 (fast enzymes, low [E]) and tier 2 (slow enzymes, high [E]) experiments. As predicted, fitted K_M values for chambers with >5 two-point fits showed systematic increases. To ensure accurate K_M estimates, we therefore flagged all chambers in which >5 of the 7 initial rates (corresponding to each [cMUP]) were determined from two-point fits and eliminated them from downstream analysis.

Assessing measurement quality using “fiducial activity measurements” and local Lower Limit of Detection (LLoD)

As the kinetic parameters of enzymes within the mutant library span a wide dynamic range, even very small amounts of contaminating “fast” enzymes within chambers containing “slow” enzymes could yield artificially high observed rates. To detect any such contamination, each printed array included “fiducial activity” spots interspersed throughout containing either no plasmid (“Skipped”) or a catalytically-incompetent or compromised mutant (T79G and/or K162A). Initial experiments probing PafA active site mutants included “Skipped” and T79G chambers every other chamber (1248 chambers total). tier 1 (low [E]) and 2 (high [E]) scanning library experiments included either “Skipped” chambers or chambers containing T79G or K162A (mutants with a $> 10^4$ -fold decrease in catalysis compared to WT) constructs at every seventh chamber within a channel; this number of fiducial chambers increased in tiers 2 and 3 (high [E]) (as enumerated in **Table S2**). For tier 3 (high [E]), the K162A mutant became measurable; thus, we estimated LLoDs via linear interpolations of the rates for the T79G and “Skipped” chambers as a function of

row number for each column on the device at each [cMUP].

For each kinetic assay, we calculated observed rates of hydrolysis for these fiducial chambers and then estimated an observed local background hydrolysis rate (Lower Limit of Detection, LLoD) for all chambers using a linear interpolation of these observed rates along a given channel (column) and the previously measured background rate of non-PafA-mediated hydrolysis (**Fig. S15A**):

$$\text{LLoD} = \frac{v_i^{\text{obs}} - v_{\text{bg}}^{\text{true}}}{v_{\text{bg}}^{\text{obs}} - v_{\text{bg}}^{\text{true}}} \quad (2)$$

where v_i^{obs} denotes the observed initial rate, $v_{\text{bg}}^{\text{obs}}$ denotes the interpolated background rate from catalytically-inactive or compromised chambers, and $v_{\text{bg}}^{\text{true}}$ denotes the on-chip measured background rate ($-4 \times 10^{-5} \mu\text{Ms}^{-1}$). In contrast to prior efforts to measure a true background rate (*cf. Lower limit of resolution due to non-PafA-driven hydrolysis*), where we considered only later timepoints to minimize contributions from photobleaching and diffusion across PDMS layers, to determine this number we considered only the early timepoints to accurately mimic observed effects during kinetic assays, yielding the slightly negative observed rate.

To determine the minimum activity threshold above the LLoD that would minimize false positives without unnecessarily culling data, we simulated initial rates as a function of [cMUP] for mutant k_{cat} values from 0.2–500 s^{-1} and K_{M} values from 0.05–500 μM in the presence of a variable amount of a “contaminant” enzyme with WT parameters (1×10^{-5} to 0.2 nM, with 0.2 nM representing the total amount of enzyme immobilized under the Button valve). For each simulation, we: (1) divided the simulated rate (for the mutant enzyme plus WT-like contaminant) by the contribution from “background” contaminant only (**Eq. 2**, assuming $v_{\text{bg}}^{\text{true}}$ for the purposes of simulation) to calculate a “fold-change over the limit of detection”, (2) fit observed rates to the Michaelis-Menten equation to yield simulated observed k_{cat} and K_{M} values, and (3) plot the ratio of the observed k_{cat} and K_{M} values to the true value as a function of the fold-change over the limit of detection. This analysis suggests that a fold-change over the limit of detection of ≥ 5 allows accurate measurement of k_{cat} and K_{M} values spanning the range from wild-type PafA to all known active site mutants within 2-fold (**Fig. S15B**). We therefore flagged all chambers in which observed rates were < 5 -fold above the per-chamber estimated LLoD and removed them from downstream analysis.

Aggregating cMUP hydrolysis data across experiments

To aggregate data across experiments and across tiers, identify likely outlier measurements, estimate error on returned parameters, and test for statistically significant differences from WT values, we carried out multiple replicate experiments within each tier to obtain multiple replicates of each mutant. At this stage, we also applied additional quality control filters and normalizations as described below (and see **Figs. S16–S17**). We provide final aggregated estimates for each mutant in the **OSF Repository Data** (<https://doi.org/10.17605/OSF.IO/QRN3C>) (74).

Aggregating measurements for mutants measured across multiple tiers

Many mutants have rates that cannot be resolved during tier 1 (low [E], fast mutant experiments). For these mutants, rare replicates that pass quality control filters in tier 1 most likely result from cross-chamber contamination, and inclusion of these replicates could skew measured rates.

Estimating false positive probabilities for mutants with many replicates To estimate the probability of a slow mutant replicate erroneously passing the LLoD filter, we re-examined the initial active site mutant experiments, in which true rates for all mutants are known and every second chamber is a “fiducial rate” chamber. To quantify the number of slow mutants that might erroneously pass a LLoD filter with fewer “fiducial rate” spots, we: (1) sub-sampled the “fiducial rate” chambers to mimic having such chambers at only every 7th position (as in the tier 1 (low [E]) experiments), (2) calculated an apparent interpolated local LLoD for each channel, and (3) quantified the number of slow mutants that would erroneously pass this local LLoD due to local contamination. These simulations returned a median false positive rate of $11 \pm 3\%$ (SD).

Next, we tested whether this predicted false positive rate was consistent with experimental observations in tier 1 (low [E]). In the glycine and valine scanning library measurements, we expect that: (1) most mutants will behave similarly to the WT enzyme, (2) chambers with artificially high rates from cross-chamber contamination will, therefore, most likely be contaminated with WT-like enzyme, and (3) that cross-chamber contamination will disproportionately affect mutants with the slowest kinetic parameters resolved within a given experimental tier. The T79S, N100A, and R164A mutants have significantly tighter K_M values compared to WT, are near the lower dynamic range limit for tier 1 (low [E]) experiments (k_{cat} values of 1 s^{-1} for T79S and N100A and 5 s^{-1} for R164A), and each device contained between 4 and 20 replicates of each mutant (with $[E] > 0.3 \text{ nM}$). We therefore compared the fitted K_M values for these mutants with their known values to test if the measured rates in these chambers arise from WT-like contaminant or from the mutants themselves. For each mutant, we calculated: (1) the number of chambers passing the tier 1 (low [E]) local LLoD filter, and (2) the Michaelis-Menten parameters for chambers that did and did not pass the tier 1 local LLoD filter. While the R164A mutant K_M values recapitulated the off-chip value for this mutant (establishing that R164A can be accurately measured in tier 1 (low [E])), the majority of T79S and N100A chambers had significant deviations from their expected K_M values (**Fig. S16A**). The majority of these T79S and N100A chambers were successfully culled (**Fig. S16B**); however, $\sim 10\%$ and $\sim 4\%$ of chambers passed quality control and had WT-like K_M values (**Fig. S16A**, red points). This indicates that these are likely false positives and provides a second conservative estimate of the false positive rate of $\sim 10\%$.

Estimating false positive measurements in tier 1 (low [E]) as a function of number of replicates Previous off-chip measurements and high replicate numbers allowed us to estimate the false positive probability for T79S and N100A (~ 100 replicates, $f_{passed} = 0.1$). However, most mutants have a smaller number of total replicates (~ 5) (**Fig. S21B**), so the observed false positive probabilities will likely be higher. To estimate false positive

probabilities for smaller replicate numbers, we simulated the number of replicates likely to erroneously pass the LLoD filter as a function of number of replicates for a mutant too slow to be measured in tier 1 (low [E]) using the 10% false positive rate (**Fig. S16C**). Based on these simulations for 5 replicates, we selected a conservative cutoff of $f_{\text{passed}} = 0.4$ for tier 1 (low [E]) and 2 (high [E]). For mutants not meeting this criterion, we incorporated only measurements from tiers 2 and 3 (high [E]). For tier 3, we did not implement this cutoff as all mutants were separated by a “fiducial” chamber in these experiments.

Normalizing k_{cat} and k_{cat}/K_M measurements across experiments and tiers

Rationale for cross-experiment normalization Within and across experimental tiers, we observed systematic variations in measured k_{cat} values for WT PafA and other active site mutants (**Fig. S17A**). One model for variability in measured k_{cat} values between experimental replicates is that small and variable amounts of enzyme can remain non-specifically adsorbed to chamber walls even after stringent washing and contribute to hydrolysis. To test for this, we performed the standard expression procedure (including on-chip expression, a 1 h incubation post-expression to allow expressed constructs to bind, and subsequent SDS washing) for a tier 1 (low [E]) library on a device in which we patterned BSA across all device surfaces in the first step (to eliminate neutravidin binding beneath the Button) and additionally flowed bBSA across the device with Button valves open prior to introducing anti-eGFP. This protocol should eliminate any anti-eGFP binding sites underneath the Button, thereby preventing specific recruitment of enzymes to the surface. We then measured cMUP standard curves and initial rates of turnover across all chambers to obtain a full Michaelis-Menten curve and fit observed rates to the following equation:

$$V_{\text{max}}^{\text{obs}} = k_{\text{cat}}^{\text{intrinsic}} ([E]_{\text{self}}^{\text{Button}} + [E]_{\text{self}}^{\text{wall}}) \quad (3)$$

Returned apparent concentrations of enzymes bound non-specifically to chambers were distributed around a median of 0.38 nM with a long tail extending past 0.1 nM (**Fig. S17B**). However, the amount of non-specifically adsorbed mutant enzyme likely varies within and between devices based on actual flow rates within device channels and the duration of incubation times between expression and washout. We therefore normalized data between experiments prior to aggregation using a linear normalization strategy, as described below.

Linear normalization procedure To normalize data across experiments, we rely on measured values for WT PafA and the R164A mutants as follows:

(1) We normalize tier 1 (low [E]) experiments to one another by: (1) calculating the median k_{cat} for all WT replicates within *each* tier 1 experiment, (2) calculating the median k_{cat} for *all* WT replicates across all tier 1 experiments (WT ‘grand median’), and then (3) scaling each k_{cat} measurement within each experiment by the ratio of the WT grand median to the per-experiment median.

(2) tier 2 and 3 (high [E]) experiments typically did not contain WT replicates, and, at the high [E] used, WT measurements are extremely prone to two-point initial rate fits (see above). We therefore perform the same normalization for the tier 2 and 3 experiments using R164A measurements instead of WT.

(3) As R164A mutants are present across all tiers, the tier 1 (low [E]) and 2/3 (high [E]) experiments are normalized using the R164A ‘grand medians’ in tier 1 and tiers 2 and 3.

For mutant replicates in Tier 1 (low [E]) experiments, this process is expressed as:

$$k_{\text{cat}}^{\text{Norm.}} = k_{\text{cat}}^{\text{obs.}} \left(\frac{\tilde{k}_{\text{cat}}^{\text{obs.,WT,Tier 1}}}{\tilde{k}_{\text{cat}}^{\text{WT,expt.i}}} \right) \left(\frac{\tilde{k}_{\text{cat}}^{\text{R164A,All tiers}}}{\tilde{k}_{\text{cat}}^{\text{R164A,Tier 1}}} \right) \quad (4)$$

where $k_{\text{cat}}^{\text{obs.}}$ is the fitted k_{cat} for each individual mutant replicate, $\tilde{k}_{\text{cat}}^{\text{WT,expt.i}}$ is the median WT k_{cat} within the same experiment as the mutant, $\tilde{k}_{\text{cat}}^{\text{WT,Tier 1}}$ is the median WT k_{cat} across all tier 1 (low [E]) experiments (grand median), $\tilde{k}_{\text{cat}}^{\text{R164A,All tiers}}$ is the R164A ‘grand median’ used to normalize across tiers 1 and 2/3, and $k_{\text{cat}}^{\text{Norm.}}$ is the normalized k_{cat} .

For mutant replicates in tier 2 and 3 experiments (high [E]):

$$k_{\text{cat}}^{\text{Norm.}} = k_{\text{cat}}^{\text{obs.}} \left(\frac{\tilde{k}_{\text{cat}}^{\text{R164A,All tiers}}}{\tilde{k}_{\text{cat}}^{\text{R164A,expt.i}}} \right) \quad (5)$$

where $\tilde{k}_{\text{cat}}^{\text{R164A,expt.i}}$ is the median R164A k_{cat} within the same experiment as the mutant and $\tilde{k}_{\text{cat}}^{\text{R164A,All tiers}}$ is the R164A ‘grand median’, calculated by taking the median of the R164A tier 1 and tier 2/3 median values.

Normalized k_{cat}/K_M values were determined using the same normalization factors (*i.e.* replacing $k_{\text{cat}}^{\text{obs}}$ with $k_{\text{cat}}/K_M^{\text{obs}}$ in **Eqs. 4** and **5**). Final normalization factors were all within ~2-fold, and this procedure significantly reduced cross-experiment variance compared with unnormalized rates (**Fig. S17, C and D**).

Specifying lower limits for very slow mutants

A total of 24 of the 1036 mutants expressed but were too slow to measure even in tier 3 (high [E]) experiments. For these mutants, we defined an estimated upper limit k_{cat}/K_M by: (1) assuming that the lowest [cMUP] (typically 10 μM) is below the K_M of the mutant, which is reasonable based on the distribution of K_M values for all mutants (**Fig. S23**), (2) converting the initial rate measured at the lowest [cMUP] into an observed second-order rate constant (k_{obs}), and (3) denoting this as an upper limit.

Testing statistical significance of measured effects

The large number of replicate measurements obtained for each mutant allow us to leverage statistical techniques to estimate effect magnitudes, probe the quality of the evidence behind each estimate, and estimate the probability that a mutant’s measured kinetic parameters differ from those of the WT enzyme.

After aggregating all replicates for each mutant, we calculated p -values under the null hypothesis that the observed median estimate of a mutant parameter did not differ from that of the WT enzyme. For each kinetic parameter, we compared the distribution of measurements for a given mutant with the distribution of measurements for the WT enzyme using a bootstrap hypothesis test (84). For each individual mutant, we: (1) pooled the m observations of the mutant distribution with the n WT observations, (2) randomly selected bootstrap

samples by sampling from this pool m and n times, with replacement, corresponding to the number of mutant and WT observations, respectively (denoted by WT^* and $mutant^*$), and then (3) calculated the difference between median values for these bootstrap samples (t^* , where $t^* = |\tilde{WT}^* - \tilde{mutant}^*|$). After iterating this procedure multiple times, we computed p -values by counting the fraction of times the observed difference between the medians of the two samples was smaller than the difference recorded in the bootstrap procedure:

$$p = \frac{\#(t_{\text{obs}} < t^*)}{N} \quad (6)$$

where t_{obs} represents the experimentally observed difference between the mutant and WT medians and N represents the number of bootstrap iterations. To enhance computational efficiency, we initially calculated p -values using 100 iterations and increased the number of iterations to 1000 and 1×10^5 only when necessary to resolve small p -values for mutants whose parameter estimates were very different from wild-type ($p \leq 0.1$ and $p \leq 0.01$, respectively). For mutants with cMUP k_{cat}/K_M values resolvable only as upper limits, we calculated p -values in a similar manner using upper limit k_{obs} values; in this case, resulting p -values are also upper limits.

We defined $p < 0.01$ as a conservative threshold for declaring a mutational effect (rejecting the null hypothesis) for a given parameter. As we assayed 1036 individual mutants, we expect some number of false positives at this p -value threshold. Thus, we implemented a Benjamini-Hochberg false discovery rate (FDR) controlling procedure at a type I error rate of $\alpha = 0.05$ (85). This procedure suggested that, generally, mutants with $p > 0.01$ are at a higher than desired probability of being false discoveries (**fig. S24**), which supported our choice to use $p < 0.01$ as a metric for strong evidence of a mutational effect.

Probing for equilibrium unfolding, changes in Zn^{2+} affinity, and changes in enzymatic pK_a

To test three models that could account for changes in the fraction of active enzyme on the device, we obtained independent on-chip measurements of cMUP as a function of urea concentration, Zn^{2+} concentration, and pH, as described below (see **Supplementary Text S1**).

Urea titration

To measure activities in the presence of 0–2 M urea, we expressed enzymes on-chip using the standard protocol described above and then measured enzyme progress curves at 50 μM [cMUP] in the standard reaction buffer (100 mM MOPS, 500 mM NaCl, 100 μM Zn^{2+} , pH 8.0) with added [urea] at 0, 1, and 2 M. Measurements were acquired sequentially in order of increasing [urea] and per-experiment quality control was applied as described above.

To determine the urea dependence of each mutant, we scaled the rates of each individual replicate by the enzyme concentration and then normalized to the [E]-scaled rate at 0 M. For mutants with >1 replicate, we used the mean of all normalized rates in subsequent analyses. We then plotted normalized rates as a function of [urea] and compared them to the theoretical curves expected for [urea]_{1/2} values of 0 and 1 M (Main Text **Fig. 2H**).

The urea dependency of enzyme activity was measured off-chip by following turn over of the chromogenic phosphate diester methyl-paranitrophenylphosphate (MepNPP) (0.5 mM) by WT PafA (0.1 μ M) with the following concentrations of urea added immediately before measuring turnover: 0, 0.1, 0.2, 0.5, 1.2, and 4M urea. WT PafA was expressed and turnover was measured using a Tecan plate reader as described above. Initial rates of turnover were fit to a competitive model of inhibition, as described below (**Eq. 18**), yielding an apparent K_i .

Equilibrium Zn^{2+} titration

To measure the $[Zn^{2+}]$ dependence of activity, we expressed enzymes on-chip using the standard protocol and then measured rates of hydrolysis for 50 μ M [cMUP] under standard buffer conditions in the presence of 100 μ M Zn^{2+} . We then measured rates of hydrolysis in the presence of 500, 100, 25, 10, and 1 μ M $[Zn^{2+}]$, in order of descending $[Zn^{2+}]$. To ensure that the $[Zn^{2+}]$ was completely exchanged and that we have reached equilibrium at each $[Zn^{2+}]$, we carried out 6 sequential assays at each $[Zn^{2+}]$ (~6.5 hours total at each $[Zn^{2+}]$). We then calculated mean rates for each mutant at each $[Zn^{2+}]$, normalized them to the median rate for each mutant at 100 μ M $[Zn^{2+}]$, and plotted normalized rates as a function of $[Zn^{2+}]$ (Main Text **Fig. 2I**).

Measuring enzymatic pK_a s

Mutations might shift the enzymatic pK_a from the WT-value of ~8.0 (16) to more acidic values, diminishing apparent activity under assays at pH 8. To test for this, we acquired Michaelis-Menten curves at pH 7, 7.5, and 8.5 in addition to the standard pH of 8. To minimize chip-to-chip variability, we acquired all pH data on the same device by acquiring Michaelis-Menten curves at five concentrations (10, 250, 100, 200, and 1000 μ M) rather than the standard 7, and also acquired per-chamber cMU standard curves at only three concentrations (2, 10, and 50 μ M). Each turnover assay was 2925 s in duration and we acquired Michaelis-Menten curves in the following pH order: 8, 7.5, 7.0, and 8.5. We determined k_{cat}/K_M values for each mutant at each pH and compared these to theoretical curves assuming a 2-state pH-dependent inactivation (competitive inhibition) model with pK_a s between 5 and 8 (see **Supplementary Text S1** and **Fig. S27**).

Measuring methyl phosphate hydrolysis using HT-MEK

To measure hydrolysis of methyl phosphate (MeP), we developed an on-chip coupled assay in which we detect production of inorganic phosphate (P_i) using a commercially available fluorophore-derivatized phosphate binding protein (PBP; Phosphate Sensor, ThermoFisher, catalog no. PV4406) (18). Binding of (P_i) by PBP leads to an increase in fluorescence that we detected via excitation at 427/10 and collection of emitted light at 470 nm using a custom “PBP” filter set (Semrock Inc., 427/10 bandpass excitation filter, catalog no. FF01-427/10-25; 470/22 bandpass emission filter, catalog no. FF01-470/22-25; 442 nm dichroic beamsplitter, catalog no. DI03-R442-T1-25X36; mounted in a TE2000 filter cube, catalog no. NTE).

Measuring enzyme concentration for MeP assays

Small amounts of PBP can non-specifically bind to the chamber surface (including the Button valve) and interfere with eGFP quantification. To avoid this, we measured enzyme concentrations by measuring eGFP intensities before introducing PBP into the device and acquiring the standard curve.

On-chip $[P_i]$ standard curves

To obtain per-chamber standard curves relating fluorescence of PBP to $[P_i]$, we prepared standards containing between 0 and 150 μM P_i (typically 0, 1, 3, 6, 15, 30, 75, and 150 μM) and 30 μM PBP in 10 mM MOPS, 50 mM NaCl, 100 μM ZnCl_2 , at pH 8.0 and 5 mg/mL BSA (UltraPure, ThermoFisher Scientific, catalog no. AM2616); the BSA functions as a sacrificial protein to minimize non-specific adsorption of PBP to device walls. As binding to PBP weakens with increasing ionic strength, we carried out MeP kinetic assays at a reduced ionic strength of ~ 60 mM as compared to the ~ 600 mM used for cMUP kinetic assays. All BSA was exchanged into ultrapure water using an Amicon microcentrifuge concentrator (3K or 10K MWCO, Millipore, catalog no. UFC5003 and UFC5010, respectively) over multiple spin cycles to remove residual P_i .

Unlike the linear cMU standard curves, binding of P_i to PBP is defined by a single-site binding isotherm relating median fluorescence within each chamber to $[P_i]$:

$$I([P_i]) = 0.5A(K_D + [P_i] + [PS] - \sqrt{(K_D + [PS] + [P_i])^2 - 4[PS][P_i]}) + I(0\mu\text{M}) \quad (7)$$

where $I([P_i])$ is the median fluorescence at a given $[P_i]$, $[PS]$ is the concentration of PBP, K_D is the dissociation constant, A is the scaling factor necessary to relate fraction PBP bound to observed fluorescence, and $I(0\mu\text{M}[P_i])$ is the median fluorescence intensity of PBP in the absence of added P_i . To determine chamber-specific fitted parameters required to calculate $[P_i]$ from observed fluorescence, we then performed a nonlinear least-squares fit of observed intensities as a function of A , $I(0\mu\text{M}[P_i])$, $[PS]$, and K_D . Fitting all four parameters effectively provides an interpolation of the standard curve that makes it possible to determine $[P_i]$ from observed fluorescence within the pseudo-linear range of the sensor's response (rather than providing an accurate estimate of K_D).

On-chip MeP hydrolysis assays

We performed MeP hydrolysis reactions (9 total experiments: 5 Tier 1 (low $[E]$), 4 Tier 2 and 3 (high $[E]$) experiments) in the same reaction buffer as the standard curve (10 mM MOPS pH 8.0, 50 mM NaCl, 100 mM ZnCl_2 , 5 mg/mL BSA, and 30 μM PBP). To equilibrate the device, we flowed reaction solution through all chambers for 6–8 min with the Buttons closed. To start reactions, we opened the Button valves and imaged as described previously (*cf. Measuring cMUP hydrolysis on-chip*) to quantify fluorescence over time. Images were processed as for the cMUP assays with the exception that individual chambers were found using images from the highest $[P_i]$ in the standard curve.

To determine product concentration ($[P_i]$) from the measured fluorescence within each chamber, we substituted the fitted parameters from **Eq. 7** into the inverse of the isotherm function:

$$I^{-1}(I[P_i](t)) = [P_i](t) \quad (8)$$

where $I[P_i](t)$ and $[P_i](t)$ are the fluorescence intensity and $[P_i]$ at time t , respectively.

Measuring initial rates of MeP hydrolysis

To determine initial rates at each $[MeP]$, we used a similar algorithm to the determination of initial rates for cMUP-based assays. However, we limit the fitted range to include only calculated P_i concentrations below two-thirds of the total available $[PBP]$, as the accuracy of inferred $[P_i]$ from **Eq. 8** decreases sharply as PBP approaches saturation.

Rates of MeP hydrolysis were measured for substrate concentrations 0–50 μM . Having substrate concentrations both below and above the $[PBP]$ results in three different regimes under which we need to determine initial rates:

1. $[MeP] < [PBP]$
2. $0.3 [MeP] > (2/3)[PBP]$
3. $0.3 [MeP] < (2/3)[PBP]$

In regime 1, where $[MeP]$ is less than $[PBP]$ (*i.e.* where $[MeP] < 30 \mu M$) and for which we can follow the complete progress curve without saturating the PBP , we fit either $\leq 30\%$ of the total turnover or the first two points in cases where $\geq 30\%$ is turned over before the second point is acquired, as described for cMUP assays. In regime 2, we only fit points corresponding to $[PBP] < 20 \mu M$ (the linear regime of the calibration curve). In regime 3, we fit all points in which $[P_i] < 0.3 [MeP]$.

Initial rates were fit to the Michaelis-Menten equation (**Eq. 1**) as for cMUP hydrolysis.

Quality control and aggregation of MeP k_{cat}/K_M values across experiments

Quality control of MeP hydrolysis assays was performed identically to that for cMUP assays (*cf. Analysis and quality control of cMUP hydrolysis measurements*). To obtain final estimates of k_{cat}/K_M for MeP hydrolysis, we aggregated data from tier 1 (low $[E]$) and tiers 2 and 3 (high $[E]$) experiments (**Table S2**) as for the cMUP assays, with the following changes to the normalization procedure: (1) We calculated normalization factors using k_{cat}/K_M values rather than k_{cat} , as the low $[MeP]$ used and high MeP K_M values for most mutants preclude accurate estimation of k_{cat} and K_M ; (2) We normalized tier 1 (low $[E]$) experiments to one another based on the WT value in each experiment; (3) We normalized tier 2/3 (high $[E]$) experiments to one another based on the T79S value; and (4) We did not perform additional cross-Tier normalization as there were no mutants that could be resolved in both tier 1 (low $[E]$) and tier 2/3 (high $[E]$) experiments.

Determining significance of MeP k_{cat}/K_M effects

To determine the significance of observed changes in MeP k_{cat}/K_M relative to WT, we used the same procedures for bootstrapping probability estimates and defining upper limits as described above for cMUP measurements.

Off-chip MeP hydrolysis assays

As for cMUP, we compared rates obtained on-chip for active site mutants hydrolyzing Me-P with rates obtained for the same recombinant enzymes expressed off-chip. Off-chip experiments used the same substrate, P_i , and PBP concentrations as on-chip measurements and detected build-up of P_i via PBP fluorescence using a Tecan Infinite M200 plate reader at excitation and emission wavelengths of 415 nm and 470 nm, respectively.

Quantifying enzyme activity as a function of temperature and $[Zn^{2+}]$ during expression

To measure the dependence of catalytic activity on expression temperature, we carried out on-chip PURExpress reactions at either 23°C or 37°C for 45 min. During the last 10 min of this reaction, we flowed reaction buffer containing 500 μM chloramphenicol. After the 45 min incubation, we closed the Sandwich valves and opened the Necks, and allowed the enzyme to fold for 90 min at 23°C in the presence of the chloramphenicol, thereby halting translation to prevent formation of a mixture of enzymes produced at different temperatures. After the 90 min incubation, we opened the Buttons to bind enzyme to antibody-coated surfaces for 15–60 min and then closed the Buttons and performed the standard flush using normal PafA reaction buffer.

To measure the dependence of catalytic activity on added $ZnCl_2$ during expression, we substituted either 10 or 1000 μM $ZnCl_2$ for the 100 μM $ZnCl_2$ typically added to PURExpress reactions and flowed reaction buffer with the same concentration of $ZnCl_2$ during expression. For the subsequent enzymatic activity assays, we switched to standard reaction buffer containing 100 μM $ZnCl_2$ and carried out all assays as for standard cMUP hydrolysis experiments.

In both cases, we again measured Michaelis-Menten parameters for cMUP hydrolysis under standard on-chip reaction conditions, as described above. For all mutants, we aggregated data across experiments and tiers largely as described previously to yield median estimates of k_{cat} , K_M , and k_{cat}/K_M at each expression temperature and $[Zn^{2+}]$. However, data aggregation procedures did not cull for mutants based on the percentage of observations exceeding LLoD thresholds due to a more limited number of replicates. In addition, this limited number of replicates precluded determination of significance using bootstrap hypothesis testing. Instead, we estimated significance by comparing the overall distribution of the ratios of the median k_{cat}/K_M values at the two temperatures and Zn^{2+} concentrations, normalized to the median WT PafA k_{cat}/K_M for each experiment, to the distribution of the ratios between experimental replicates of the same mutant under identical conditions (Main Text **Fig. 3, G and I**). These temperature effect (T-Effect) and zinc-effect (Zn-Effect) ratios are defined below (**Eqs. 9 and 10**, respectively).

$$\text{T-Effect} = \frac{\left[\frac{(k_{\text{cat}}/K_M)^{\text{Mutant}}}{(k_{\text{cat}}/K_M)^{\text{WT}}} \right]^{23^\circ\text{C}}}{\left[\frac{(k_{\text{cat}}/K_M)^{\text{Mutant}}}{(k_{\text{cat}}/K_M)^{\text{WT}}} \right]^{37^\circ\text{C}}} \quad (9)$$

$$\text{Zn-Effect} = \frac{\left[\frac{(k_{\text{cat}}/K_M)^{\text{mutant}}}{(k_{\text{cat}}/K_M)^{\text{WT}}} \right]^{1000 \mu\text{M Zn}^{2+}}}{\left[\frac{(k_{\text{cat}}/K_M)^{\text{mutant}}}{(k_{\text{cat}}/K_M)^{\text{WT}}} \right]^{10 \mu\text{M Zn}^{2+}}} \quad (10)$$

We plotted the top 5th percentile of T-Effects as spheres on the structure of PafA (Fig. 3F and G). The number of mutants for which we measured the Zn-Effect was lower than that in the T-Effect experiments; we therefore used a less stringent threshold (top 20th percentile of Zn-Effects) when plotting effects on the structure (Fig. 3, H and I).

Characterization of the misfolded state

Further characterization of mutants off-chip *in vitro* To test if on-chip expression alters enzyme folding, we expressed and assayed a subset of library variants (9 Valine, 8 Glycine, 1 Active Site, and the WT) off-chip *in vitro* (Table S4). These mutants spanned more than an order of magnitude in apparent k_{cat}/K_M MeP and included mutants with and without likely fraction active effects (Main Text Fig. 3C, closer to the solid blue line and dashed blue line, respectively). In parallel, we expressed and assayed the catalytically inactive Gly library mutant T79G as a control for any background activity stemming from contaminating phosphatase activity in PURExpress.

Off-chip expression via *in vitro* transcription/translation We expressed variants in Table S4 *in vitro* with PURExpress off chip. First, we gently mixed four parts of PURExpress component A with 3 parts of PURExpress component B (a $\frac{10}{7}$ X stock) and incubated on ice for 45 min. We then added 40 U/L recombinant ribonuclease inhibitor (0.8 U/ μ L final), 1 mM ZnCl₂ (100 μ M final), and nuclease-free water to bring the A and B two-component mixture to 1X. Then, we partitioned 11- μ L aliquots of this master mix into PCR tubes and added 0.5 μ L of variant plasmid DNA to each. We expressed enzyme in a thermocycler at 37°C for 45 min, followed by a 90 min incubation at room temperature in the dark. To quantify protein yields, we diluted the full reaction volumes with PafA reaction buffer (100 mM MOPS, pH 8, 500 mM NaCl, 100 μ M ZnCl₂) to 200 μ L total, and measured the GFP fluorescence intensity using a Denovix fluorometer/spectrophotometer (model DS-11 FX+). Enzyme concentration was calculated using an eGFP standard curve measured on the same instrument, prepared using commercial eGFP (Biovision, catalog no. 4999).

pNPP hydrolysis assays We measured activities of enzymes expressed *in vitro* via turnover assays with the substrate pNPP, a convenient chromogenic substrate with a high dynamic range, as off-chip measurements require substantially more material and would quickly deplete stocks of our synthesized cMUP substrate. The fold-change in apparent activities after expression at high and low temperature should be identical regardless of the choice of substrate. First, we diluted the IVTT expression mixture for each enzyme an additional 10-fold in water and prepared kinetic assays as follows: we mixed 100 μ L of 2X PafA

reaction buffer with 50 μL of 4X pNPP substrate at concentrations ranging from 31.2–2000 μM in a 96-well optically-clear plate and then added 50 μL of the diluted IVTT reactions (200- μL reactions). We then measured absorbance at 400 nm over time using a Tecan Infinite M200 plate reader, fit initial rates of turnover to linear models, and fit the Michaelis-Menten equation to linear rates as a function of substrate concentration as described above (Eq. 1; using KaleidaGraph software, version 4.5, Synergy Software). Finally, we calculated k_{cat}/K_M for each mutant using the fit enzyme-concentration-independent Michaelis-Menten parameters and enzyme concentrations inferred from the eGFP quantifications described above.

Native polyacrylamide gel electrophoresis of temperature-sensitive mutants To assess the temperature-dependence of misfolding off-chip, we expressed WT PafA and four temperature-sensitive mutants (Y103G, G130V, T189G, and S190G) with PURExpress for 45 min at either 37°C or 22°C, respectively. Expression was halted by doubling the reaction volumes with 0.5 mM chloramphenicol, and reactions were then incubated at room temperature for 90 min in the dark. This procedure mimicked the protocol employed on-chip for expression at low and high temperature.

Aliquots (two parts) of each sample were mixed with one part 3X native gel loading buffer (62 mM Tris, 0.01% (w/v) bromophenol blue, and 40% (v/v) glycerol at pH 6.8) and loaded onto a polyacrylamide gel (BioRad, Mini-PROTEAN 4–20% TGX gel, catalog no. 4561096) and electrophoresed at 120 V, 4°C, for 3 h in a running buffer containing 25 mM Tris and 190 mM Glycine at pH 8.3. Gels were characterized via in-gel fluorescence imaging (measuring eGFP fluorescence) with a Typhoon FLA 9500 imaging system (excitation at 473 nm with a long pass blue, LPB 510LP, emission filter).

Thermolysin sensitivity assays of temperature-sensitive mutants To test if mutants exhibiting reduced activity when expressed at higher temperatures were more susceptible to thermolysin proteolysis, we diluted expression mixtures from WT and five temperature-sensitive mutants (Y52G, Y103G, G130V, T189G, and S190G) into PafA reaction buffer. We then performed native gel electrophoresis with samples of WT and mutant PafA expressed at low and high temperature both with and without treatment with thermolysin protease. Protease-treated samples were prepared as follows: To each sample of IVTT expression product diluted into PafA reaction buffer, we added a 100X stock solution of 10 mg/mL thermolysin (Sigma-Aldrich, catalog no. T7902) containing 10 mM CaCl_2 and 2.5 M NaCl to give a final reaction containing 0.05 mg/mL thermolysin (200-fold dilution). Reactions were incubated at room temperature for 10 min and then quenched by adding an equivalent volume of 50 mM sodium EDTA (to inactivate thermolysin via chelation of calcium). Untreated (no thermolysin cleavage) samples consisted of dilutions of the original IVTT mixture in PafA reaction buffer. Then, we loaded both thermolysin treated and untreated samples and electrophoresed in a polyacrylamide gel under non-denaturing conditions, as described above. In-gel fluorescence of eGFP-bearing constructs was quantified with a Typhoon imaging system, also as described previously.

Separately, we performed substrate turnover assays with WT and mutant PafAs both in the presence and absence of thermolysin to correlate observed loss in native-gel band

intensity with loss of activity. Expressed enzymes diluted in PafA reaction buffer were further diluted 10-fold in water, and 200- μ L reactions were prepared as follows: to 100 μ L of 2X PafA reaction buffer, 50 μ L of 800 μ M pNPP, either 2 μ L of water (no thermolysin) or 2 μ L of 100X thermolysin stock solution (with thermolysin, final concentration of 0.1 mg/mL thermolysin), and 50 μ L of diluted enzyme were added and the reactions were mixed. Reaction progress was monitored via time-dependent changes in absorbance at 400 nm, and no significant curvature was observed over at least 15 minutes (a time frame longer than the thermolysin cleavage reactions complementarily characterized via native gel electrophoresis). Initial rates of hydrolysis were fit as described for other off-chip assays.

Further characterization of possible misfolding mutants in *E. coli*

To test if misfolding-induced activity changes also arise *in vivo*, we recombinantly expressed 22 variants in *E. coli*: a subset of the 14 variants characterized *in vitro* off-chip (5 Val, 7 Gly, 1 Active Site, and the WT), an additional 7 variants (4 Val and 3 Gly), and T79G as a control for background activity from contaminating phosphatases *E. coli* cell lysate. After purification, we assayed each for hydrolytic activity towards pNPP (**Table S5**).

Recombinant *E. coli* expression of enzymes We expressed PafA-eGFP mutant variants **Table S5** in *E. coli* using non-induced expression of the PURExpress vector. Competent BL21(DE3) *E. coli* cells (made in house) were transformed with mutant or WT PafA-eGFP constructs (the same plamid stocks used for on- and off-chip expression *in vitro*), plated onto LB agar with 50 mg/mL carbenicillin, and grown overnight at 37°C. For each mutant, 20 mL LB media with carbenicillin was inoculated with a single colony, and cultures were grown overnight at 37°C (high temperature expressions). To express enzyme at room temperature, we used 100 μ L of each high-temperature expression overnight culture to inoculate 10 mL LB with carbenicillin, and those cultures were grown overnight at room temperature (room temperature expressions).

The high temperature expression cultures were partitioned into two 10-mL aliquots and pelleted via swinging bucket centrifugation. Plasmid was isolated for one aliquot (each mutant) using a Qiagen miniprep kit and sequence verified with Sanger sequencing; the other aliquot of each high-temperature expression culture was frozen at -20°C for subsequent kinetic assays, described below. The 10-mL room temperature expression cultures were similarly pelleted and frozen for kinetic assays.

Frozen pellets were defrosted and re-pelleted in a swinging bucket centrifuge at 4°C, supernatant was decanted, and the pellets were re-suspended in 1 mL of 10 mM MOPS, 50 mM NaCl, 100 M ZnCl₂ at pH 8 (PafA storage buffer). The suspension was then re-pelleted in a bench-top centrifuge and again suspended in 1 mL PafA storage buffer. Cells were lysed via sonication (using a Fisherbrand Model 705 Sonic Dismembrator), on ice, as follows: 5 repetitions of 5 s on, at 25% power, and 30 s rest. The crude lysate was pelleted and the supernatant was isolated and clarified by centrifugation in a bench-top centrifuge for 10 min at 13,000 rpm and 4°C. Enzyme concentration in the clarified supernatant was quantified using eGFP fluorescence as measured using a DeNovix spectrophotometer/fluorometer and using the eGFP standard described previously. The component of

total eGFP signal from full-length enzyme-eGFP construct was assessed via in-gel fluorescence (denaturing with sodium dodecyl sulfate, BioRad, Mini-PROTEAN 4–20% TGX polyacrylamide gel) using a Typhoon imaging system, as described previously, and found to be approximately comparable to or greater than the signal arising from free eGFP and truncated enzyme-eGFP. This suggested that eGFP fluorescence-inferred enzyme concentration was comparable with the actual concentration of full-length enzyme construct.

pNPP hydrolysis assays The clarified supernatant of each mutant expressed *in vivo* (cell lysate) was further diluted 5-fold into PafA storage buffer, then diluted 10-fold into water. Kinetic assays were then performed as follows: 75 μL of 2X PafA reaction buffer was mixed with 37.5 μM pNPP substrate at concentrations ranging from 31.2–2000 μM and 37.5 μL of diluted cell lysate (150- μL reactions) in a 96-well optically-clear plate. Product turnover measurement, initial rate fitting, and Michaelis-Menten parameter calculation were performed as described for assays of *in vitro* expressed enzymes.

Expression of non-eGFP-tagged WT PafA and Y103G, and circular dichroism measurements We over-expressed WT PafA and Y103G constructs with a Strep-tag in *E. coli* at 37°C and room temperature and purified constructs, as previously described in (16). Activities were measured using 100 μM pNPP, and concentrations of purified enzyme were estimated by measuring absorption at 280 nm ($\epsilon = 101560\text{M}^{-1}\text{cm}^{-1}$). Aliquots of enzyme stocks in PafA storage buffer were then buffer-exchanged into both 10 mM Tris at pH 8 and 10 mM KP_i at pH 8, respectively. Circular dichroism (CD) spectra were obtained for concentrated enzyme stocks in PafA storage buffer, Tris, and potassium phosphate buffers via a J-815 Jasco Spectrophotometer from 210–250 nm (1 nm bandwidth, 50 nm/min scanning speed) at 20°C in a 0.1 cm cuvette (Hellma Analytics). Additionally, WT PafA expressed at room temperature was subjected to incubation with urea for 2 weeks, then characterized by CD to assess loss of secondary structure. This was performed by incubating concentrated protein in reaction buffer with urea on the benchtop, and CD was performed with urea present in $\frac{1}{2}$ X reaction buffer, as described (Fig. S25).

Deconvolving mutational effects on folding and catalysis

Theory and derivation of the expected relationship between the observed MeP and cMUP $k_{\text{cat}}/K_{\text{M}}$ for catalytic and misfolding effects is detailed in **Supplementary Text S2** and **S3**.

Determining statistical significance of fraction active and catalytic effects within the active fraction

We determined the significance of f_{a} and intrinsic $k_{\text{cat}}/K_{\text{M}}$ effects using a modification of the bootstrap hypothesis testing procedure described above. As determination of the active fraction (f_{a}) depends on measured $k_{\text{cat}}/K_{\text{M}}$ values for both cMUP and MeP hydrolysis, we: (1) pooled the mutant and wild-type MeP $k_{\text{cat}}/K_{\text{M}}$ observations, (2) pooled the mutant and wild-type cMUP $k_{\text{cat}}/K_{\text{M}}$ observations separately, and then (3) determined bootstrap samples of MeP and cMUP measurements by resampling with replacement, and then calculated f_{a} and intrinsic MeP and cMUP $k_{\text{cat}}/K_{\text{M}}$ values using **Eqs. 31–35** and the number of MeP

(m) and cMUP (n) replicates for the mutant and WT, respectively. We then calculated the difference between the medians of f_a and $k_{\text{cat}}/K_M^{\text{chem}}$ for the mutant and WT bootstrap samples ($t^* = |m - n|$), iterated this procedure 100–1000 times, and computed a p -value using Eq. 6.

As $k_{\text{cat}}/K_M^{\text{chem}}$ depend on both cMUP and MeP k_{cat}/K_M , and its dependence on these two observed rate constants is non-linear, their errors are typically larger than those on the observed cMUP and MeP k_{cat}/K_M measurements. We therefore use $p < 0.05$ to determine $k_{\text{cat}}/K_M^{\text{chem}}$ effects, with the caveat that we expect more false positives. The relationship between f_a and cMUP and MeP k_{cat}/K_M is more linear, so we use our standard $p < 0.01$ to determine f_a effects.

Measuring hydrolysis of the non-cognate substrate MecMUP

We assayed rates of MecMUP hydrolysis (8 total experiments: 5 Tier 1 (low [E]) and 3 Tier 2 and 3 (high [E]) experiments) using a procedure similar to that used for cMUP hydrolysis, again acquiring cMU standard curves at the start of each experiment. However, we modified the pipeline for obtaining initial rates of MecMUP hydrolysis in two ways. First, the non-cognate MecMUP hydrolysis reaction catalyzed by WT PafA is 10^5 -fold slower than cMUP hydrolysis. Therefore, to maximize substrate turnover within a reasonable acquisition time, we measured all rates at high [E] (10–30 nM) and high [S] (0.5–2 mM) over 1–3 hr/assay. Second, trace amounts of the monoester (cMUP) within MecMUP stocks (~0.1% mol/mol) led to an initial burst phase (corresponding to fast hydrolysis of trace cMUP monoester) followed by a longer linear phase (corresponding to slower hydrolysis of MecMUP diester). We therefore fit fluorescent product buildup to a function including a linear term for MecMUP hydrolysis and the integrated form of the Michaelis-Menten equation (86) for trace cMUP hydrolysis:

$$[\text{cMU}](t) = v_i^{\text{MecMUP}} t + [\text{cMUP}]_0 - K_M W\left(\frac{[\text{cMUP}]_0}{K_M} e^{\frac{[\text{cMUP}]_0 - k_{\text{cat}}[E]t}{K_M}}\right) \quad (11)$$

Here, $[\text{cMU}](t)$ is the concentration of fluorescent product at time t , v_i^{MecMUP} is the initial rate of MecMUP hydrolysis, $k_{\text{cat}}^{\text{cMUP}}$ and K_M^{cMUP} are the Michaelis-Menten parameters of cMUP hydrolysis, [E] is the enzyme concentration, $[\text{cMUP}]_0$ is the contaminating concentration of cMUP in the assay present during the first fluorescence measurement, and W is the Lambert Omega function (86). To reduce the number of free parameters, we substituted measured $k_{\text{cat}}^{\text{cMUP}}$ and K_M^{cMUP} for cMUP hydrolysis for each mutant and restrained $[\text{cMUP}]_0$ to be $\leq 0.1\%$ of [MecMUP]. We then determined v_i^{MecMUP} for each mutant by non-linear least squares fitting of the entire progress curve.

To measure k_{cat}/K_M for MecMUP hydrolysis for nearly all mutants, we measured initial rates at 3–4 MecMUP concentrations from 500–2000 μM and fit these to the Michaelis-Menten equation. For the tier 3 (high [E]) library, we measured rates by quantifying MecMUP hydrolysis at a single high concentration (2000 μM) over 22 hours. For this experiment, we determined k_{cat}/K_M by simply dividing the fitted rate by the [E] and [MecMUP] concentrations as [MecMUP] was not appreciably depleted over the total measurement time (with the assumption of being subsaturating).

Quality control of MecMUP hydrolysis measurements

Quality control of MecMUP hydrolysis assays was carried out in a similar manner to cMUP assays with two differences: (1) the local LLoD interpolations considered only T79G and Skipped chambers and not K162A (as K162A has a WT-like rate of diester hydrolysis), and (2) we culled any chambers with measured MecMUP rates for a given mutant within 5-fold of the cMUP rate during the last 5 timepoints of the reaction, reasoning that these rates likely represent hydrolysis of trace monoester contaminant.

Obtaining final estimates of MecMUP hydrolysis and determining statistical significance

After quality control, MecMUP assays were aggregated and normalized in an analogous manner to the cMUP and MeP measurements, but with the following differences: (1) K162A was used as the normalizing mutant instead of WT, as its MecMUP $k_{\text{cat}}/K_{\text{M}}$ is WT-like, and every experiment contained multiple replicates. (2) Instead of a two-stage normalization procedure, K162A was used to normalize all experiments across all tiers. As MecMUP hydrolysis is intrinsically orders of magnitude slower than cMUP and MeP hydrolysis, there were no 2-pt fits.

To determine the statistical significance of MecMUP $k_{\text{cat}}/K_{\text{M}}$ effects, we again used bootstrap hypothesis testing to compare mutant $k_{\text{cat}}/K_{\text{M}}$ distributions relative to that of wild-type PafA, as described for cMUP and MeP assays above.

Functional Component 1: Effects through the O2 phosphoryl oxygen atom

We quantified Functional component 1 (FC1) for each mutant by comparing observed fold-changes in $k_{\text{cat}}/K_{\text{M}}$ from the WT value for MecMUP versus MeP hydrolysis:

$$\text{FC1} = \Delta \text{MecMUP} / \Delta \text{MeP} \quad (12)$$

where

$$\Delta = \frac{k_{\text{cat}}/K_{\text{M}}^{\text{mutant}}}{k_{\text{cat}}/K_{\text{M}}^{\text{WT}}} \quad (13)$$

for MeP and MecMUP hydrolysis. As noted in the main text, as misfolding is expected to affect both MeP and MecMUP equally, we compared the observed $k_{\text{cat}}/K_{\text{M}}$ values rather than the values corrected for f_{a} effects.

FC1 values for mutants below the dynamic range of on-chip assays

There are 3 instances in which upper limits in MeP and MecMUP result in limits on calculated FC1 values:

(1) MecMUP $k_{\text{cat}}/K_{\text{M}}$ upper limit but MeP $k_{\text{cat}}/K_{\text{M}}$ measured. In this case, rates of MecMUP hydrolysis are much slower than cMUP and MeP, limiting assay dynamic range. The calculated value therefore represents an upper limit; however, as these mutants could

have FC1 values anywhere between 0 and this upper limit, we do not consider them significant in downstream analyses.

(2) MecMUP k_{cat}/K_M measured, but MeP k_{cat}/K_M upper limit, resulting in lower FC1 limits. We conservatively estimate the significance of these mutants using this lower limit value, as true FC1 values must actually be larger and more significant.

(3) Both MecMUP and MeP k_{cat}/K_M upper limits, resulting in indeterminate FC1 values and significance.

Determining statistical significance of FC1 effects

We determined the statistical significance of FC1 effects using bootstrap hypothesis testing, as follows. For each mutant, (1) we merged the observations of mutant MeP and MecMUP k_{cat}/K_M with the WT observations, (2) randomly sampled from these observations to generate bootstrapped observations with the same number of mutant observations in both assays (MecMUP_{mutant}^{*} and MeP_{mutant}^{*}), (3) similarly generated bootstrapped observations with the same number of WT replicates in both assays (MecMUP_{WT}^{*} and MeP_{WT}^{*}), (4) calculated the medians of these bootstrap observations, and (5) calculated the differences (t^*) between the MecMUP and MeP k_{cat}/K_M medians for the mutant and WT from the bootstrap observations:

$$\delta_{\text{mutant}} = \log_2 \widetilde{\text{MecMUP}}_{\text{mutant}}^* - \log_2 \widetilde{\text{MeP}}_{\text{mutant}}^* \quad (14)$$

$$\delta_{\text{WT}} = \log_2 \widetilde{\text{MecMUP}}_{\text{WT}}^* - \log_2 \widetilde{\text{MeP}}_{\text{WT}}^* \quad (15)$$

$$t^* = | \delta_{\text{mutant}} - \delta_{\text{WT}} | \quad (16)$$

We then repeated this process up to 500 times and calculated the p -value as the number of times the bootstrapped difference was greater than the difference between the medians of the experimentally-observed distributions (t^{obs}).

$$p = \frac{\#(t_{\text{obs}} < t^*)}{N} \quad (17)$$

Determination of residues within each K162/R164 interaction shell

To define residues within K162 and R164 interaction shells, we used GetContacts (<https://getcontacts.github.io/>) as follows. First, we ran GetContacts using the WT PafA crystal structure (PDBID: 5TJ3) as input to identify all the potential contacts between residues in PafA. We defined the active site to consist of all residues making direct contacts to the substrate (T79, N100, K162 and R164) as well as the six catalytic Zn²⁺-liganding residues. We then defined the second shell as the set of residues having at least one contact to either K162 or R164 (but excluding the active site residues themselves).

To define the third shell, we then determined the set of residues making at least one contact to any of the second shell residues, including contacts between residues via bridging waters. As some of the second shell residues interact with one another, we needed to

remove these from the third shell set. We therefore determined the subset of the third shell residues not present in either the second shell or the active site set. Higher order shells were also determined by enumerating the full set of contacts and then finding the unique subset of residues not present in any lower interaction shells.

In addition to the K162 and R164 interaction shells, we also defined the sets of residues within each interaction shell of any of the active site residues (T79, N100, K162 and R164 and the catalytic Zn²⁺-liganding residues) in an analogous manner.

Determination of surface-exposed residues and calculation of depth from surface

Surface-exposed residues were determined by calculating relative accessible surface area (ASA) using Biopython (Bio.PDB.DSSP) (87) and the normalization values of Tien *et al.* (88). Residues having a relative ASA >0.16 were defined as surface-exposed (89). The N- and C-terminal residues unmodeled in the PafA crystal structure were also assumed to be solvent exposed. Separately, depth of each C-alpha to a reduced surface was calculated using Biopython (Bio.PDB.ResidueDepth) using the MSMS program (87, 90).

Measuring phosphate inhibition constants using HT-MEK

We determined inhibition constants K_i for inorganic phosphate (P_i) via competitive inhibition assays in which we varied inhibitor concentrations at a constant [cMUP] (12 total experiments: 8 Tier 1 (low [E]) and 4 Tier 2 and 3 (high [E]) experiments). We performed tier 1 (low [E]) and tier 2 (high [E]) assays for the full valine and glycine-scanning libraries at either 10 or 50 μ M cMUP in 100 mM MOPS (pH 8.0) with 500 mM NaCl and 100 μ M ZnCl₂ at 10–12 inhibitor concentrations ranging from 0–8000 μ M. For tier 3 (high [E]) assays, we reduced the number of inhibitor concentrations to 6 due to the longer acquisition times required for each measurement. When possible, we included replicate assays (typically at 0 μ M P_i) to control for activity loss over time. On-chip assays were otherwise acquired as previously described for cMUP.

For each chamber, we quantified initial rates of product formation at each inhibitor concentration as described previously. We then determined inhibition constants for each chamber by fitting the observed rates to a model of competitive inhibition:

$$v_i([I]) = \frac{v_i^{\text{uninhibited}}}{1 + [I]/K_i} \quad (18)$$

where v_i is the initial rate at a given inhibitor concentration, K_i is a fitted inhibition constant, and $v_i^{\text{uninhibited}}$ is a fitted initial rate in the absence of inhibitor.

As for the other measurements, all data, fits and quality control flags for each chamber within each experiment are in the per-experiment CSV and PDF files in the **OSF Repository Data** (74) and Fordyce Lab website (<http://www.fordycelab.com/publication-data>), respectively.

Obtaining final estimates of phosphate inhibition constants and determining significance

To obtain final estimates of phosphate inhibition constants for each mutant, we performed quality control and aggregated data across experiments in a similar manner as for cMUP, MeP, and MecMUP experiments. To pass all quality control filters, we required: (1) that chambers contain $[E] > 0.3$ nM, (2) that eGFP spots be free of apparent defects or artifacts upon visual inspection, (3) that initial rates were >5 -fold above the LLoD (calculated using the $0 \mu\text{M}$ $[P_i]$ assay), and (4) that inhibition curves included <6 2-pt fits. In addition, we only considered tier 1 (low $[E]$) and 2 (high $[E]$) measurements for mutants in which $>40\%$ of replicates passed the LLoD filter during that tier.

We corrected for any systematic errors in either the stock phosphate concentrations or buffer pH between experiments by normalizing fitted K_i values to the median K_i of the 3–17 WT replicates within each experiment that passed quality control. As the R164A K_i is a lower limit, we could not apply a two-stage normalization analogous to that for cMUP; therefore, the K_i values from tier 2 and 3 (high $[E]$) experiments lacking WT replicates were not normalized. The per-experiment median WT K_i s (and thus normalization factors) were all within ~ 2 -fold of the cross-experiment median.

Apparent competitive inhibition constants (K_i^{obs}) are sensitive to substrate K_M , with the magnitude of the delta between $K_i^{\text{obs}}(P_i)$ and $K_i^{\text{intrinsic}}(P_i)$ related to K_M of cMUP for our mutants. In traditional competitive inhibition assays, the substrate concentration is chosen to be $[S] < K_M$, such that $K_i^{\text{obs}} \approx K_i^{\text{intrinsic}}$. Here, we used 10 and 50 μM cMUP concentrations to meet this criterion for the majority of mutants. In addition, to correct for systematic overestimation of measured (observed) $K_i(P_i)$ values arising for mutants with low cMUP K_M values, we used the Cheng-Prusoff relationship, which relates the intrinsic competitive K_i to the observed competitive K_i and substrate K_M :

$$K_i = \frac{K_i^{\text{obs}}}{1 + [S]/K_M} \quad (19)$$

We corrected each individual measurement using the median cMUP K_M for that mutant, the experimental [cMUP] concentration used, and **Eq. 19**. After correction, we combined all K_i measurements and calculated median estimates for each mutant. Raw fitted K_i values are reported in the per-experiment CSV and PDF summaries, and Cheng-Prusoff corrected values are given in the aggregated estimate summary CSV and PDF files.

Identifying lower and upper K_i limits We identified 3 mutants for which K_i values were lower limits and 6 for which K_i values were upper limits. Lower K_i limits arise when $K_i \gg$ the highest $[P_i]$ assayed. During the aggregation process, we flagged individual measurements as lower limits if the observed fit K_i was >2 -fold above the highest $[P_i]$ used in the experiment and set a conservative lower limit of the K_i to be 2-fold above the highest $[P_i]$. In addition, we defined the median K_i estimate for a given mutant as a lower limit if $>50\%$ of the underlying measurements for that mutant were K_i lower limits.

Upper limits in K_i can arise when: (1) the fit K_i is below the lowest non-zero $[P_i]$ concentration used (1 μM in on-chip assays), or (2) when measured cMUP K_M values are

upper limits, propagating a limit through (preventing accurate correction via) the Cheng-Prusoff relationship described above. In the first case, as for the lower limits, we defined the median K_i value as an upper limit if >50% of the individual replicates were K_i upper limits and set the K_i of these replicates to be 2-fold less than the lowest [P_i]. In the second case, if the median cMUP K_M was a lower limit, we automatically denoted the median K_i value as an upper limit, as this will introduce systematic error on all K_i replicates.

Determining significance of K_i measurements We again determined the significance of mutational effect estimates using bootstrap hypothesis testing comparing the distribution of corrected K_i values to the WT corrected K_i distribution (as described above for cMUP measurements). We conservatively estimated the statistical significance of upper and lower K_i limits in the same way, as limit values will only underestimate the true significance. For mutants with catalytic rates below the lower limit of detection, we cannot determine a significant change in K_i of phosphate binding and, therefore, do not report either K_i or significance.

PafA phylogenetic analysis

Generating a multiple sequence alignment of public database and metagenomic PafA-like AP superfamily member sequences

Obtaining, aligning, and filtering publicly-available sequences To assess conservation within metagenomic sequences, we first generated a heavily curated alignment of PafA-like sequences originating in public databases.

To identify candidate sequences, we first assembled a comprehensive collection of 156,929 alkaline phosphatase (AP) superfamily members from the UniProtKB database (91). Next, we added the following additional AP superfamily sequences from publicly available databases: (1) sequences that possess the appropriate AP fold, as defined by the CATH (92) database (the 3.40.720.10 domain), (2) sequences with sequence patterns manually selected from the InterPro (93) and Pfam (94) databases that are associated with AP functions (IPR000917, IPR001952, IPR002591, IPR004245, IPR006124, IPR007312, IPR010869, IPR013973, IPR017849, IPR017850, IPR026263, IPR029879, IPR029881, IPR029885, IPR029889, IPR029890, IPR029895, IPR029896, IPR029897, IPR032506, PF00245, PF00884, PF01663, PF01676, PF02995, PF04185, PF07394, PF08665, PF14707, PF16347), and (3) sequences from the UniProtKB/SwissProt, BRENDA (www.brenda-enzymes.org) (95) and Sabio-RK (96) databases with any of the following EC numbers (2.7.8.20, 2.7.8.21, 2.7.8.43, 2.7.8.44, 3.1.3.1, 3.1.3.2, 3.1.3.27, 3.1.3.39, 3.1.3.54, 3.1.4.1, 3.1.4.3, 3.1.4.12, 3.1.4.38, 3.1.4.39, 3.1.6.1, 3.1.6.12, 3.1.6.13, 3.1.6.14, 3.1.6.2, 3.1.6.4, 3.1.6.4, 3.1.6.6, 3.1.6.8, 3.1.7.6, 3.10.1.1, 3.11.1.2, 3.6.1.29, 3.6.1.9, 5.4.2.1, 5.4.2.12, 5.4.2.7).

Next, we used the Structure Function Linkage Database (SFLD) (97) to generate a sequence similarity network (SSN) of the entire superfamily, and used a previously described procedure (98–100) to delineate the relevant SSN cluster that includes PafA. Briefly, by mapping experimentally validated reactions to the SSN, we evaluated different edge inclusion cutoffs to identify a threshold that: (1) maintains PafA homologs in one cluster, and

(2) separates this PafA cluster from other clusters that include sequences that are clearly not PafA-like (*e.g.* annotated in SwissProt to catalyze a different reaction). This process yielded a list of 1,384 PafA homologs used for subsequent analysis.

Next, we aligned a subset of these initial 1384 PafA-like sequences. First, we clustered sequences by identity using CD-HIT (101) and then extracted unique representatives from 75% identity clusters for subsequent analysis. Next, we aligned these representatives, including WT PafA, with PASTA (<https://github.com/smirarab/pasta>) (102) using the following non-default parameters: “--num-cpus=6, -datatype=Protein”.

The resulting alignment was restricted to sequences bearing a subset of possible residue identities at positions corresponding to the nucleophile and Zn²⁺ ligands in the PafA reference sequence (Uniprot Accession Q9KJX5). This gappy restricted alignment was then trimmed by removing alignment positions at which gaps existed at $\geq 95\%$ of sequences, and both PafA or the other structurally-characterized relative SPAP (Uniprot Accession A1YYW7) were gapped. The resulting alignment was then de-gapped and re-aligned using PASTA (using the same non-default parameters) to yield a final curated “public database alignment” of 478 sequences.

Obtaining, aligning, and filtering metagenomic sequences To identify metagenomic PafA-like sequences, we queried the IMG/M database (August 2018) (103) with a profile Hidden Markov Model (HMM) generated from the multiple sequence alignment of 478 highly-curated PafA-like sequences collected from public databases (“public database alignment”) with `hmmbuild` (of HMMER, www.hmmer.org) using default arguments. The query was performed with National Energy Research Scientific Computing Center (NERSC) resources and enabled by the JGI-EMSL Facilities Integrating Collaborations for User Science (FICUS) program (<https://jgi.doe.gov/user-programs/program-info/ficus-overview/>). This query returned 2,374,441 sequences that were subsequently restricted to 34,654 sequences meeting the following criteria: 250–1200 residues in length, an HMM bitscore of at least 120, and bearing a Met, Val, or Leu N-terminal residue.

Filtered sequences were concatenated with the public database sequences originally collected (giving rise to the “public database alignment”) and aligned with UPP (104). Creating this “large alignment” first required a smaller “backbone alignment,” which we generated from representative metagenomic sequences identified via CD-HIT aligned initially using PASTA, then heuristically subdivided into sub-alignments and re-aligned and merged using MAFFT (105). Finally, we removed sequences in the crude backbone alignment contributing to excessive gappiness via a heuristic-based procedure to generate the final backbone alignment composed of 1402 sequences. Then, we generated a Maximum Likelihood (ML) tree using this “backbone alignment” using FastTree (106) with default parameters. The “large alignment” was generated using UPP with the following non-default parameters: “-t \$BBTree -d \$NumCores -m amino”, where \$BBTree refers to the tree inferred from the “backbone alignment,” and \$NumCores was the number of logical cores employed in the calculation. This yielded an alignment of 36,036 sequences with many gapped positions.

The “large alignment” was subsequently restricted to non-gapped positions in the reference PafA sequence (Uniprot Accession Q9KJX5) to yield a “de-gapped large alignment”.

This masked alignment was further filtered on the presence of the canonical PafA active site residues (T79, N100, K162, and R164) and removing sequences for which PafA non-gapped positions consisted of $\geq 20\%$ gapped identities. This procedure yielded a sieved subset of 14,505 aligned metagenomic and public database sequences (the “culled trimmed metagenomic alignment”) used for downstream analyses.

We generated a ML tree of culled PafA-like metagenomic and public database (“culled trimmed metagenomic alignment”) sequences using FastTree as described above. The resulting un-rooted tree was plotted using the ggtree package in R (**Fig. S67**) (107).

Calculating phylogenetic conservation

To test if on-chip measured functional parameters were correlated with conservation, we used the “culled trimmed metagenomic alignment” described above to quantify information content within the alignment at each position within the PafA ORF. We calculated information content using the `information_content` function in the `Bio.Align.AlignInfo` module of Biopython (87) using a custom amino-acid frequency table derived from the amino acid composition of UniProtKBSwiss-Prot (<https://web.expasy.org/protscale/pscale/A.A.Swiss-Prot.html>) and ignoring the following characters: “-”, “X”, “B”, “Z”, “J”, “U”, “O”.

Supplementary Text

S1. Equilibrium measurements to test if activity depends on [urea], [Zn²⁺], and pH

Altered catalytic efficiencies for a given mutant could simply reflect changes in the equilibrium population of active enzyme under our assay conditions. We identified three molecular mechanisms that could alter the fraction of active enzyme at equilibrium: (1) thermodynamic destabilization that shifts the equilibrium distribution of folded and unfolded PafA, (2) diminished affinity for Zn²⁺ at the bimetallo site, and (3) alteration in the observed inhibitory enzymatic pK_a. We systematically tested each of these three possibilities on-chip for our valine and glycine scanning mutant libraries as described below.

Equilibrium unfolding of PafA upon mutation in the presence of urea

For a two-state equilibrium between folded and unfolded states given by



the dependence of the Gibbs free energy of unfolding on denaturant concentration is given by

$$\Delta G = \Delta G^{\text{H}_2\text{O}} - m[\text{urea}] \quad (21)$$

where m describes the dependence of ΔG on the concentration of denaturant. Using the lower bound, and therefore most conservative, m -value for urea denaturation for wild-type PafA predicted using the Protein m -value Calculation Webserver (108), ($m_{\text{pred}} = 4.8$ kcal/mol/M), we can predict the unfolding of PafA as a function of [urea] by recasting **Eq. 21** as follows and solving for the folded fraction, f_f :

$$-RT \ln \frac{1 - f_f([\text{urea}])}{f_f([\text{urea}])} = -RT \ln \frac{1 - f_f(0\text{M})}{f_f(0\text{M})} - m[\text{urea}] \quad (22)$$

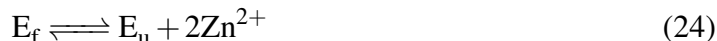
$$f_f([\text{urea}]) = \frac{1}{1 + e^{\frac{m[\text{urea}]}{RT} \left(-1 + \frac{1}{f_f(0\text{M})}\right)}} \quad (23)$$

where T is the temperature and R is the ideal gas constant. In order for an observed significant decrease in activity (*i.e.*, a >2 -fold decrease in k_{cat}/K_M) upon mutation to result purely from unfolding, the unfolded fraction (denoted here as $f_u = 1 - f_f$) would have to be >0.5 . Under these conditions, **Eq. 23** predicts that the relative populations within the folded and unfolded fractions (and thus the observed activity) would be highly sensitive to the addition of denaturant (Main Text **Fig. 2H**). For example, if 50% of enzyme were unfolded due to thermodynamic destabilization under our standard assay conditions, **Eq. 23** predicts that observed rates at 1 and 2 M would drop by $>10^3$ and $>10^7$ -fold, respectively. Although these predicted changes are based on a computed m -value, even if this were underestimated by 2-fold, we would still expect a >10 and $>10^3$ -fold change at 1 and 2 M urea, respectively. In contrast to these predictions, we observe effects of <4 -fold and <10 -fold for 99% of mutants, and <2 -fold and <3 -fold for 95% of mutants, at 1 and

2 M urea, respectively. These small effects are consistent with an apparent competitive inhibition of folded active PafA by urea (**Fig. S26**). Overall, this discrepancy between predicted and observed behaviors establishes that mutational effects on k_{cat}/K_M cannot be due to equilibrium destabilization.

Altered affinity of Zn^{2+} for the bimetallo site upon mutation

PafA binds two essential catalytic Zn^{2+} ions in the folded state (16) and upon unfolding, these Zn^{2+} ions should be released to solution. Therefore, a necessary corollary to the model of equilibrium unfolding is that excess $[\text{Zn}^{2+}]$ will push the following equilibrium towards the folded state:



where the equilibrium constant, K_u , is defined by

$$K_u = \frac{[E_u][\text{Zn}^{2+}]^2}{[E_f]} \quad (25)$$

or equivalently, in terms of the folded fraction of enzyme, f_f ,

$$K_u = \frac{(1 - f_f)[\text{Zn}^{2+}]^2}{f_f} \quad (26)$$

If observed mutational effects on activity were due to equilibrium unfolding, decreasing the solution $[\text{Zn}^{2+}]$ would significantly reduce f_f . Rearranging **Eq. 26** yields the relationship between f_f and $[\text{Zn}^{2+}]$:

$$f_f = \frac{[\text{Zn}^{2+}]^2}{K_u + [\text{Zn}^{2+}]^2} \quad (27)$$

To test this model, we measured rates of hydrolysis for PafA valine scan mutants over a range of $[\text{Zn}^{2+}]$ and compared these measured rates to those what would be predicted by **Eq. 27**. Consistent with the absence of significant equilibrium unfolding, we observed no significant decreases in activity over a 100-fold range of $[\text{Zn}^{2+}]$. As fractional occupancies have not been measured for the two distal Zn^{2+} ions seen in the WT PafA crystal structure, we do not include them in this calculation. However, their inclusion would predict even more dramatic effects.

Altered enzymatic $\text{p}K_a$ upon mutation

PafA possesses an inhibitory enzymatic $\text{p}K_a$ of ~ 8.0 (16, 109). This may be due to deprotonation of a bimetallo zinc-coordinated water, generating an inhibitory hydroxide ion bound at the active site (19, 35). We therefore tested the possibility that mutants with observed decreases in k_{cat}/K_M relative to WT possess shifted enzymatic $\text{p}K_a$ s (apparently competitive; **Eq. 28**).



This two-state model predicts that a change in assay pH (a change from pH A to pH B) will change the observed $k_{\text{cat}}/K_{\text{M}}$ (**Eq. 29**).

$$\frac{(k_{\text{cat}}/K_{\text{M}})^{\text{pHA}}}{(k_{\text{cat}}/K_{\text{M}})^{\text{pHB}}} = \frac{1 + 10^{\text{pHB} - \text{p}K_{\text{a}}}}{1 + 10^{\text{pHA} - \text{p}K_{\text{a}}}} \quad (29)$$

Comparisons between experimentally measured $k_{\text{cat}}/K_{\text{M}}$ values and those predicted by the previously observed $\text{p}K_{\text{a}}$ (**Eq. 29**) for WT and active site mutant PafA constructs at pH 8.0 (standard conditions), 7.5, and 7.0 revealed that, in contrast with the expected 1.5-fold and 1.8-fold increases in $k_{\text{cat}}/K_{\text{M}}$ upon reducing pH to 7.5 and 7.0, the WT enzyme either lost or only slightly gained in activity. These observations are consistent with time-dependent enzyme death that may be aggravated upon acidification. Overall, 97% of glycine and valine library mutants had pH-dependent changes in activity within the range observed for WT PafA enzymes across four pH values. These results strongly suggest that enzymatic $\text{p}K_{\text{a}}$ values for mutants do not significantly differ from the WT values and cannot explain observed mutational effects.

S2. Deriving the predicted relationship between $k_{\text{cat}}/K_{\text{M}}$ for cMUP and MeP for PafA

At subsaturating concentrations, WT PafA hydrolysis of cMUP is limited by the rate of binding to the enzyme (k_1 ; Main Text **Fig. 7A**) (13, 19). By contrast, hydrolysis of MeP at subsaturating concentrations is limited by the chemical step ($k_{\text{chem},1}$; Main Text **Fig. 7A**). The relative intrinsic reactivities of these substrates is proportional to the ratio of their hydrolysis rates on the enzyme (the rate of the chemical step, enzyme-substrate complex hydrolysis, for each) (13):

$$f_{\text{r}} = k_{\text{chem},1}^{\text{cMUP}}/k_{\text{chem},1}^{\text{MeP}} \quad (30)$$

Using f_{r} (**Eq. 30**) and the substrate-independent binding rate k_1 , we can then derive a mathematical relationship between $k_{\text{cat}}/K_{\text{M}}$ values for cMUP and MeP (**Eq. 31**, below). We can use **Eq. 31** and previously-determined cMUP and MeP $k_{\text{cat}}/K_{\text{M}}$ values for PafA active site mutants, which are not significantly misfolded (**Fig. S41**), to solve for f_{r} . This value (f_{r}), the experimentally-estimated value of $k_1 = 1.42 \times 10^6 \text{ M}^{-1}\text{s}^{-1}$ (see below), and **Eq. 31** predict the kinetic behavior of our PafA Val and Gly mutants in the absence of any misfolding effects.

$$(k_{\text{cat}}/K_{\text{M}})^{\text{cMUP}} = \frac{f_{\text{r}}k_1(k_{\text{cat}}/K_{\text{M}})^{\text{MeP}}}{k_1 + (f_{\text{r}} - 1)(k_{\text{cat}}/K_{\text{M}})^{\text{MeP}}} \quad (31)$$

Specifically, the value of f_{r} was fit using the NMinimize function of Mathematica with \log_{10} -scaled on-chip cMUP and MeP hydrolysis rates for wild-type and the five PafA active site mutants. MeP measurements were made with the Phosphate Sensor (PBP) under reaction conditions used on chip. While MeP $k_{\text{cat}}/K_{\text{M}}$ for K162A was too slow to accurately measure off chip using the PBP, a point estimate was made by scaling the previously published pNPP K162A rate constant by 6-fold to account for the previously observed ionic strength dependency of $k_{\text{cat}}/K_{\text{M}}$ (16, 110). To generate a fit f_{r} consistent with on-chip data,

the cMUP and MeP estimates were scaled by the ratio of $(k_{\text{cat}}/K_{\text{M}}^{\text{on-chip}})/(k_{\text{cat}}/K_{\text{M}}^{\text{off-chip}})$ for WT PafA (0.47). For fitting, k_1 was restrained at $1.42 \times 10^6 \text{ M}^{-1}\text{s}^{-1}$, the median on-chip WT $k_{\text{cat}}/K_{\text{M}}$ for cMUP. The best-fit value of f_r was 776 ± 126 (Median \pm SEM), with standard error of the mean calculated from a Monte Carlo simulated distribution of f_r assuming normally-distributed error on the underlying measurements.

S3. A two-state model of unfolding estimates mutational misfolding effects on f_a

Assays measuring effects of altering expression temperature and zinc concentration strongly suggest that many mutations promote the formation of non-exchanging misfolded and inactive enzymes. Evidence for lack of exchange between the active and inactive states comes from on-chip experiments varying expression temperature and expression Zn^{2+} concentration, and the lack of activity loss when the misfolded state is completely degraded by thermolysin (**Figs. 3 and S38**). To deconvolve and quantify mutational effects on misfolding and catalysis, we used a two-state model to quantitatively estimate the fraction of mutant enzymes in these misfolded, inactive states. We note that although this is a two-state model, this misfolded fraction could potentially reflect a combination of multiple misfolded states that are all catalytically-inactive rather than a single misfolded state. The active site mutants are well-fit by expected relative reactivities, and we confirmed that each active site single mutant is fully folded (**Fig. S41**). Thus, observed losses in activity for these mutants reflect purely catalytic effects ($f_a = 1$) (**Figs. S42 and S43**).

This assumption, together with the fit relative reactivity of cMUP and MeP substrates (f_r , see **Supplementary Text S3**), makes it possible to solve for the active enzyme fraction as a function of observed cMUP and MeP $k_{\text{cat}}/K_{\text{M}}$ values (**Eq. 32**):

$$f_a = \frac{(f_r - 1)(k_{\text{cat}}/K_{\text{M}})^{\text{MeP,obs}}(k_{\text{cat}}/K_{\text{M}})^{\text{cMUP,obs}}}{k_1(f_r(k_{\text{cat}}/K_{\text{M}})^{\text{MeP,obs}} - (k_{\text{cat}}/K_{\text{M}})^{\text{cMUP,obs}})} \quad (32)$$

We used this relationship to estimate f_a , $k_{\text{cat}}/K_{\text{M,chem}}$, and associated confidence intervals for mutants in our valine and glycine libraries; we also estimated bootstrapped statistics and p -values as described in **Materials and Methods**. In two cases, we could not calculate f_a : (1) mutants with $k_{\text{cat}}/K_{\text{M}}^{\text{MeP,obs}} > k_{\text{cat}}/K_{\text{M}}^{\text{cMUP,obs}}$, and (2) mutants with limits for both $k_{\text{cat}}/K_{\text{M}}^{\text{MeP,obs}}$ and $k_{\text{cat}}/K_{\text{M}}^{\text{cMUP,obs}}$ in the same direction. These mutants were therefore excluded from downstream analysis to estimate mutational effects on intrinsic catalytic parameters.

S4. Estimating mutational effects on intrinsic catalytic parameters

Estimating the intrinsic k_{cat} and $k_{\text{cat}}/K_{\text{M}}$ requires dividing the total observed enzyme concentration by the fraction active (f_a), as follows:

$$(k_{\text{cat}})^{\text{cMUP,chem}} = (k_{\text{cat}})^{\text{cMUP,obs}}/f_a \quad (33)$$

$$(k_{\text{cat}}/K_{\text{M}})^{\text{cMUP,chem}} = (k_{\text{cat}}/K_{\text{M}})^{\text{cMUP,obs}}/f_a \quad (34)$$

$$(k_{\text{cat}}/K_{\text{M}})^{\text{MeP,chem}} = (k_{\text{cat}}/K_{\text{M}})^{\text{MeP,obs}} / f_{\text{a}} \quad (35)$$

We note that K_{M} is the substrate concentration that gives half-maximal activity and is independent of f_{a} , provided that the active and inactive populations do not exchange (which is the case in our experiments).

In each case, we again estimated bootstrapped statistics and p -values as described in **Materials and Methods**. In addition, we define the intrinsic ‘‘Catalytic effect’’ of mutation, using **Eq. 35**, as follows:

$$\text{Catalytic effect} = \frac{(k_{\text{cat}}/K_{\text{M}})_{\text{mutant}}^{\text{MeP,chem}}}{(k_{\text{cat}}/K_{\text{M}})_{\text{WT}}^{\text{MeP,chem}}} \quad (36)$$

S5. Identifying and classifying non-conserved auxiliary domains

Alkaline phosphatase (AP) superfamily members contain a universally-conserved Rossmann fold domain, the hydrophobic core of the enzyme, which bears the conserved bimetallo Zn^{2+} ligands and a nucleophilic serine or threonine. AP superfamily members also contain up to 6 ‘‘auxiliary’’ domains (ADs) of varying length, secondary structure, and tertiary structure that are inserted at spatially-conserved junctures in the core of the Rossmann fold (**Figs. S12** and **S53**). Although the presence or absence and approximate length of particular ADs is conserved among superfamily members sharing cognate reactivities, AP phosphomonoesterases still display variability in the structure and precise length of these insertions. However, the six bimetallo Zn^{2+} -site ligands are conserved across all known mono- and diesterases.

To define and enumerate ADs for all AP superfamily phosphomonoesterases and phosphodiesterases for which crystal structures are available (**Table S12** and **Fig. S52**), we first aligned the six bimetallo Zn^{2+} -site ligands within each structure (selecting one chain to perform alignment) to those of PafA using the ‘‘align’’ command of PyMOL 2. Next, we identified the conserved Rossmann core within each member, defined as the regions present with shared secondary structure and well-aligned backbones (as assessed qualitatively from the alignment) in all enzymes within the structural alignment. Finally, we defined ADs to comprise any stretches of 1° sequence present in individual superfamily members but not structurally shared among all of them. This procedure identified 3–6 ADs for each enzyme, indexed based on their point of insertion in the Rossmann core (using PafA numbering). ADs 2–4 are present in both phosphomonoesterases and phosphodiesterases.

AD3 is composed of two smaller domains (ADs 3.1 and 3.2) separated by only 7 or 8 residues in the Rossmann core. In monoesterases, AD 3.1 contains the K162 and R164 active site residues essential for phosphomonoesterase specificity and AD 3.2 is significantly larger, suggesting an evolutionary association between ADs 3.1 and 3.2.

S6. Estimating mutational effects on phospho-enzyme intermediate hydrolysis

For the three-metal AP superfamily phosphomonoesterase EcAP, phosphate release ($k_{\text{off,Pi}}$) is the k_{cat} rate-limiting step at pH 8.0; at lower pH, hydrolysis of the covalent phospho-enzyme intermediate ($k_{\text{chem},2}$) becomes rate limiting (58). Independent evidence suggests that EcAP mutations alter $k_{\text{off,Pi}}$ and $k_{\text{chem},2}$ (111). As the WT PafA catalytic cycle is highly similar to that of EcAP, PafA k_{cat} is likely rate-limited by one or both of these catalytic steps, and mutations may alter these rates. To quantify $k_{\text{chem},2}$ for WT PafA and all mutants, we first estimated the rate of phosphate release, $k_{\text{off,Pi}}$ (**Eq. 37**):

$$k_{\text{off,Pi}} = K_i(\text{P}_i) \times k_{\text{on,Pi}} \quad (37)$$

Here, we use the measured K_i for P_i from on-chip HT-MEK experiments and assume that $k_{\text{on,Pi}}$ is approximately the apparent rate constant for substrate binding to the enzyme. As the k_{cat}/K_M for activated aryl substrates (*e.g.* cMUP) is binding-limited (19) and we expect that $k_{\text{on,Pi}}$ will not vary substantially upon mutation (111), we can estimate $k_{\text{on,Pi}}$ using the WT PafA k_{cat}/K_M for cMUP ($k_{\text{on,Pi}} \approx k_{\text{cat}}/K_M^{\text{cMUP,WT}} = 1.42 \times 10^6 \text{ M}^{-1}\text{s}^{-1}$).

Next, we estimated the rate of covalent phospho-enzyme intermediate hydrolysis ($k_{\text{chem},2}$) for all mutants with an estimated $k_{\text{off,Pi}}$ and measured $k_{\text{cat}}^{\text{cMUP,chem}}$ (the f_a -corrected k_{cat} , **Eq. 33**) for cMUP (992/1036). To do this, we first derived an expression for the PafA k_{cat} using the method of net rate constants (112), assuming that $k_{\text{chem},2} \gg k_{\text{chem},-2}$ (**Eq. 38**). This assumption is supported by the observations that $k_{\text{chem},2}/k_{\text{chem},-2} = 100$ and 40 for WT EcAP and R166S EcAP, respectively (111).

$$k_{\text{cat}}^{\text{cMUP,chem}} = \frac{1}{\frac{1}{k_{\text{off,Pi}}} + \frac{1}{k_{\text{chem},2}} + \frac{1}{k_{\text{chem},1}} + \frac{1}{k_1 \frac{k_{\text{chem},1}}{k_{-1} + k_{\text{chem},1}}}} \approx \frac{1}{\frac{1}{k_{\text{off,Pi}}} + \frac{1}{k_{\text{chem},2}}} = \frac{k_{\text{off,Pi}} k_{\text{chem},2}}{k_{\text{off,Pi}} + k_{\text{chem},2}} \quad (38)$$

Next, we substituted the expression for $k_{\text{off,Pi}}$ from **Eq. 37**:

$$k_{\text{cat}}^{\text{cMUP,chem}} = \frac{k_{\text{on,Pi}} K_i(\text{P}_i) k_{\text{chem},2}}{k_{\text{on,Pi}} K_i(\text{P}_i) + k_{\text{chem},2}} \quad (39)$$

Finally, solving for $k_{\text{chem},2}$ and substituting with **Eq. 33**

$$k_{\text{chem},2} = \frac{k_{\text{on,Pi}} K_i(\text{P}_i) k_{\text{cat}}^{\text{cMUP,chem}}}{k_{\text{on,Pi}} K_i(\text{P}_i) - k_{\text{cat}}^{\text{cMUP,chem}}} = \frac{k_{\text{on,Pi}} K_i(\text{P}_i) k_{\text{cat}}^{\text{cMUP,obs}}}{f_a k_{\text{on,Pi}} K_i(\text{P}_i) - k_{\text{cat}}^{\text{cMUP,obs}}} \quad (40)$$

Using this expression, we estimated $k_{\text{chem},2}$ for all mutants with measurements for $K_i(\text{P}_i)$ and $k_{\text{cat}}^{\text{cMUP,chem}}$. Limits in $K_i(\text{P}_i)$ and/or f_a yield limits in $k_{\text{chem},2}$, and these limit cases were i) $k_{\text{chem},2}$ upper limit, arising from a lower f_a limit and a lower, or no, limit in $K_i(\text{P}_i)$; ii) $k_{\text{chem},2}$ lower limit, arising from an upper limit in $K_i(\text{P}_i)$ and an upper, or no limit, in f_a ; iii) undefined $k_{\text{chem},2}$ limit, arising from a lower limit in $K_i(\text{P}_i)$ and an upper limit in f_a , or an upper limit in $K_i(\text{P}_i)$ and a lower limit in f_a (these estimates were omitted from plots and downstream analyses). Finally, a lower limit in $K_i(\text{P}_i)$ yields a range of potential

values of $k_{\text{chem},2}$ (case iv.), but we treated this limit case as a point estimate (*i.e.*, no limit) for plots and analyses as the bounded range is small for most mutants.

Estimates of mutational effects on $k_{\text{chem},2}$ rely on measurements of the K_i for P_i and $k_{\text{cat}}^{\text{cMUP,chem}}$, and the latter relies on accurate estimation of mutational effects on the active enzyme fraction (f_a). Measurement error in any of these quantities renders estimates of mutational effects on $k_{\text{chem},2}$ less precise. To account for this uncertainty, we calculated p -values for mutant $k_{\text{chem},2}$ estimates via bootstrap hypothesis testing in an analogous manner as for $k_{\text{cat}}/K_M^{\text{chem}}$ and f_a effects (see **Materials and Methods**, *Determining statistical significance of fraction active and catalytic effects within the active fraction*).

S7. Evolutionary constraints revealed by comparisons between phylogeny and functional parameters

Natural evolution provides a mutagenesis and selection experiment at a massive scale. Highly conserved residues typically perform critical functions (e.g. active site residues) and coevolution between residues can reveal molecular contacts required for folding and stability (113–115). Nevertheless, conservation cannot reveal all aspects of function, most basically because selective pressures may exist for multiple aspects of function. HT-MEK and FCA have allowed us to dissect and quantify effects of mutations at every residue on misfolding, catalysis, and four Functional Components. Here, we assess the correlation between conservation and these functional effects using a metagenomic alignment of 14,505 AP superfamily sequences with PafA-like active site residues (T79, K162, and R164; fig. S67).

Fig. S68A shows conservation at each position throughout the PafA structure and provides the starting point for these comparisons. Residues with high conservation scores often have no apparent functional effect, and some with lower scores have effects (figs. S69 and S70). Overall, observed k_{cat}/K_M values (MeP hydrolysis) correlated with the information content at a given position (Spearman $\rho = 0.4$; figs. S68B and S69A), with this correlation increasing slightly for more perturbative substitutions (fig. S69B). Systematic comparisons of information content and the mutational effects on misfolding, catalysis ($k_{\text{cat}}/K_M^{\text{chem}}$) and each of the four Functional Components gave Spearman's correlation coefficients with magnitudes ranging from 0.1 to 0.25 (figs. S68B and S69). The observation of multiple correlations with these functional parameters underscores the complexity of evolutionary pressure and responses and the need for additional information to understand and interpret the sequence record.

Figures S1 to S70

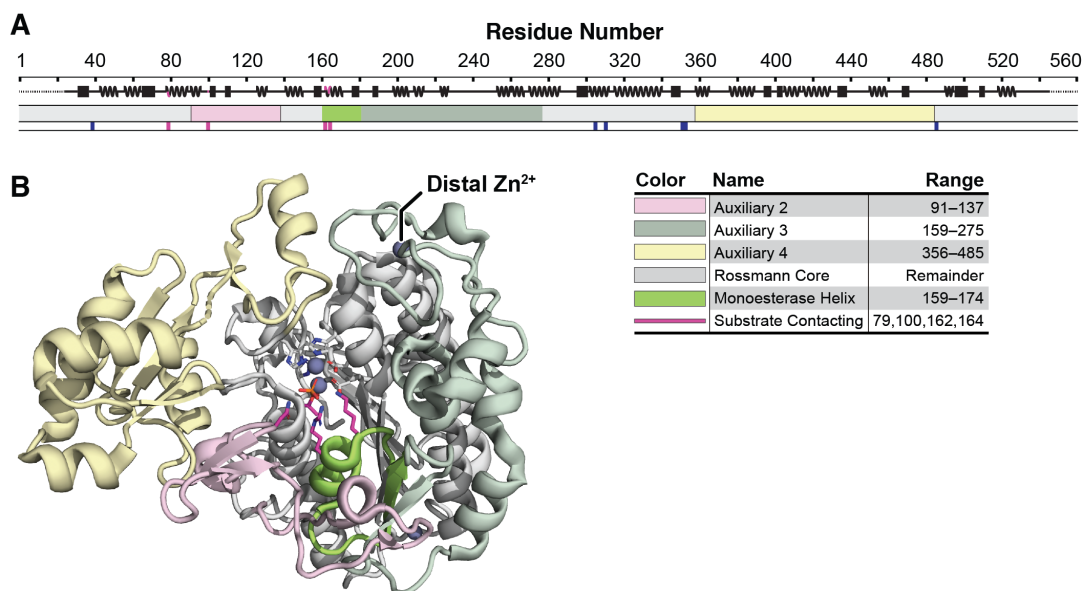


Fig. S1. Structural overview of PafA phosphatase. (A) Linear topology of PafA showing secondary structure, named domains and structural elements (colored as in the legend below and to the right), and key catalytic residues, including active site residues (magenta) and Zn^{2+} ligands (dark blue). (B) Crystal structure of WT PafA (PDB ID: 5TJ3) with conserved superfamily core fold (Rossmann fold) in white and insertion (“Auxiliary”) domains colored as in panel A. Besides the two active site Zn^{2+} ions, one of two additional Zn^{2+} ions is annotated (“Distal Zn^{2+} ”).

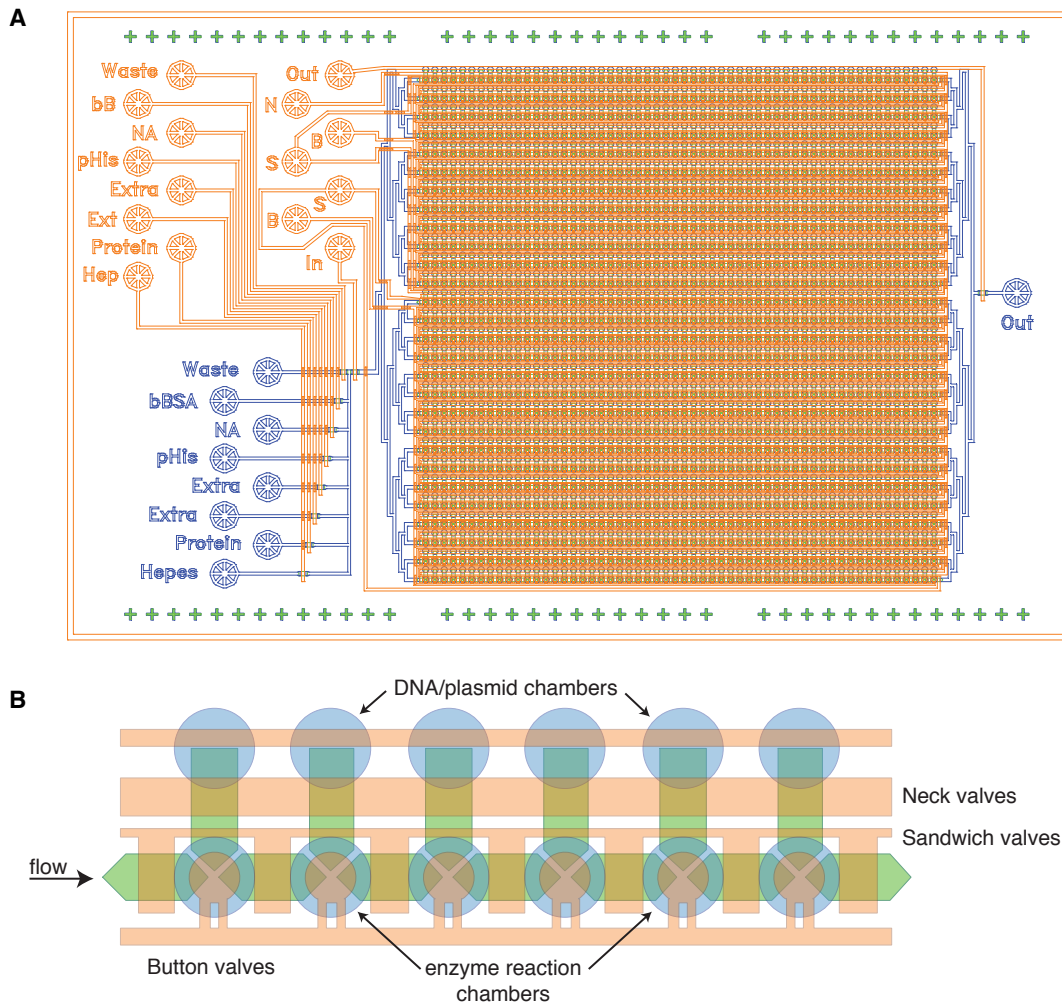


Fig. S2. Detailed schematic of the microfluidic device used for HT-MEK measurements. (A) PDMS device “control” (orange) and “flow” (blue) layers, with input ports labeled (70, 71). Each device contains 1,568 chambers (56 chambers arrayed along each of 28 fluidically-connected channels). (B) Detailed schematic for six example reaction chambers along a single channel. Each chamber contains two compartments, “DNA/plasmid” (DNA) and “enzyme reaction” (Reaction), with fluid flow within and between chambers controlled by three valves: a Sandwich valve (to control fluid flow between chambers), a Neck valve (to control fluid flow between compartments), and a Button valve that restricts fluidic access to a particular patch of the device surface for surface patterning, enzyme immobilization, and fluid exchange.

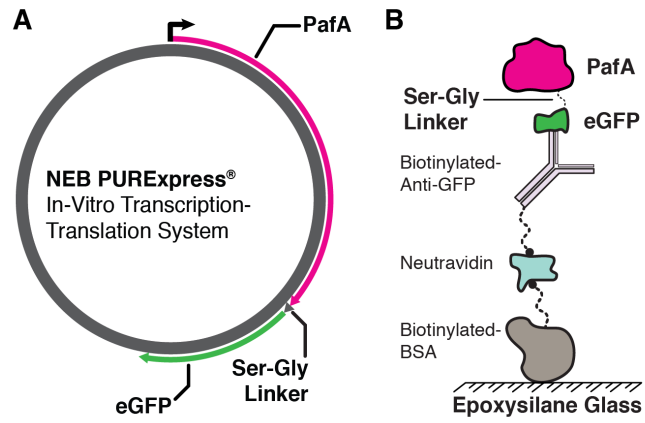


Fig. S3. Protein expression constructs and linkages for surface immobilization. (A) Vector map of the PafA-eGFP PURExpress construct with flexible Ser-Gly linker. (B) Molecular linkages tethering expressed PafA-eGFP constructs to epoxysilane glass surfaces within the HT-MEK device.

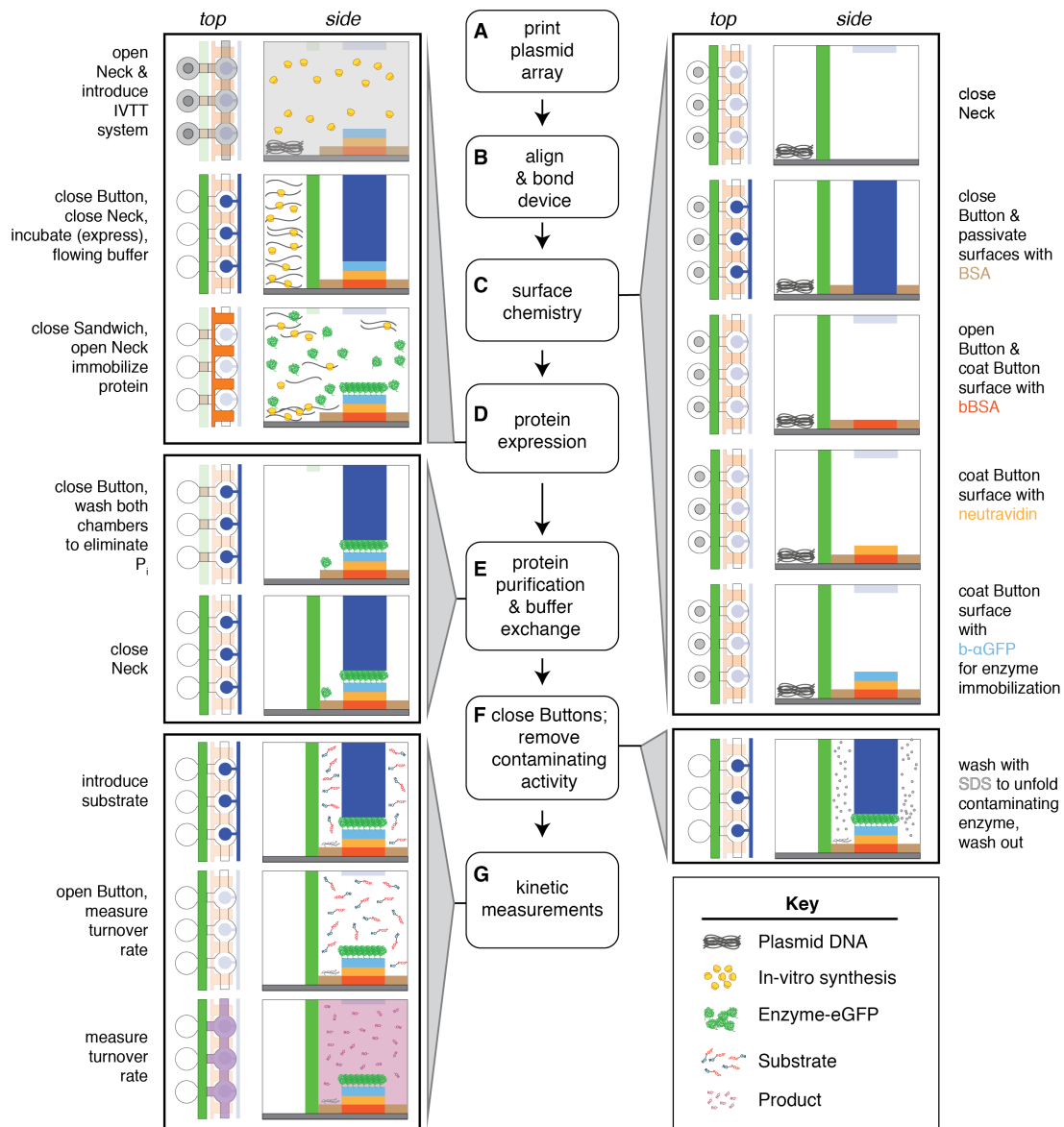


Fig. S4. Schematic showing workflow for on-chip surface patterning, enzyme expression and purification, and subsequent kinetic assays via HT-MEK.

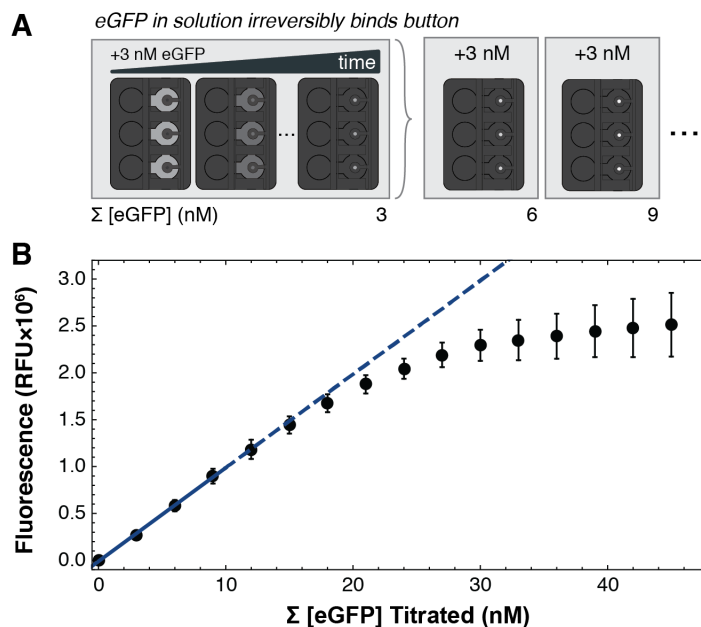


Fig. S5. Calibration curves relating surface-immobilized eGFP intensities to effective enzyme concentrations in each chamber. (A) Schematic of calibration curve acquisition showing iterative introduction of 3 nM eGFP into each reaction chamber, opening of the Button valves to expose anti-eGFP patterned device surfaces, and binding of eGFP until saturation. Each titration repeated this process at least 12 times (to a total summed concentration of at least 36 nM). (B) Measured eGFP intensities beneath the Button valve after 15 iterative introductions of 3 nM eGFP. Points denote the median fluorescence in all chambers across the device; error bars indicate the standard error on the mean (SEM). A linear fit (blue) to measured fluorescence intensity as a function of [eGFP] for the first 4–9 points yielded fit parameters that were subsequently used to convert measured intensities within each chamber to product concentrations during kinetic assays (slope = $\sim 100,000$ – $200,000$ RFU/nM).

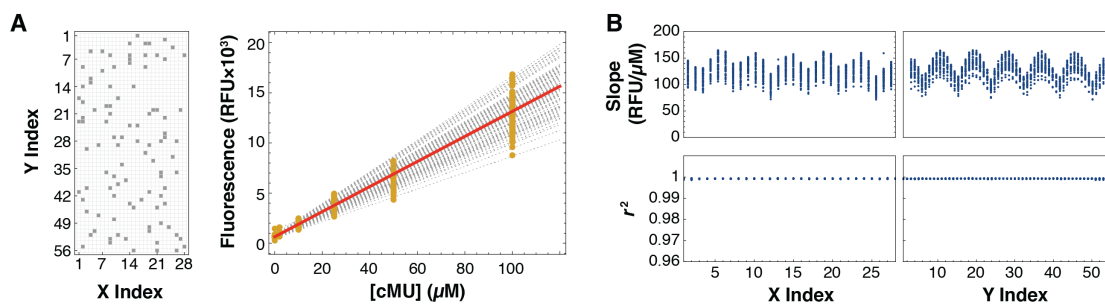


Fig. S6. Per-chamber on-chip product calibration curves for an example fluorescent product (cMU, see **Materials and Methods**). (A) Measured fluorescence intensities as a function of introduced cMU concentration (right) for 100 chambers at various positions within the device (left). Median intensities for each chamber are shown in gold, calibration curves for each chamber are shown as black dashed lines, and a linear fit to the median of all chamber intensities at a given concentration is shown in red. (B) Observed variation in slope as a function of chamber position within the device (top) and returned coefficients of determination for linear fits (bottom). The observed regular variation in slope, as a function of device position, is expected as a result of image vignetting.

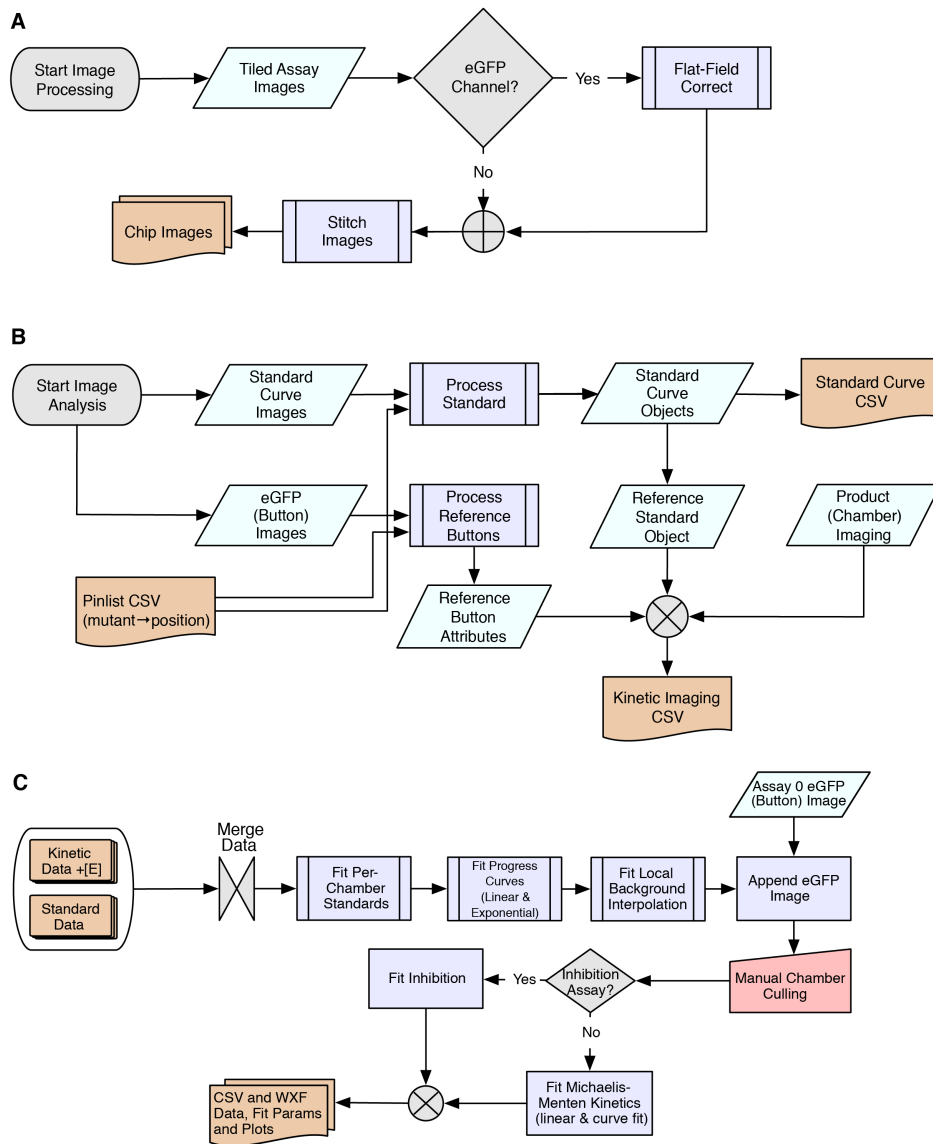


Fig. S7. Image processing and Michealis-Menten fitting pipelines as well as all data available in the OSF repository (<https://doi.org/10.17605/OSF.IO/QRN3C>). (A) Image processing workflow. Overlapping tiled chip images (1024×1024 , 16-bit depth) are flat-field corrected if collected in the eGFP channel, then stitched to generate single images of the entire device at each assay time point. (B) Image post-processing pipeline. Product standard curve images, eGFP Button images, and enzymatic turnover chamber images are combined, associated with chamber variant identities (Pinlist), and processed to yield a data table describing kinetic progress curves for each chamber. (C) Pipeline for processing kinetic data and applying quality control criteria to yield Michaelis-Menten parameters and inhibition constants.

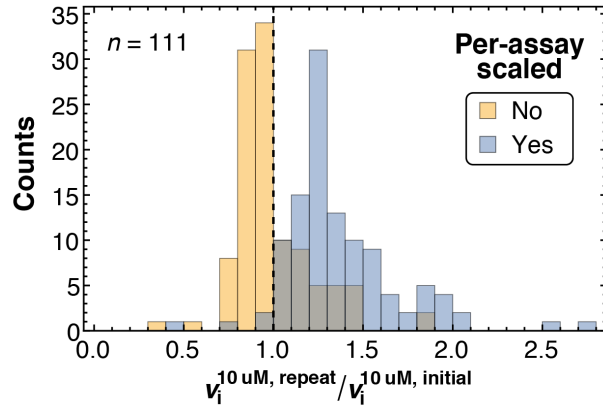


Fig. S8. Scaling each rate by the enzyme concentration ([E]) determined before each assay results in systematic overestimation of later rates. Comparison of the ratios of initial rates in each chamber obtained for an initial 10 μM cMUP assay and a replicate assay acquired ~ 6 hours later, scaling rates measured in both assays by the first eGFP measurement only (yellow), and those obtained after scaling by the [E] determined before each assay (blue).

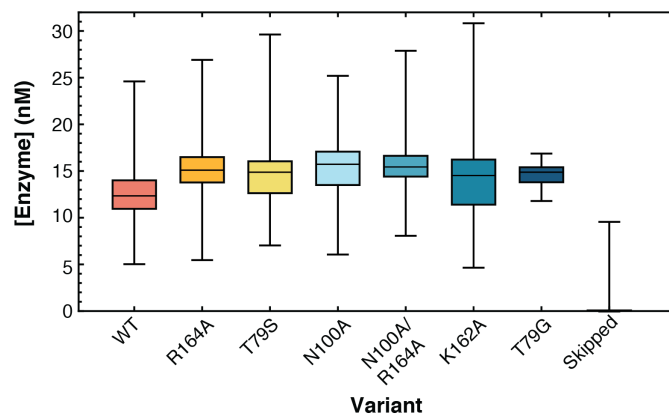


Fig. S9. On-chip expression of PafA active site mutants. Distribution of calibrated per-chamber enzyme concentrations for seven PafA-eGFP variants and chambers in which no plasmid was printed (Skipped). Whiskers denote the full range of enzyme concentrations calculated from individual chamber eGFP intensities; boxes define the range between the 25% and 75% quantiles. Apparent expression in several Skipped chambers is inflated by enzyme leakage from adjacent DNA-containing chambers; in kinetic experiments, these chambers would be identified and eliminated from further analysis (*cf.* **Materials and Methods**, *Analysis and quality control of cMUP hydrolysis measurements*).

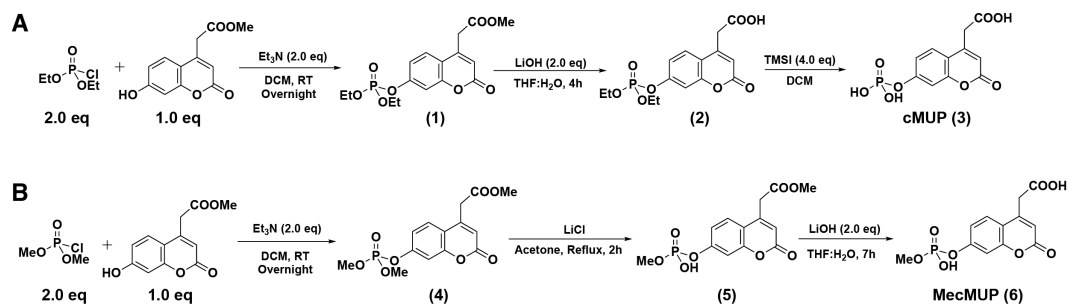


Fig. S10. Synthesis of carboxy-coumarinyl phosphomonoester and phosphodiester substrates. (A) Synthesis of cMUP. (B) Synthesis of MecMUP.

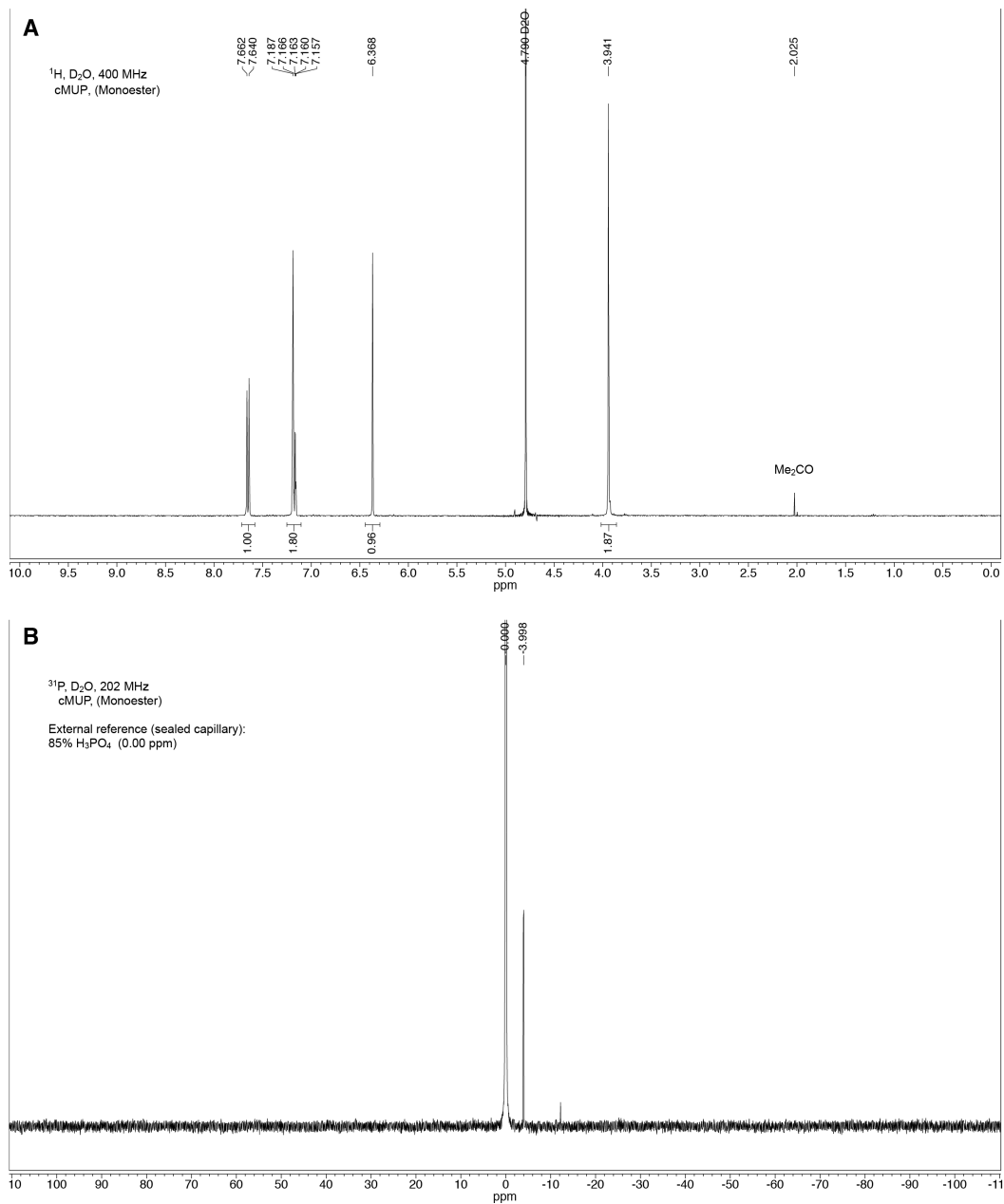


Fig. S11. ¹H (A) and ³¹P (B) NMR spectra of 2-(2-oxo-7-(phosphonoxy)-2H-chromen-4-yl)acetic acid (cMUP; **Fig. S10A** compound **3**).

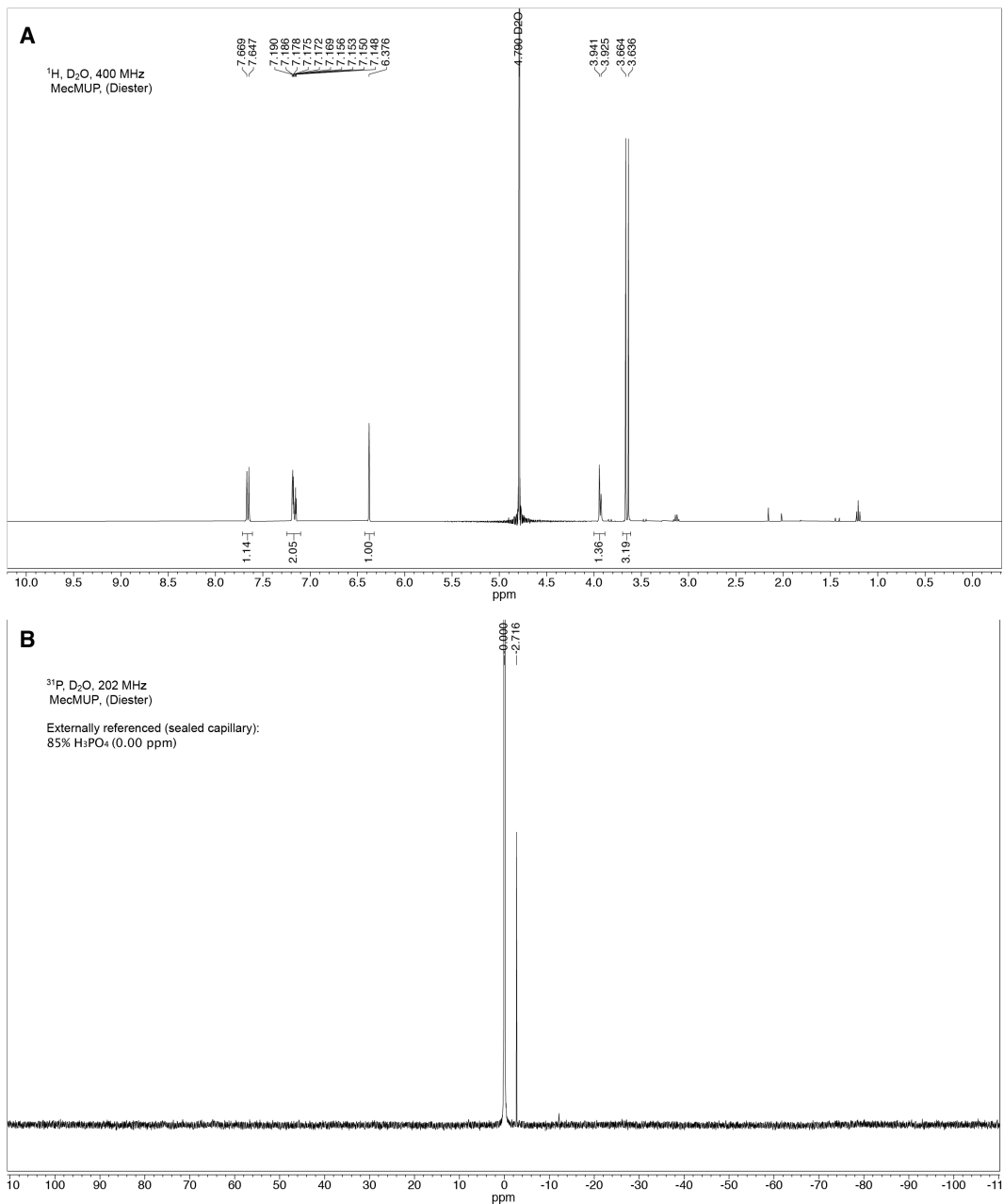


Fig. S12. ¹H (A) and ³¹P (B) NMR spectra of 2-(7-((hydroxy(methoxy)phosphoryl)oxy)-2-oxo-2H-chromen-4-yl)acetic acid (MecMUP; **Fig. S10B** compound **6**).

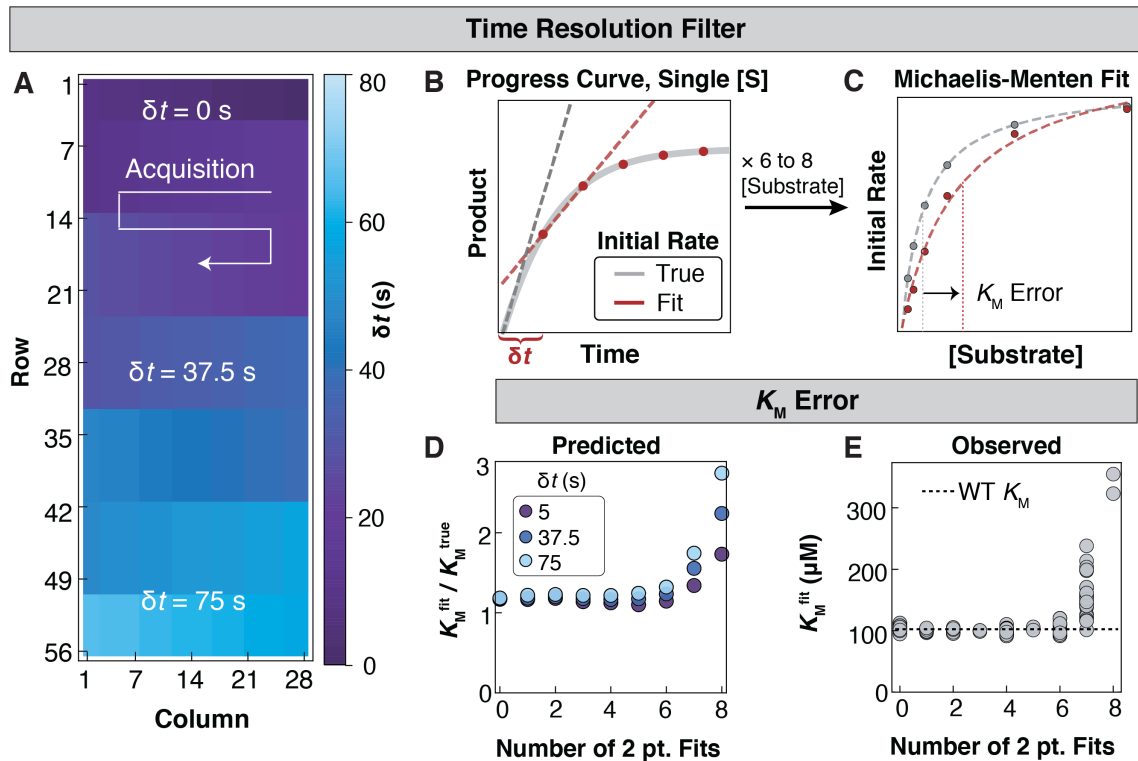


Fig. S13. Eliminating chambers with rates too fast to be measured accurately. (A) Heat map showing initial image acquisition delay time as a function of device position. (B) Simulated progress curves for a WT enzyme illustrating how a linear fit (red dashed line) to measurements sampled with a long initial delay (red circles) can underestimate the true rate (gray dashed line). (C) Simulated Michaelis-Menten curves illustrating how Michaelis-Menten fits to initial rates estimated from measurements with a long initial delay (red points) can lead to systematic overestimates of K_M (red curve; “true” values and associated fit shown in gray). (D) K_M values obtained from Michaelis-Menten fits of simulated progress curves assuming WT parameters ($k_{\text{cat}} = 200 \text{ s}^{-1}$, $K_M = 100 \mu\text{M}$ and $[E] = 10 \text{ nM}$), for three different values of δt . Underestimation ($K_M^{\text{fit}}/K_M^{\text{true}}$) increases with increasing δt or the number of initial rates with two-point fits used to generate the Michaelis-Menten curve. (E) Fit K_M values for WT chambers as a function of the number of two-point initial rate fits in the Michaelis-Menten curve. Observed systematic errors match those predicted from the simulations in panel D.

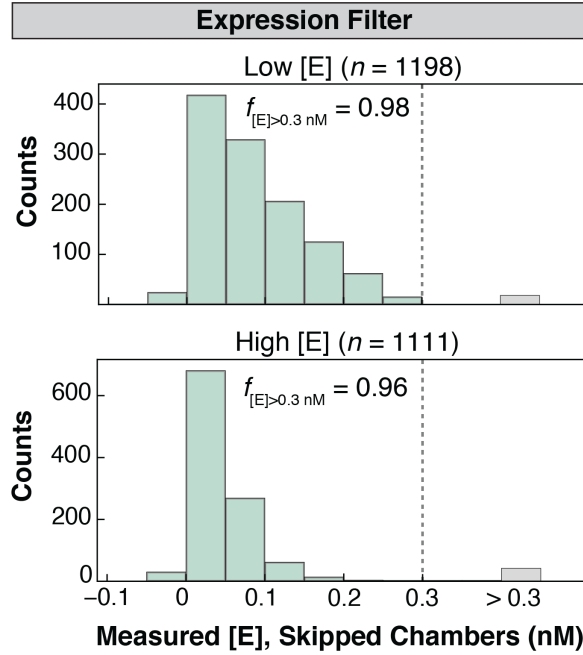


Fig. S14. Eliminating chambers with poor enzyme expression from further analysis. Distribution of measured eGFP intensities in “Skipped” chambers (in which no plasmid was printed) for low [E] (top) and high [E] (bottom) devices. For both sets of experiments, $>95\%$ of “Skipped” chambers had measured $[E] \leq 0.3 \text{ nM}$ (grey dashed line). We therefore flagged any chambers with $\leq 0.3 \text{ nM}$ immobilized enzyme as lacking successful expression.

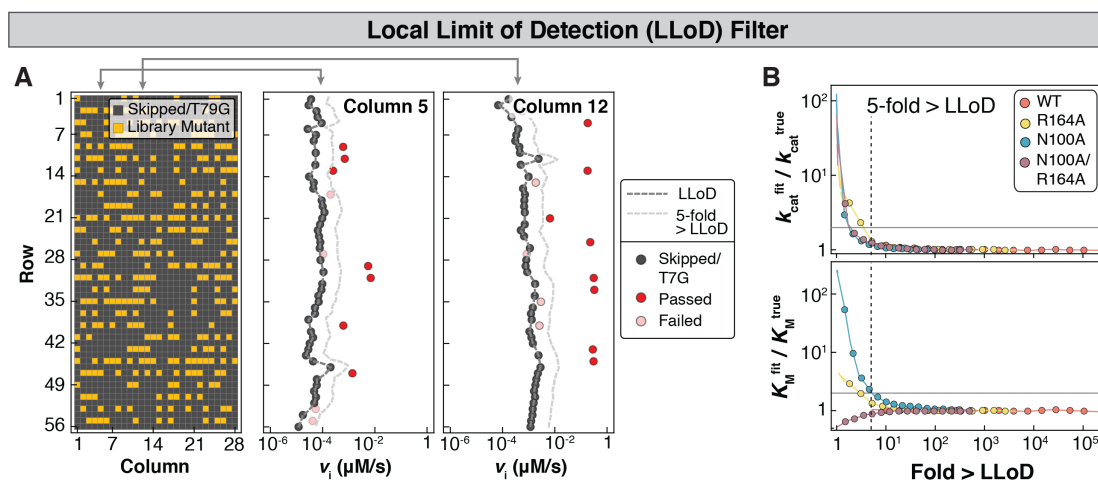


Fig. S15. Quality control to eliminate chambers with artificially high observed rates resulting from WT-like contamination. (A) Heat map (left) of a representative tier I device showing the location of library mutants (gold), and Skipped and T79G chambers (gray); observed rates as a function of row position for two example columns (channels) for Skipped/T79G chambers (gray) and mutant chambers that either passed (red) or failed (pink) the quality control criteria (observed rate >5 -fold above the interpolated local limit of detection (LLoD, light gray dashed line)). (B) Simulations used to determine a threshold of $5\times$ LLoD. Fractional errors in k_{cat} (top) and K_M (bottom) as a function of the fold change above LLoD (itself a function of the amount of contaminant included in the simulations).

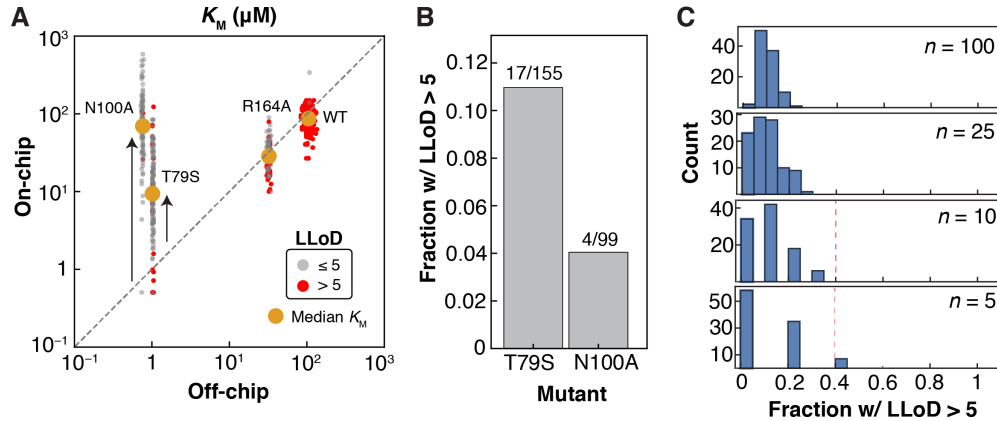


Fig. S16. Additional culling of LLoD false positives (>5-fold above the LLoD). (A) Determination of the LLoD false positive rate on tier I devices using a comparison of all on-chip measurements against the off-chip K_M values of PafA active site mutants. The tier I values of K_M indicate that T79S and N100A cannot be measured accurately (black arrows) due to contamination from WT-like enzyme. (B) The large number of T79S and N100A replicates (155 and 99, respectively) allows estimation of the false positive rate. The fraction of total T79S and N100A chambers that passed LLoD culling (*cf.* red and gray points in panel A) estimate a false positive rate of 10%. (C) Effect of a 10% false positive rate on the observed fraction of replicates >5-fold above the LLoD, as a function of the number of mutant replicates obtained (n , where $n = 0, 10, 25$, and 100). One hundred simulations were performed at each number of replicates. As we typically obtained 5–10 replicates of each mutant, the rates for any mutant for which <40% of total replicates passed the LLoD culling (red dashed line) on tier I devices was considered to be due to contamination. These tier I replicates were therefore not included in subsequent analyses and measurements were taken from the tier 2 and 3 devices only.

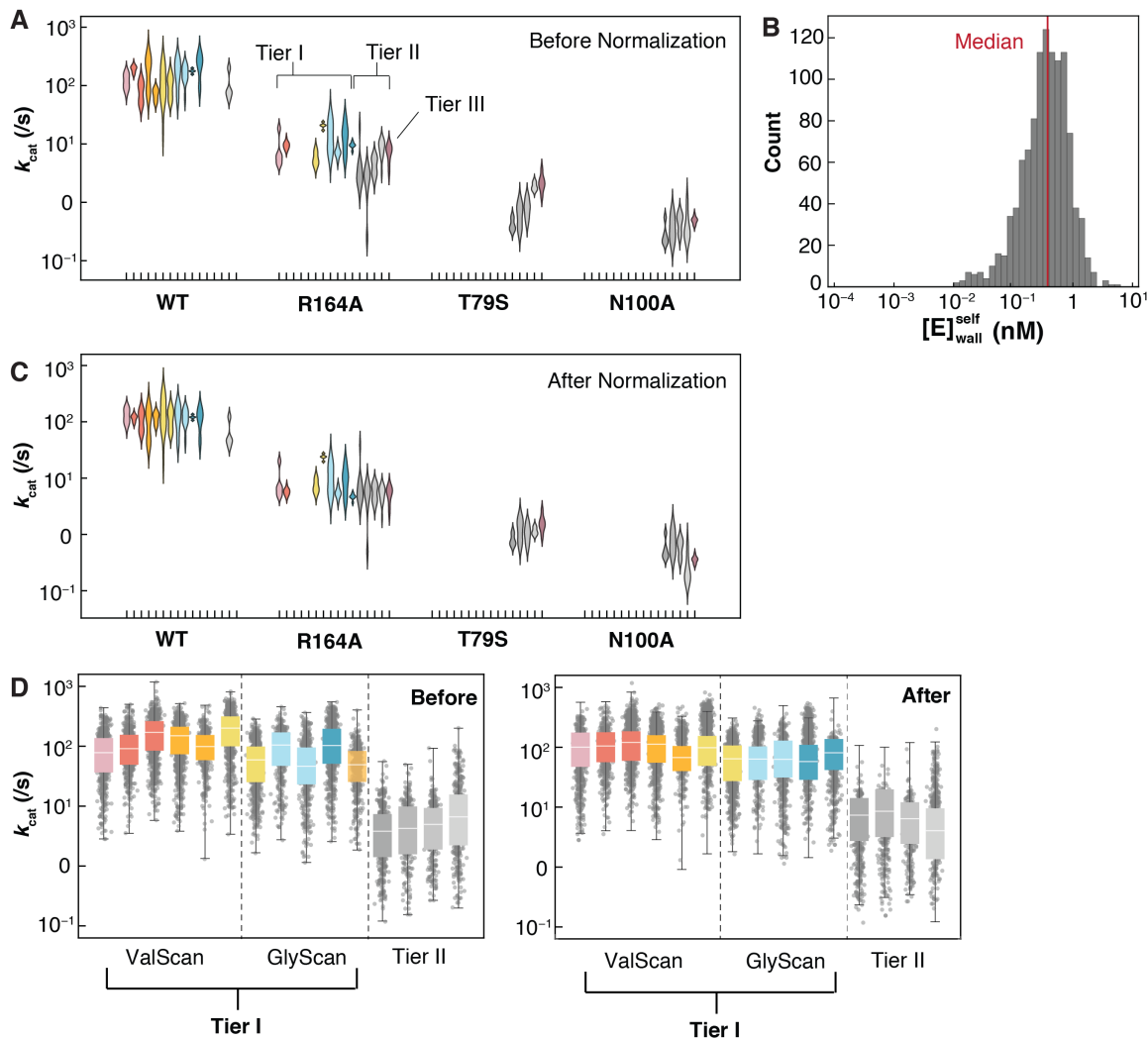


Fig. S17. Normalizing data across experiments and tiers. (A) k_{cat} distributions within each experiment for WT and active site single mutants before normalization. (B) Distribution of contributions from non-specifically bound enzyme (E_{wall}^{self}) to the total $[E]$ within each chamber. (C) k_{cat} distributions within each experiment for WT and active site single mutants after normalization. (D) k_{cat} distributions within each experiment for all chambers passing quality control filters, before and after cross-experiment normalization for tiers 1 and 2. White lines denote the median and boxes span 25% and 75% quantiles.

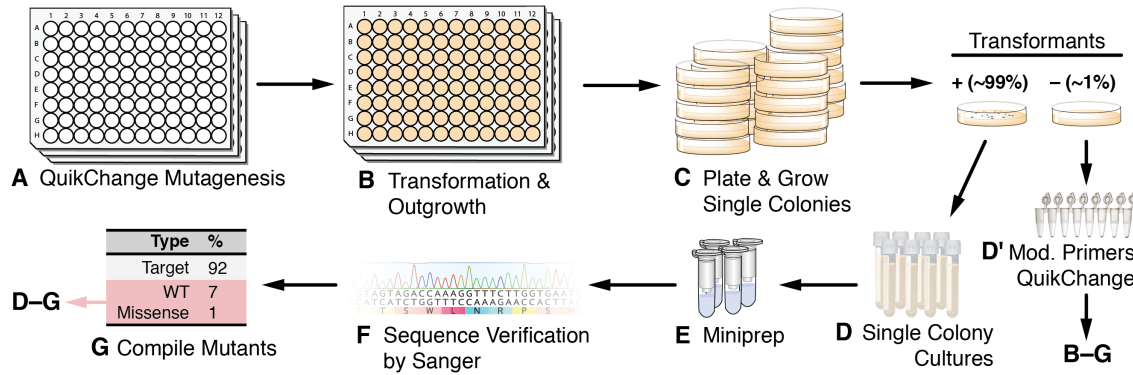


Fig. S18. High-throughput mutagenesis protocol to generate comprehensive single-site mutant libraries. (A) Parallelized QuikChange site-directed mutagenesis performed in 96-well plates. (B) Transformation of ultra-competent DH5alpha *E. coli* with QuikChange products and subsequent culture in deep well plates in SOC media for 1 h. (C) Plating of reactions on LB agar with ampicillin prior to growth overnight. (D) Picking single colonies for growth in 10 mL LB with ampicillin along with additional rounds of primer design, QuikChange, and transformation for reactions that did not yield colonies. (E) Miniprep plasmid isolation from 10 mL liquid cultures. (F) Sanger sequencing to verify construct sequence. (G) Picking, culturing, and sequencing additional colonies in cases where first-round sequencing identified WT constructs, undesired missense mutations, or insertions/deletions.

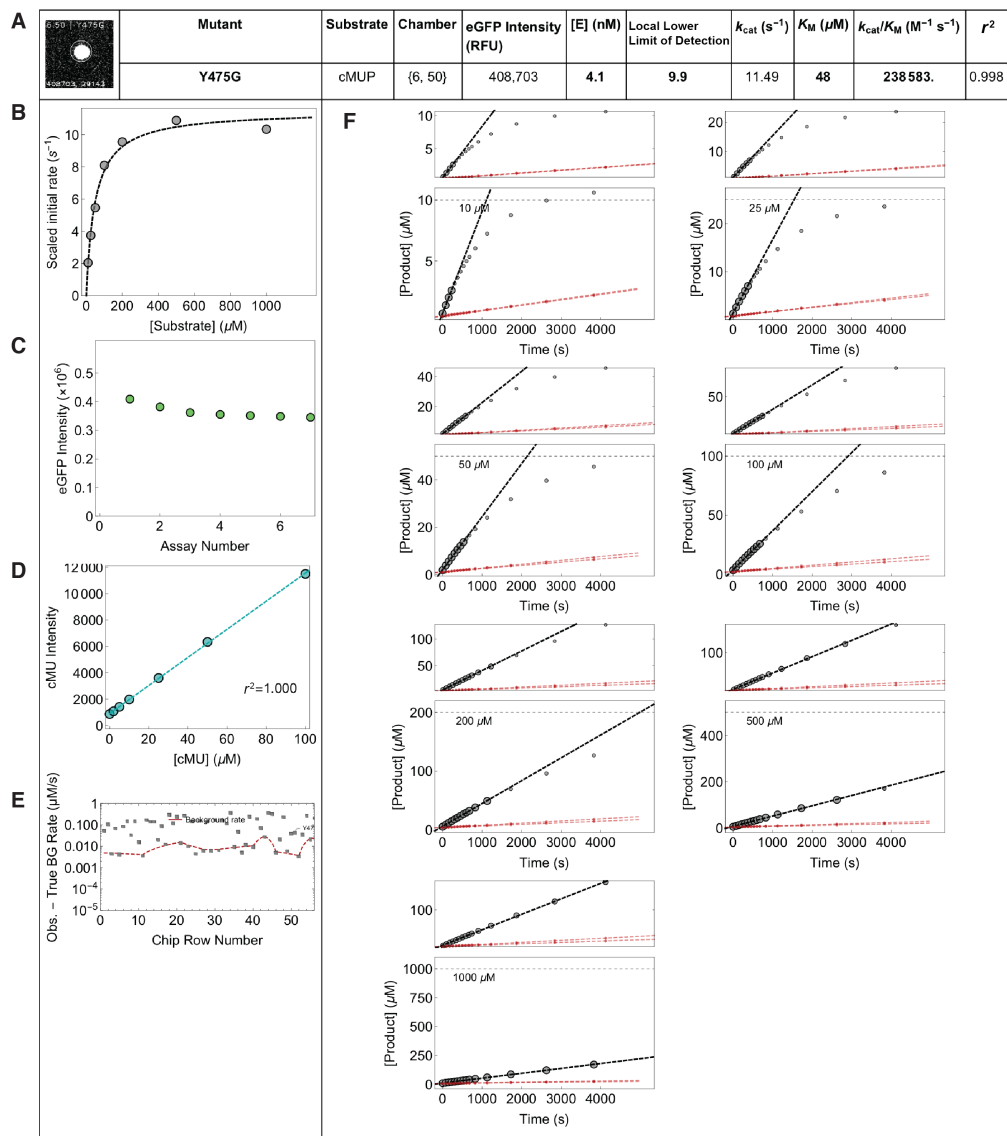


Fig. S19. Example data report for a single chamber following an HT-MEK cMUP kinetic experiment (7 individual cMUP assays). Each experiment returns 1,568 unique per-chamber reports containing: (A) Mutant identity, image of immobilized enzyme (eGFP channel), experimental parameters (substrate, chamber column and row, eGFP intensity, enzyme concentration, the rate compared to the local background (Local Lower Limit of Detection, or LLoD, see (E)), and Michaelis-Menten fit parameters (k_{cat} , K_M , k_{cat}/K_M , and associated r^2 values); (B) Michaelis-Menten fits to enzyme-concentration-scaled initial rates (gray); (C) Measured eGFP intensity prior to each assay; (D) Per-chamber product fluorescence standard curve and fit r^2 ; (E) Comparison of fitted rates (gray points) with the interpolated LLoD (red dashed line) for all chambers in the same column; (F) Full reaction progress curves (lower panels) and zoomed in plots (upper panels) for each substrate concentration with fitted initial rates (dashed gray lines). Large gray points were used to determine the linear fit; small gray points were measured but outside the linear region and not used to fit initial rates. Red points and lines denote the progress curves and linear fits from the nearest upstream and downstream background chambers used to determine the LLoD.

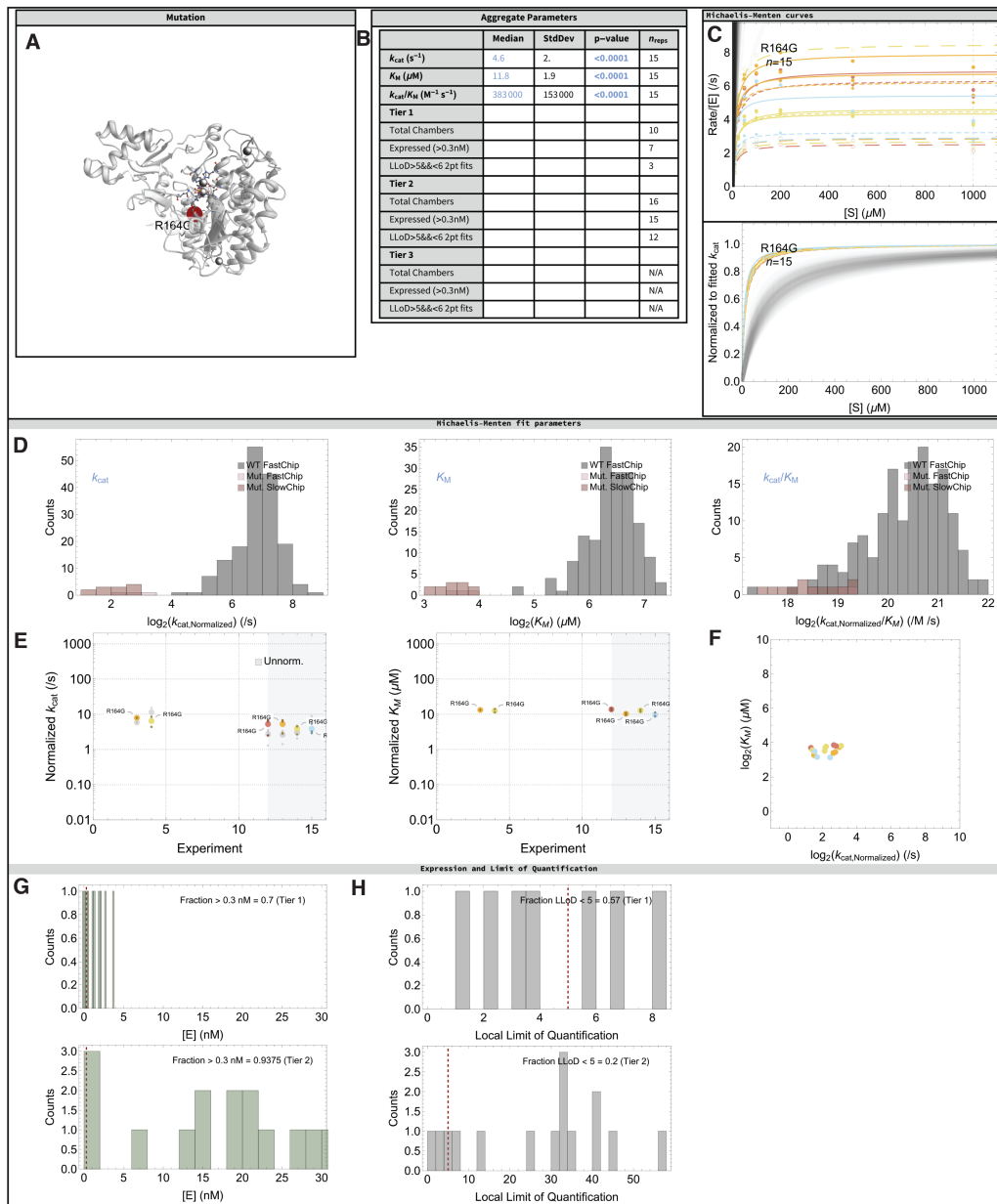


Fig. S20. Example aggregate cMUP summary for a representative mutant. (A) Name and location of mutation in PafA crystal structure (red sphere). (B) Aggregate parameter table. Number of replicates expressed and number that passed the LLoD filter in each experimental tier. (C) Fitted Michaelis-Menten curves for this mutant (colored lines) and for WT PafA (gray lines). (D) Distributions of mutant k_{cat} , K_M , and k_{cat}/K_M (red) relative to WT distributions (gray). (E) k_{cat} and K_M for replicates within each experiment. The gray region denotes tier 2 and 3 experiments. (F) Scatter plot of k_{cat} vs. K_M . (G) Histograms of $[E]$ for each replicate. Red dashed line denotes expression filter cutoff of 0.3 nM. (H) Histograms of v_i/LLoD , for all replicates. Red dashed line denotes the LLoD cutoff (5-fold above the LLoD). Aggregate pages also contain a table of k_{cat} , K_M , and k_{cat}/K_M values for each replicate (not shown).

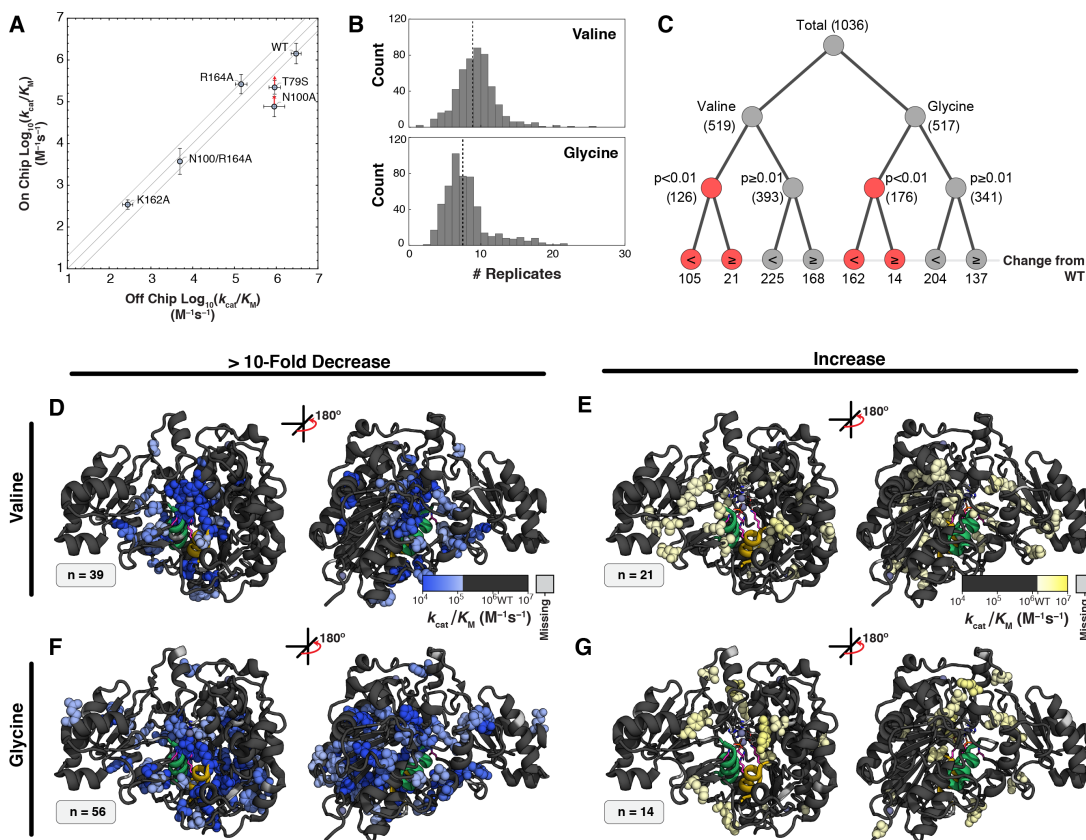


Fig. S21. Summary of Val and Gly library mutant cMUP k_{cat}/K_M values measured on chip. (A) Comparison of on- and off-chip cMUP k_{cat}/K_M measurements for WT PafA and 5 active site mutants. Error bars denote standard deviations (for > 2 replicates) and red arrows denote limits. (B) Histograms showing number of experimental replicates for all valine (top) and glycine (bottom) mutants. (C) Binary tree summarizing fraction of mutations with changes in activity from WT ($p < 0.01$) for valine and glycine mutant libraries. (D) Measured cMUP k_{cat}/K_M values for valine substitutions with decreases of at least ten-fold in activity relative to WT projected on the PafA structure (front and rear views). (E) Measured cMUP k_{cat}/K_M values for valine substitutions with increases in activity relative to WT ($p < 0.01$) projected on the PafA structure (front and rear views). (F) Measured cMUP k_{cat}/K_M values for glycine substitutions with decreases of at least ten-fold in activity relative to WT projected on the PafA structure (front and rear views). (G) Measured cMUP k_{cat}/K_M values for glycine substitutions with increases in activity relative to WT ($p < 0.01$) projected on the PafA structure (front and rear views).

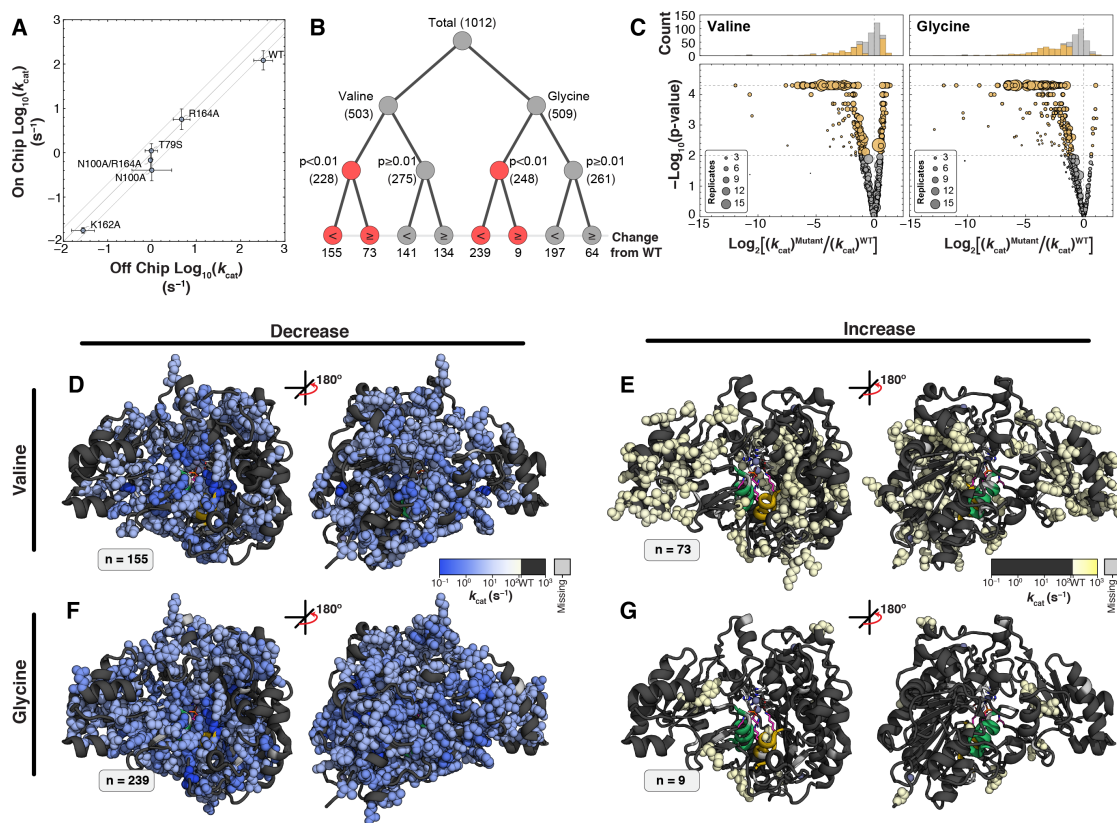


Fig. S22. Summary of on-chip measured cMUP k_{cat} values for Val and Gly library mutants. (A) Comparison of on- and off-chip cMUP k_{cat} measurements for WT PafA and 5 active site mutants. Error bars denote standard deviations (for > 2 replicates). (B) Binary tree diagram summarizing fraction of mutations with changes in activity from WT ($p < 0.01$) for valine and glycine mutant libraries. (C) Volcano plots showing p -value (as calculated from bootstrap analysis) as a function of measured effect size for valine (left) and glycine (right) mutants; mutants with differences in cMUP k_{cat} are shown in gold ($p < 0.01$). (D) Measured cMUP k_{cat} values for valine substitutions with decreases in activity relative to WT ($p < 0.01$) projected on the PafA structure (front and rear views). (E) Measured cMUP k_{cat} values for valine substitutions with increases in activity relative to WT ($p < 0.01$) projected on the PafA structure (front and rear views). (F) Measured cMUP k_{cat} values for glycine substitutions with decreases in activity relative to WT ($p < 0.01$) projected on the PafA structure (front and rear views). (G) Measured cMUP k_{cat} values for glycine substitutions with increases in activity relative to WT ($p < 0.01$) projected on the PafA structure (front and rear views).

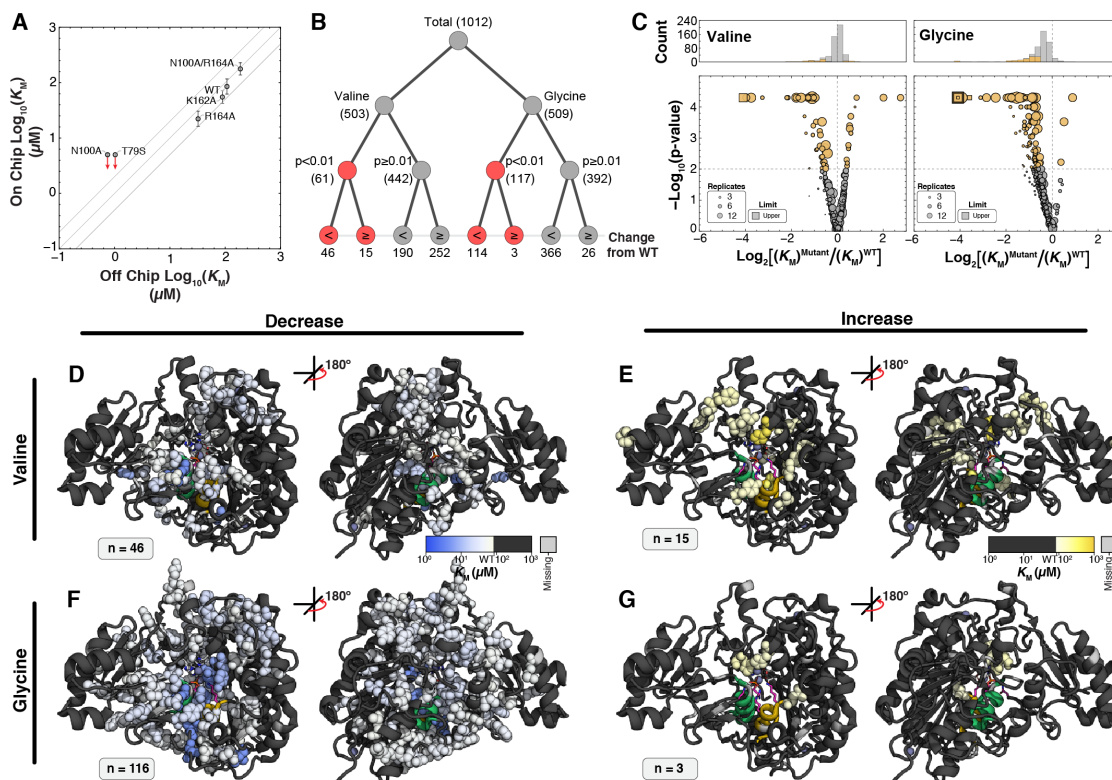


Fig. S23. Summary of on-chip measured cMUP K_M values for Val and Gly library mutants. (A) Comparison of on- and off-chip cMUP K_M measurements for WT PafA and 5 active site mutants. Error bars denote standard deviations (for > 2 replicates) and red arrows denote limits. (B) Binary tree diagram summarizing fraction of mutations with changes in activity from WT ($p < 0.01$) for valine and glycine mutant libraries. (C) Volcano plots showing p -value (as calculated from bootstrap analysis) as a function of measured effect size for valine (left) and glycine (right) mutants; mutants with differences in cMUP K_M are shown in gold ($p < 0.01$). (D) Measured cMUP K_M values for valine substitutions with decreases in activity relative to WT ($p < 0.01$) projected on the PafA structure (front and rear views). (E) Measured cMUP K_M values for valine substitutions with increases in activity relative to WT ($p < 0.01$) projected on the PafA structure (front and rear views). (F) Measured cMUP K_M values for glycine substitutions with decreases in activity ($p < 0.01$) relative to WT projected on the PafA structure (front and rear views). (G) Measured cMUP K_M values for glycine substitutions with increases in activity relative to WT ($p < 0.01$) projected on the PafA structure (front and rear views).

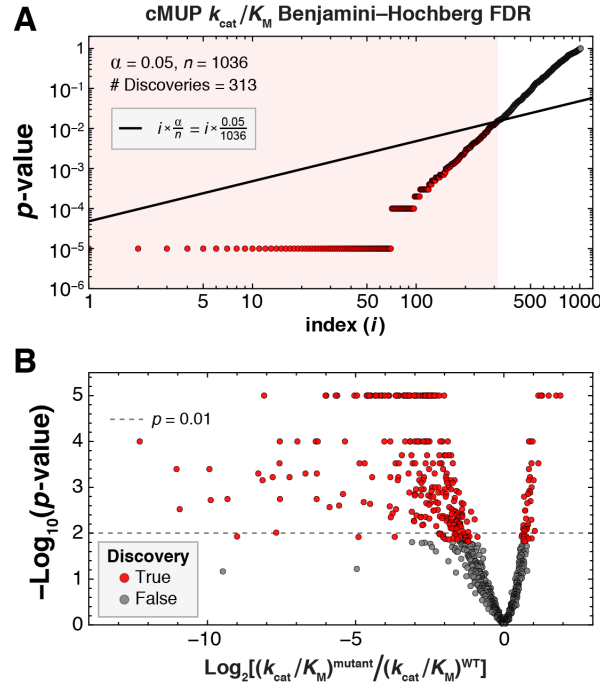


Fig. S24. Benjamini-Hochberg false discovery rate (FDR) controlling procedure. (A) p -values for median cMUP k_{cat}/K_M values for 1036 Val and Gly mutants (markers), sorted by p -value. Black line indicates predicted Benjamini-Hochberg FDR at $\alpha = 0.05$, calculated using the equation shown in the inset. The pink box denotes the range of observations considered discoveries under our FDR controlling procedure. (B) Volcano plot showing true discoveries declared under this FDR controlling procedure (red) co-plotted with all other observations (gray). The horizontal dashed line denotes $p = 0.01$, the threshold used to define strong evidence of mutational effects.

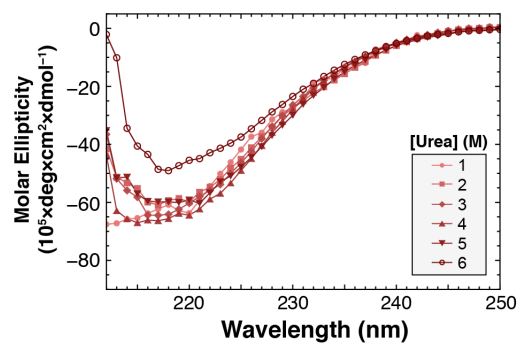


Fig. S25. Circular dichroism (CD) spectra of WT PafA over-expressed in *E. coli*, purified, and subjected to 2 weeks of incubation with urea in the presence of 100 μM Zn^{2+} .

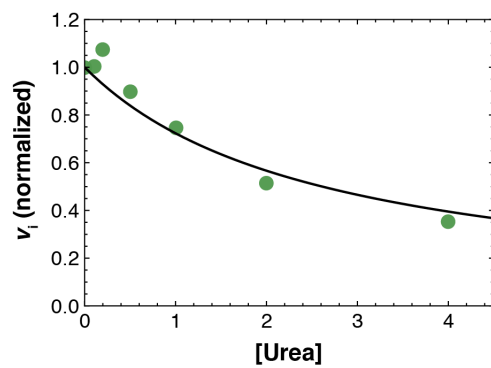


Fig. S26. Apparent competitive inhibition of PafA by urea. Initial rates of WT PafA hydrolysis (500 μ M MepNPP) as a function of added urea concentration (green), normalized to that at 0 M urea, are well fit by a model of competitive inhibition (**Eq. 18**) with a K_i of 2.6 M ($r^2 = 0.99$).

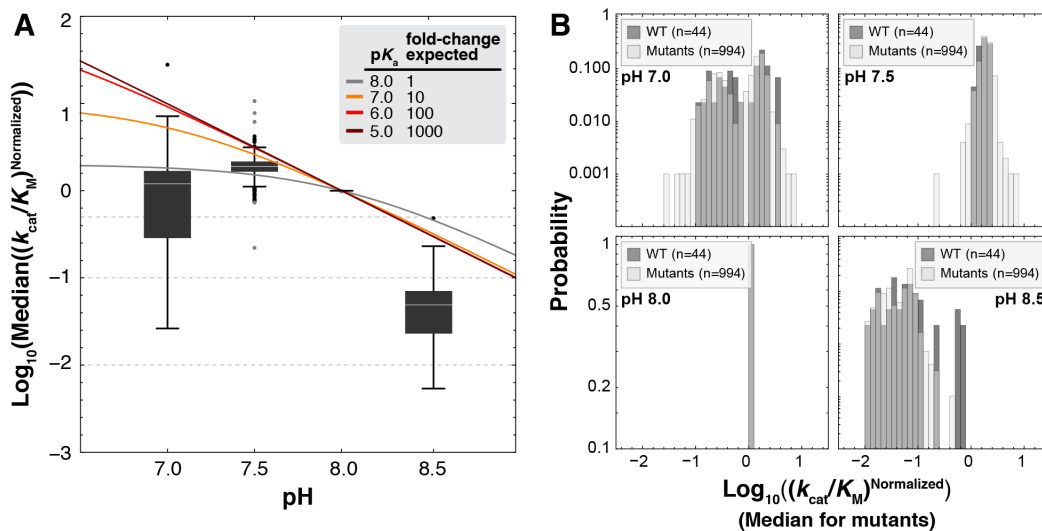


Fig. S27. pH-dependence of observed cMUP k_{cat}/K_M for valine and glycine scan mutants. (A) Box and whisker plots of cMUP k_{cat}/K_M values measured on-chip for all mutants (normalized to k_{cat}/K_M at pH 8.0) at pH 7, 7.5, 8, and 8.5. Curves denote predicted k_{cat}/K_M values (also normalized to the pH 8.0 values) for enzymes with pK_a values of 5.0, 6.0, 7.0, and 8.0 (the value previously reported for WT PafA) (16); all curves assume a single inhibitory pK_a and that the enzyme is full inactivated at high pH. The observed behavior is most consistent with mutants having an unchanged pK_a of 8.0 (B) Distributions of observed normalized k_{cat}/K_M values for mutants and WT PafA at each pH.

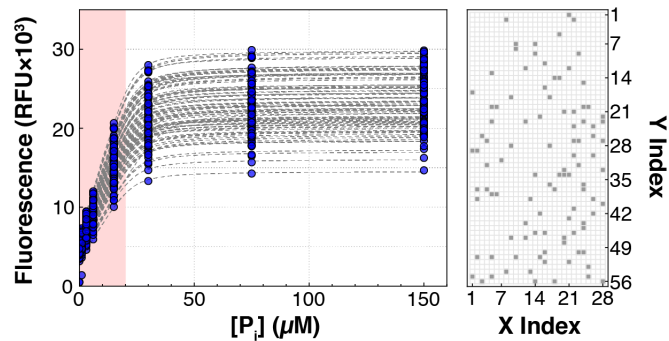


Fig. S28. Fluorescence standard curves relating measured Phosphate Sensor (*I8*) fluorescence intensities to inorganic phosphate (P_i) concentrations on chip. Measured fluorescence intensities for chambers throughout the device containing 30 μM PBP in the presence of increasing amounts of P_i (left, blue markers). Individual chamber intensities were fit to a single-site binding isotherm model (gray dashed lines; see **Materials and Methods**) to allow subsequent per-chamber conversion of measured intensities to P_i concentrations. Initial rate fits were limited to points in the region indicated by the pink window (up to 20 μM P_i). Locations of randomly selected plotted chambers within the device (right).

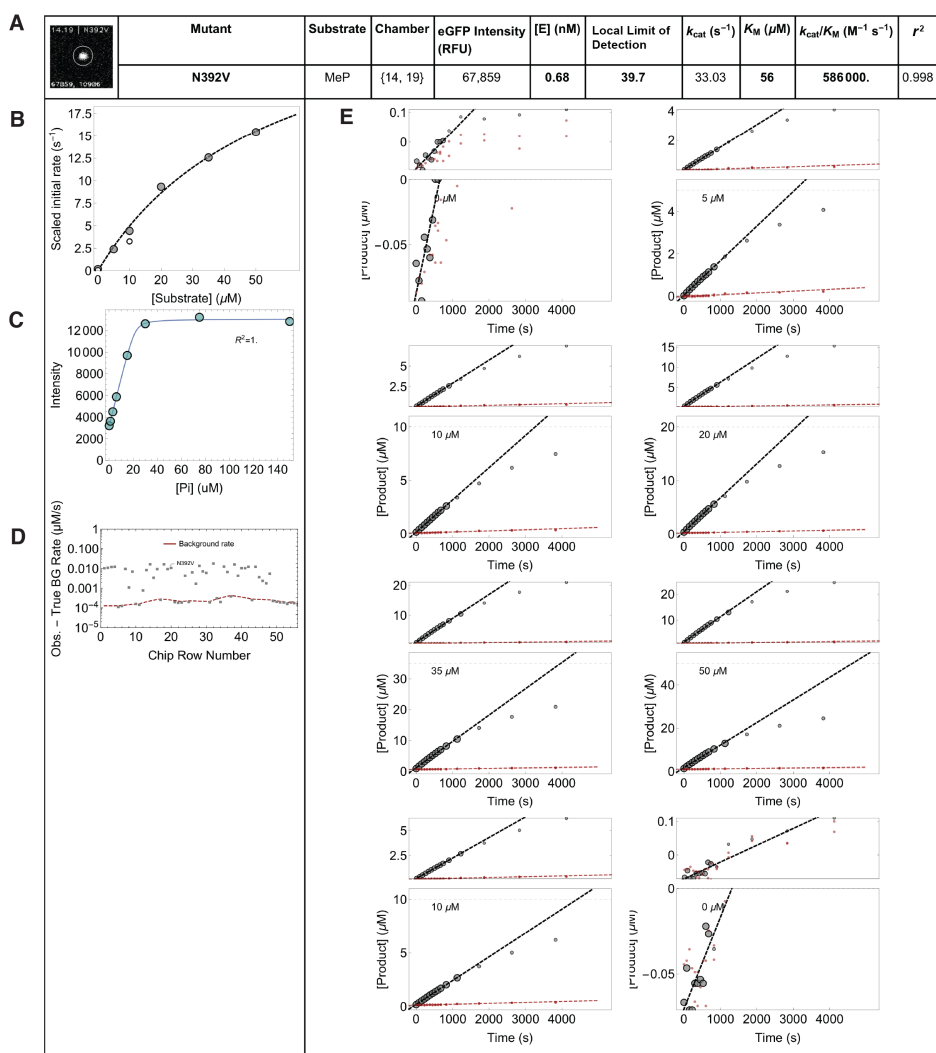


Fig. S29. Example data report for a single chamber after an HT-MEK MeP hydrolysis kinetic experiment (8 individual assays). Each experiment returns 1,568 unique per-chamber reports containing: (A) Mutant identity and image of immobilized enzyme (eGFP channel), experimental parameters (substrate, chamber column and row, eGFP intensity, enzyme concentration, rate compared to the local background (LLoD), and Michaelis-Menten fit parameters (k_{cat} , K_M , k_{cat}/K_M , and r^2); (B) Michaelis-Menten fits to scaled initial rates (gray) with initial rate from replicate assay (white); (C) Per-chamber product fluorescence standard curve and fit r^2 ; (D) Comparison of fitted rates (gray points) with interpolated local lower limit of quantification (LLoD, red dashed line) within this chamber's full column; (E) Full reaction progress curves (lower panels) and expanded plots (upper panels) for each substrate concentration, with fitted initial rates shown as dashed gray lines. Large gray points were used to determine the linear fit, small gray points were measured but outside the linear region and not used to fit initial rates. Red points and lines denote the progress curves and linear fits from the nearest upstream and downstream background chambers used to determine the local background.

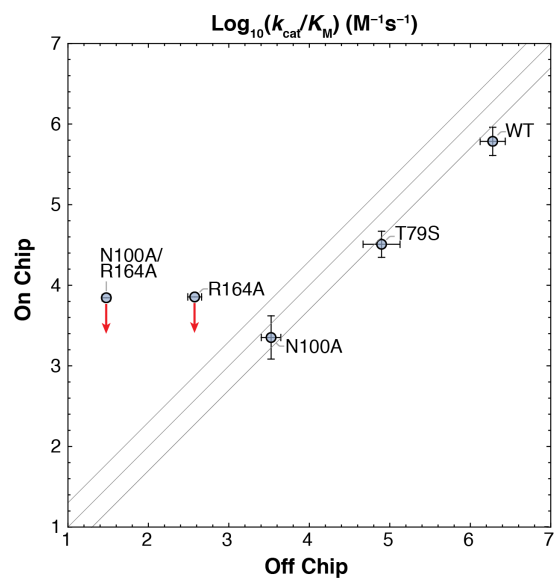


Fig. S30. Comparison of on-chip (eGFP-tagged) and off-chip (strepII-tagged) MeP k_{cat}/K_M values for PafA active site mutants. On-chip median values were calculated from measurements of active site variant controls incorporated in the valine and glycine scanning mutant assays. Upper limits for on-chip measurements are denoted by red arrows. Off-chip values are means of two or more replicates and error bars denote standard deviations.

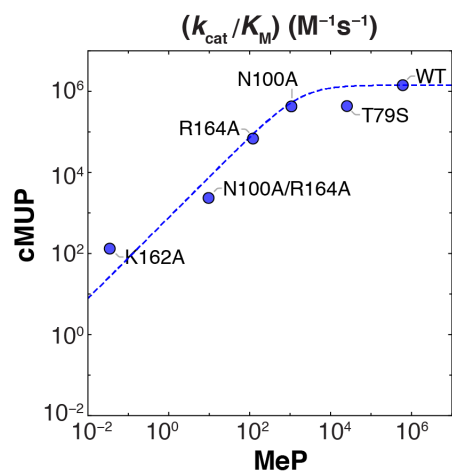


Fig. S31. Off-chip measured cMUP k_{cat}/K_M and MeP k_{cat}/K_M values for strepII-tagged WT PafA and 5 active site mutants with associated non-linear fit to the relative reactivity relationship predicted by their kinetic rate equations (**Eq. 31**). Activity measurements were made using purified enzyme expressed in *E. coli*; the fit to **Eq. 31** yielded $f_r = 776 \pm 126$ (median \pm SEM), which specifies the relative turnover rates of the substrates when the hydrolysis step is rate limiting for both (as described in **Supplementary Text S2**).

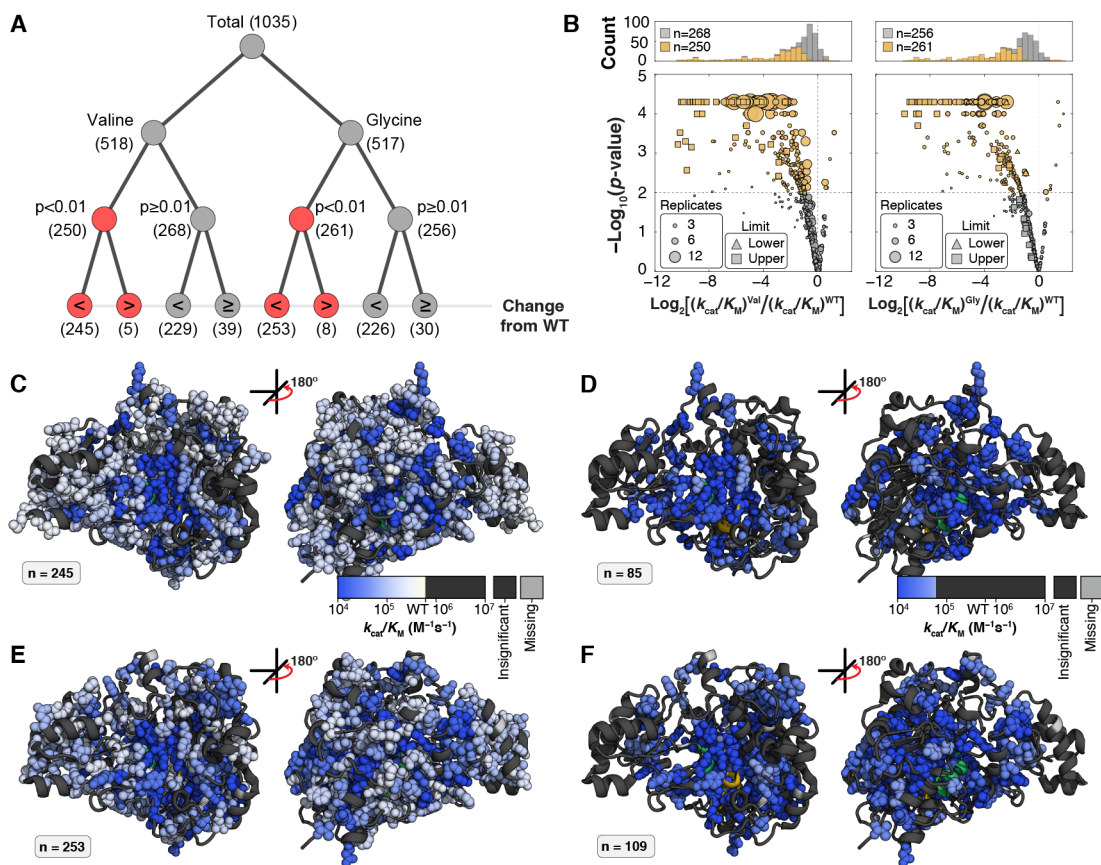


Fig. S32. Summary of on-chip measured MeP k_{cat}/K_M values for glycine and valine library mutants. (A) Tree diagram describing the number of mutants with MeP k_{cat}/K_M effects ($p < 0.01$). (B) Volcano plots showing fold-effects, p -value, and number of replicates for the valine scanning mutants (left) and glycine scanning mutants (right). Effects with $p < 0.01$ are shown in gold. (C–F) Structural representations of positions with decreases in MeP k_{cat}/K_M upon mutation to valine (C, less than WT and $p < 0.01$; D, 10-fold or greater decrease from WT and $p < 0.01$) or glycine (E, less than WT and $p < 0.01$; F, 10-fold or greater decrease from WT and $p < 0.01$). “Nucleophile” and “Monoester” helices are shown in green and gold, respectively, but are largely obscured by spheres indicating positions with effects.

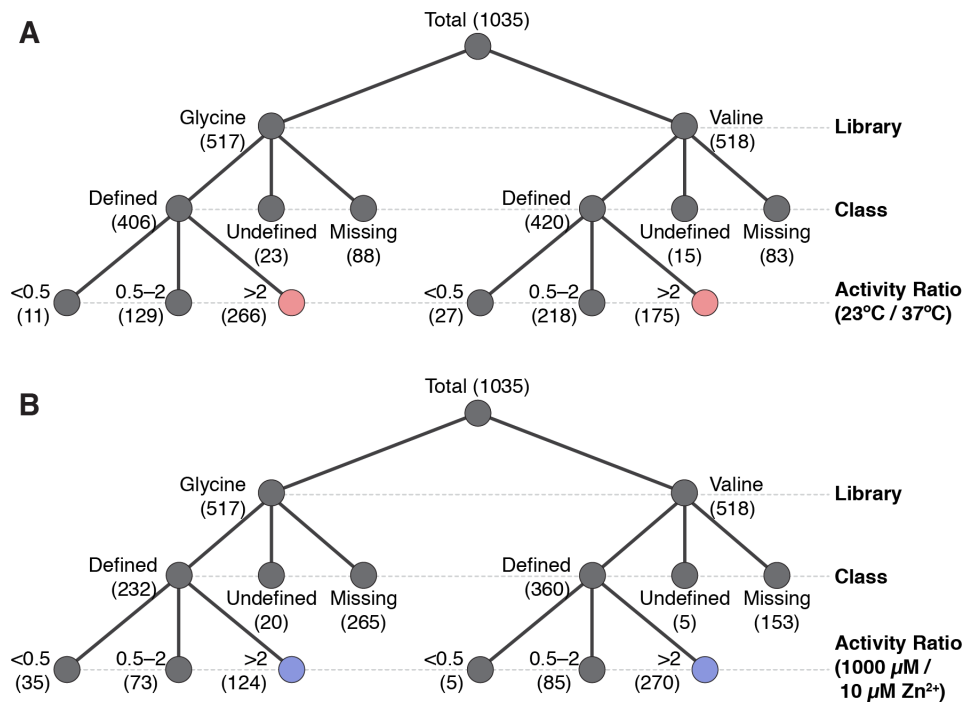


Fig. S33. Number of valine and glycine mutants with changes in cMUP k_{cat}/K_M upon changes in expression (but not assay) conditions. Trees indicating counts of (A) temperature- and (B) Zn-dependent expression effects (T-Effect and Zn-Effect; Eq. 9 and 10, respectively) on k_{cat}/K_M for Val and Gly library mutants. Mutants for which the activity ratio may be less than or greater than unity (as they are limits in one or both direction) are considered “Undefined” and mutants lacking an estimate under either or both expression conditions are “Missing.”

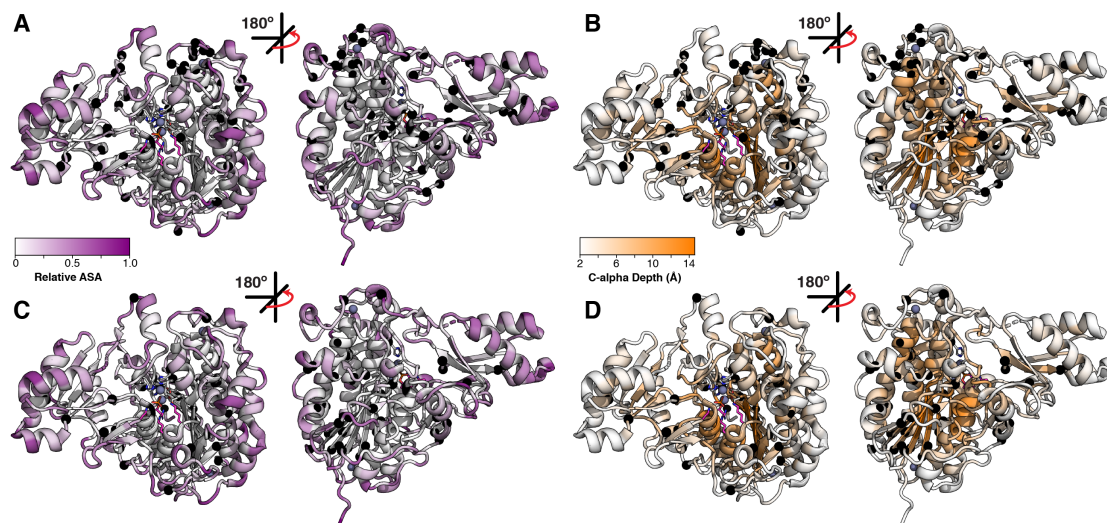


Fig. S34. Significant Zn-Effects and T-Effects and residue biophysical features visualized on a ribbon representation of PafA covalently bound to phosphate (PDB ID: 5TJ3). Positions of substitutions with large Zn-Effects (black spheres) plotted on PafA colored by (A) relative solvent accessible surface area (ASA) and (B) minimum depth of each residue's C-alpha from the reduced surface. Positions of substitutions with large T-Effects (black spheres) plotted on PafA colored by (C) relative solvent accessible surface area (ASA) and (D) minimum depth of each residue's C-alpha from the reduced surface. Active site residues T79, N100, R164, and K162 are represented with magenta sticks. Relative ASA was not calculable for residue 79 (black ribbon).

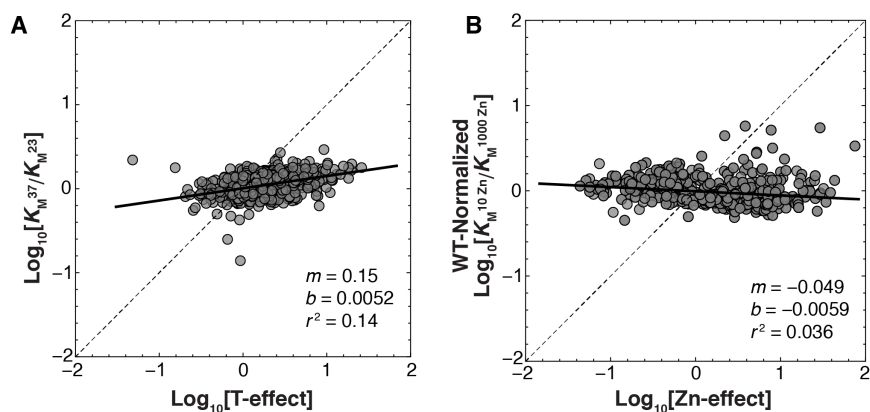


Fig. S35. Measured K_M values as a function of temperature- and zinc-effects (T-Effect and Zn-Effect; **Eq. 9** and **10**, respectively) during expression. (A) Log_{10} -transformed ratios of K_M values at 37°C and 23°C (grey markers) as a function of log_{10} -transformed T-effect (**Eq. 9**). (B) WT-normalized log_{10} -transformed ratio of K_M values at $10\ \mu\text{M}$ and $1000\ \mu\text{M}$ ZnCl_2 (grey markers) as a function of log_{10} -transformed Zn-effect (**Eq. 10**). Dashed grey lines denote a 1:1 relationship; solid black lines correspond to linear regressions with slopes, intercepts, and r^2 values as indicated.

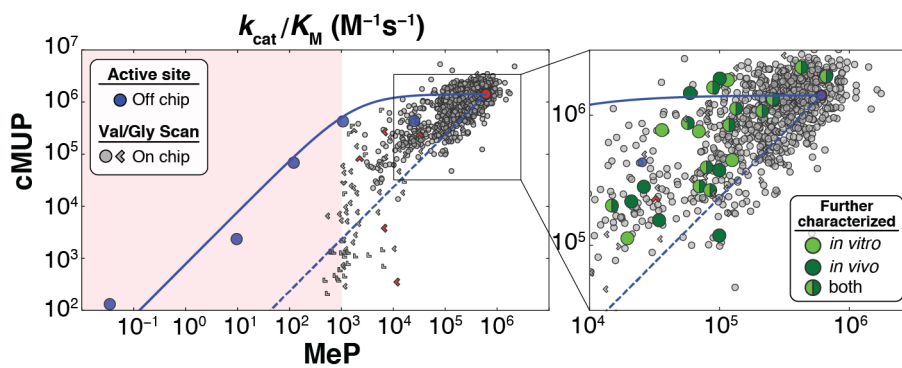


Fig. S36. Mutants subjected to further characterization *in vitro* and *in vivo*. Measured k_{cat}/K_M for MeP vs. k_{cat}/K_M for cMUP for strepII-tagged active site mutants off-chip (blue points) and for valine and glycine library mutants. Limits in one or both directions are denoted by chevrons pointing in the direction or quadrant, respectively, of the limit. Green points correspond to Val and Gly library mutants subjected to further off-chip characterization *in vitro* (light green) and/or *in vivo* (dark green).

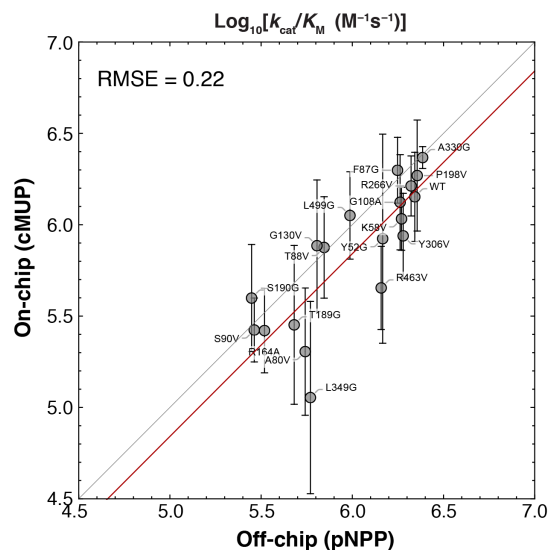


Fig. S37. Comparison of measured on- and off-chip measured aryl monoester (cMUP and pNPP, respectively) $k_{\text{cat}}/K_{\text{M}}$ values for in vitro expressed eGFP-tagged WT PafA and 18 library mutants (grey markers, see **Table S4** and **Materials and Methods**). The red line corresponds to a linear least-squares regression with a constrained slope of unity using \log_{10} -transformed data (fit intercept = -0.16); y-error bars indicate the standard deviations of on-chip measurements. An RMSE of 0.22 in \log_{10} -transformed space corresponds to a 1.7-fold effect.

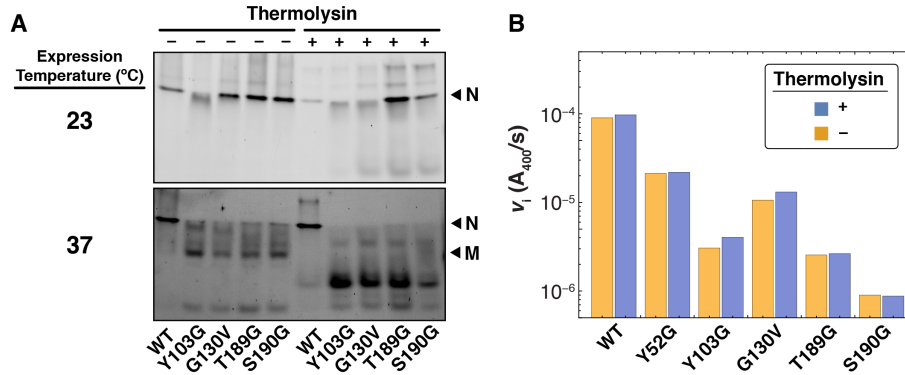


Fig. S38. Native gel electrophoresis and turnover kinetics support the existence of a misfolded state among library mutants expressed *in vitro* off-chip. (A) Native gel electrophoresis of a subset of eGFP-tagged mutants expressed at either 23°C (top) or 37°C (bottom) in the presence (+) or absence (–) of thermolysin. When expressed at 23°C (left), all constructs appeared as a single band with the same electrophoretic mobility as that of WT (the native “N” state). By contrast, expression at 37°C resulted in the appearance of common higher-mobility species among the mutants, but not the WT (the putatively misfolded “M” state). The addition of thermolysin (right) led to near-complete degradation of the M state (37°C panel) but not the N state (23°C panel). (B) Measured initial rates of pNPP turnover for WT PafA and five library mutants expressed off-chip at 37°C, assayed with and without prior thermolysin treatment. Thermolysin treatment did not significantly alter the activities, suggesting that the protease-susceptible M state observed in (A) was catalytically inactive and did not contribute to the observed rate.

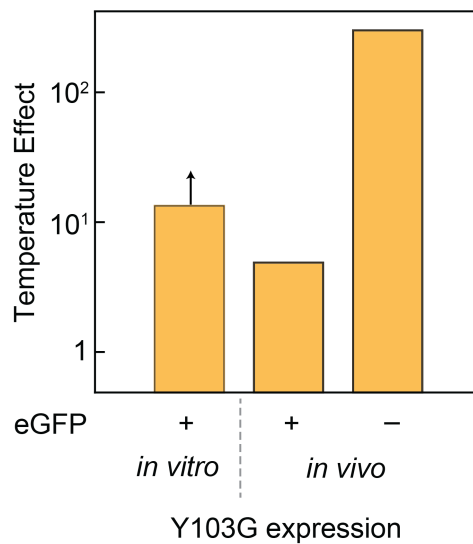


Fig. S39. Comparison of temperature effects (ratio of WT-normalized activities at 23°C and 37°C) of the Y103G mutant expressed *in vivo* in the presence and absence of the eGFP tag, and *in vitro* (on-chip), at 23°C and 37°C. The black arrow denotes that the *in vitro* temperature effect is a lower limit, arising because the measured k_{cat}/K_M of 37°C-expressed Y103G is an upper limit. Data from table S6.

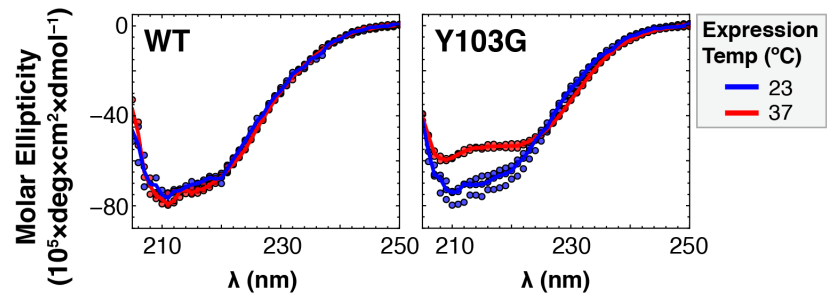


Fig. S40. CD spectra for strepII-tagged WT PafA and the temperature-sensitive mutant Y103G expressed in *E. coli* at low (23°C, blue markers) and high (37°C, red markers) temperature. Solid lines are the medians of 2 or 3 replicate spectra obtained in different buffers (see **Materials and Methods**).

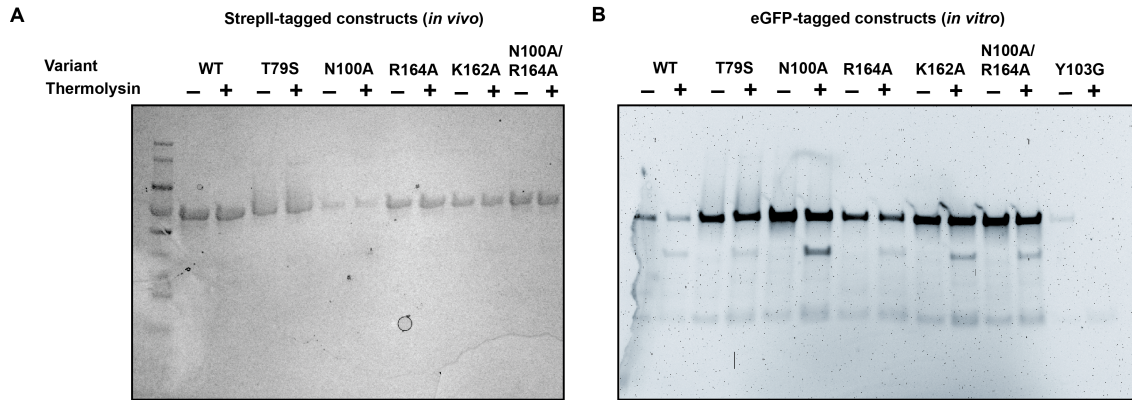


Fig. S41. Thermolysin degradation assays indicate that PafA active site mutants are not significantly misfolded. (A) SDS-PAGE of *in vivo* expressed, strepII-tagged WT and the five PafA active site mutants used to define the relative reactivity relationship between cMUP and MeP, untreated with thermolysin (-) or exposed to thermolysin proteolysis for 10 min. (+). (B) SDS-PAGE of *in vitro* expressed (PURExpress), eGFP-tagged WT, active site variants, and the misfolding prone mutant Y103G, untreated with thermolysin (-) or exposed to thermolysin proteolysis for 10 min (+).

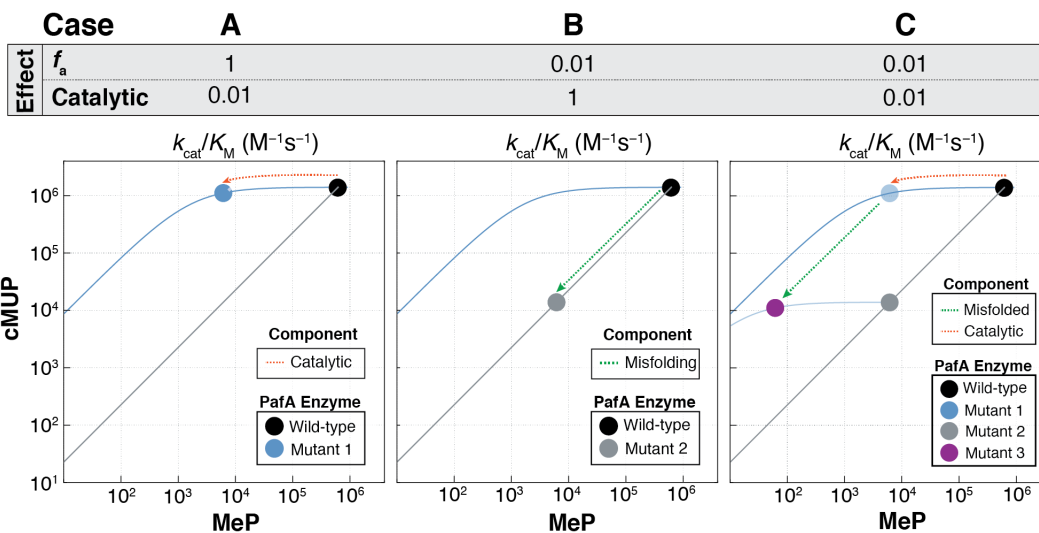


Fig. S42. Three examples illustrating how observed mutational effects on k_{cat}/K_M can arise from combinations of catalytic and misfolding effects. (A) Case 1: Mutation has a 100-fold effect on the chemical step of catalysis (k_{cat}/K_M) (red dashed arrow) from wild-type (black point). The effect is much greater for MeP hydrolysis ($(k_{cat}/K_M)^{MeP}$) as hydrolysis remains diffusion-limited for cMUP ($(k_{cat}/K_M)^{cMUP}$) (blue point and curve). (B) Case 2: Mutation results in 99% of the protein misfolding, but the folded 1% has wild-type ($(k_{cat}/K_M)^{MeP}$) and ($(k_{cat}/K_M)^{cMUP}$), resulting in an observed 100-fold drop in k_{cat}/K_M for both substrates (gray point, and green dashed arrow). (C) Case 3: Mutation results in 99% of the protein misfolding, as in (B) (green dashed arrow), but with an additional 100-fold effect on the chemical step (red dashed arrow). The observed rates (purple point) result from a combination of misfolding (gray point) and catalytic effects (blue point). The observed $(k_{cat}/K_M)^{MeP}$ is therefore decreased 10^4 -fold from the wild-type value, while the observed $(k_{cat}/K_M)^{cMUP}$ is only decreased 10^2 -fold due to the misfolding effect, as hydrolysis remains diffusion-limited for cMUP.

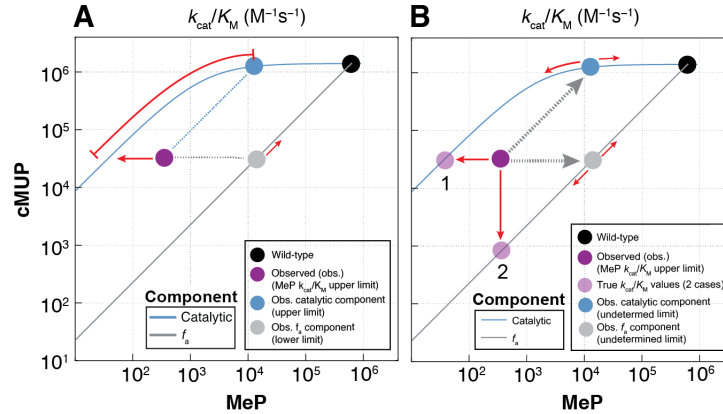


Fig. S43. Effect of observed MeP and cMUP k_{cat}/K_M upper limits on calculated catalytic and fraction active (f_a) effects. (A) Effect of a MeP k_{cat}/K_M upper limit. As determination of catalytic and f_a effects depends on both cMUP and MeP k_{cat}/K_M , variants for which the observed (obs.) MeP k_{cat}/K_M is an upper limit (dark purple point) will result in the intrinsic catalytic k_{cat}/K_M (blue point) and f_a (gray point) effects being upper and lower limits, respectively. The red arrows denote the direction of the limits. It is therefore possible to obtain upper limits for catalytic effects and estimate their significance; however, p -values of f_a effects cannot be determined. (B) Effect of both MeP and cMUP k_{cat}/K_M upper limits on calculated catalytic and f_a components (the gray arrows denote the determination of catalytic and f_a components from the observed point). When both the observed MeP and cMUP k_{cat}/K_M are upper limits (red arrows and dark purple point), the true effect can be fully catalytic (case 1, light purple), fully due to f_a (case 2, light purple), or any combination of the two components. Therefore, neither the catalytic and f_a effects of the variants nor their p -values can be determined.

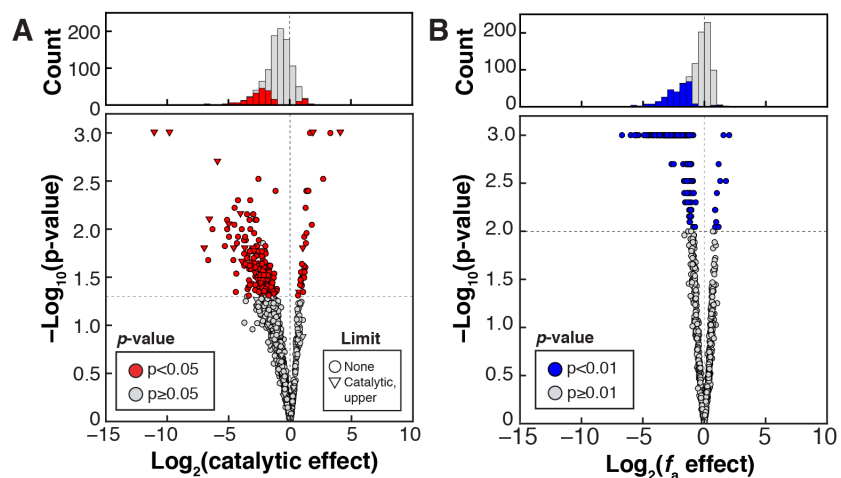


Fig. S44. Volcano plots of (A) catalytic effects and (B) fraction active (f_a) effects for all measurable variants in the valine and glycine libraries. Upper limits of p -values for upper $k_{\text{cat}}/K_M^{\text{chem}}$ limits (triangles) can only be inferred for catalytic effects (see **Materials and Methods** and **Fig. S43**); therefore, limits are included in (A) but not (B). For both, vertical grid lines denote no change from WT, while horizontal grid lines denote the p -value thresholds of 0.05 and 0.01, respectively.

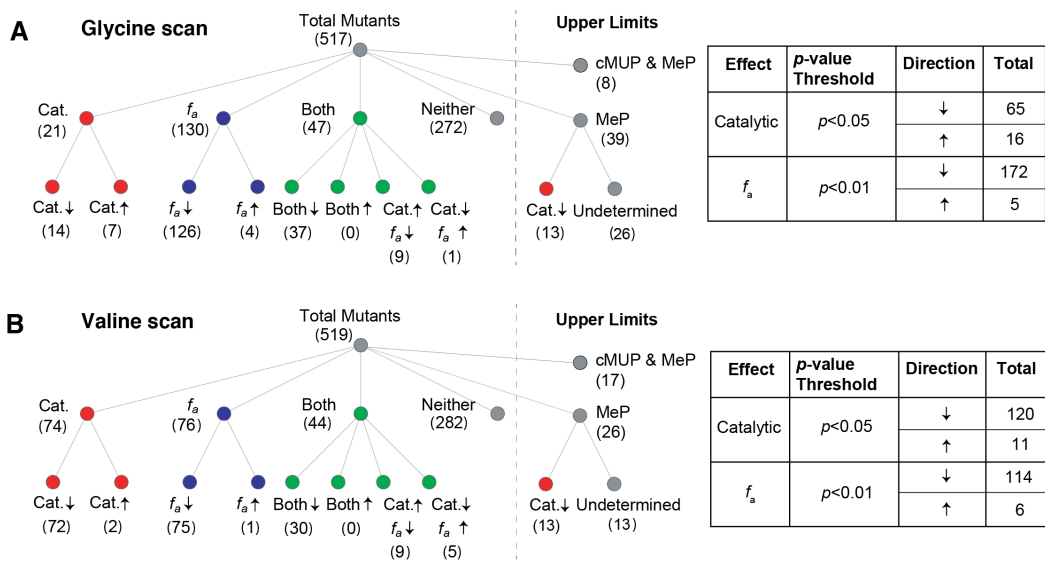


Fig. S45. Counts of variants within the (A) glycine and (B) valine scan libraries with catalytic (Cat.) effects, fraction active (f_a) effects, both catalytic and fraction active effects, and variants without significant effects. Mutants with catalytic effects ($p < 0.05$) are colored red, mutants with f_a effects only ($p < 0.01$) are colored blue, and mutants with both catalytic and f_a effects are colored green, with the number of mutants within each set given in brackets. Arrows denote the direction of effects relative to WT. P -values for limits can only be inferred for catalytic effects, as described in **Materials and Methods** (and see **Fig. S43**). Total (cumulative) numbers of catalytic and f_a effects (including the mutants with both effects and limits) are given in the tables to the right.

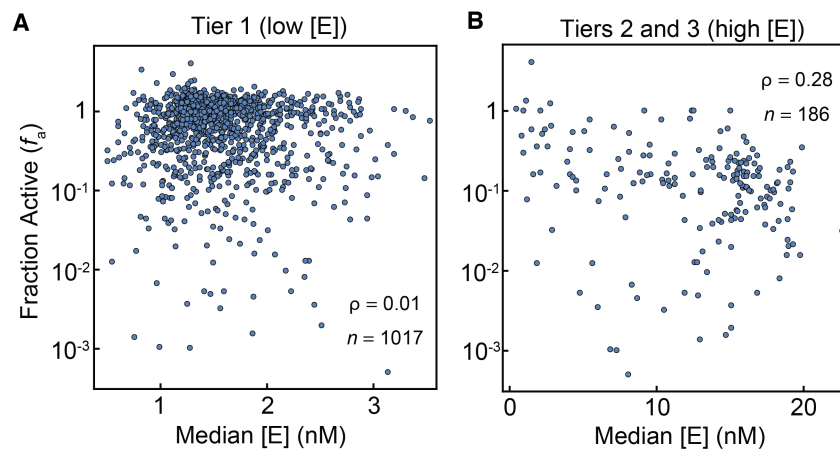


Fig. S46. Scatter plots of fraction active and median enzyme concentration ([E]) for (A) low [E] (Tier 1) and (B) high [E] (Tiers 2 and 3) devices. Correlations were measured using Spearman's rank correlation coefficients (ρ). These ρ values are reported in the insets.

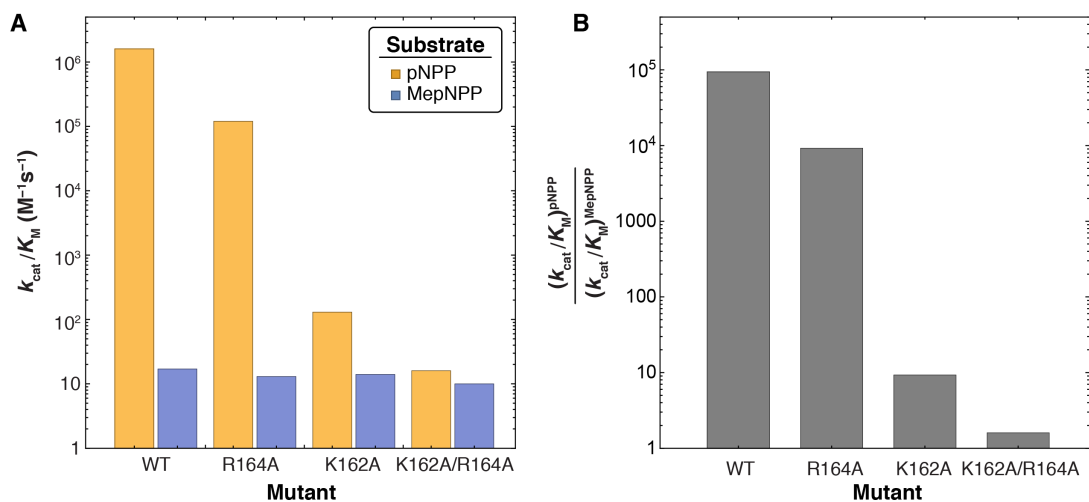


Fig. S47. K162 and R164 determine specificity for monoester hydrolysis. (A) Off-chip measurements of k_{cat}/K_M for pNPP (monoester) and MepNPP (diester) hydrolysis by strepII-tagged WT PafA and K162/R164 mutants. (B) Ratio of k_{cat}/K_M for pNPP and MepNPP hydrolysis (“specificity”) for WT PafA and K162/R164 mutants. Data in both panels reproduced from (16).

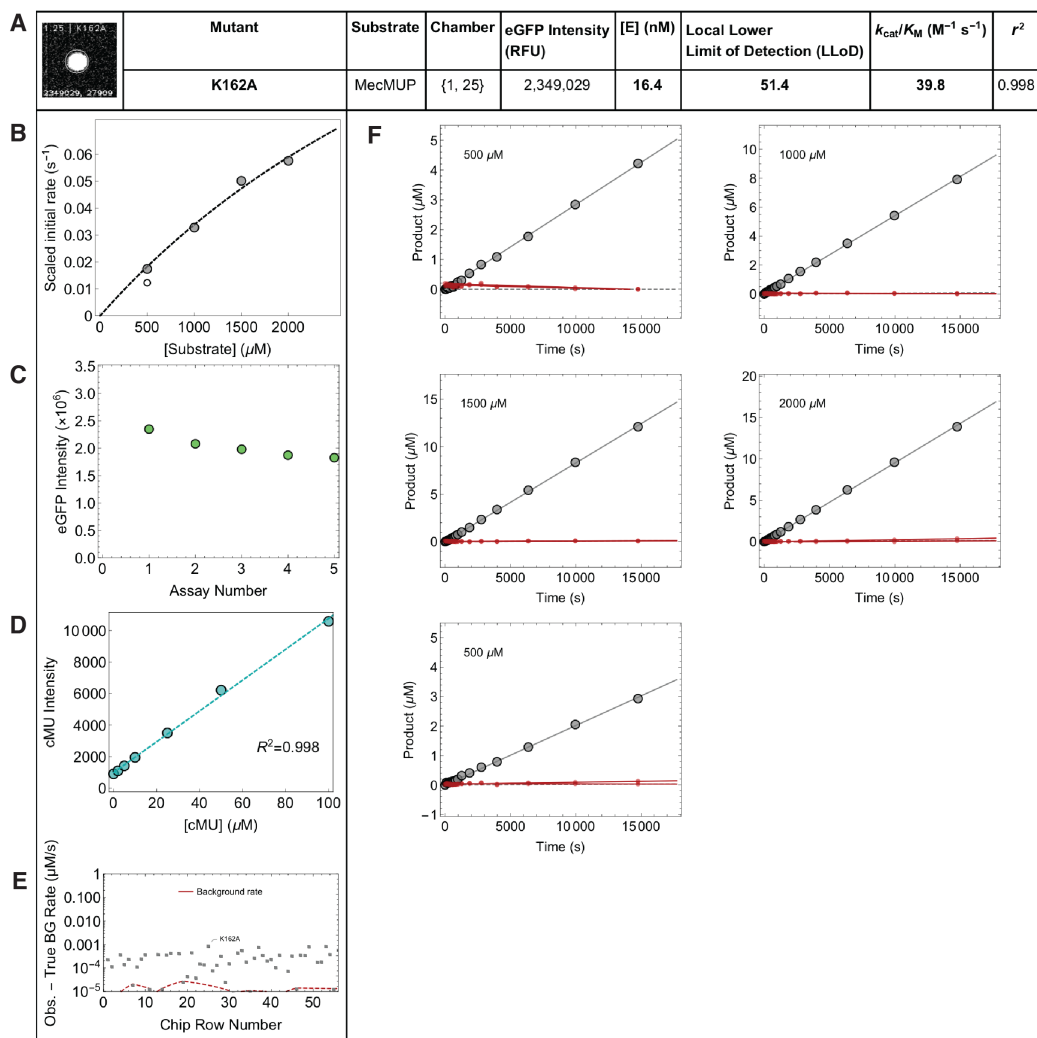


Fig. S48. Example data report for a single chamber after an HT-MEK experiment measuring MecMUP hydrolysis (5 individual assays). Each experiment returns 1,568 unique per-chamber reports containing: (A) Identity of the mutant in each chamber, with image of immobilized enzyme (eGFP channel) and experimental parameters including substrate, chamber column and row, eGFP intensity, enzyme concentration, the rate compared to the local background (LLoD, see (E) and **Materials and Methods**), k_{cat}/K_M , and r^2 ; (B) Michaelis-Menten fits to scaled initial rates (gray) with initial rate from replicate assay (white); (C) Measured eGFP intensity for each assay; (D) Per-chamber product fluorescence standard curve and fit r^2 ; (E) Comparison of fitted rates (gray points) with the interpolated local lower limit of quantification (LLoD, red dashed line) within this chamber's full column (see **Materials and Methods**); (F) Full reaction progress curves (lower panels) and expanded plots (upper panels) for each substrate concentration, with fitted initial rates shown as dashed gray lines. Large gray points were used to determine the linear fit, small gray points were measured but outside the linear region and not used to fit initial rates. Red points and lines denote the progress curves and linear fits from the nearest upstream and downstream background chambers used to determine the local background.

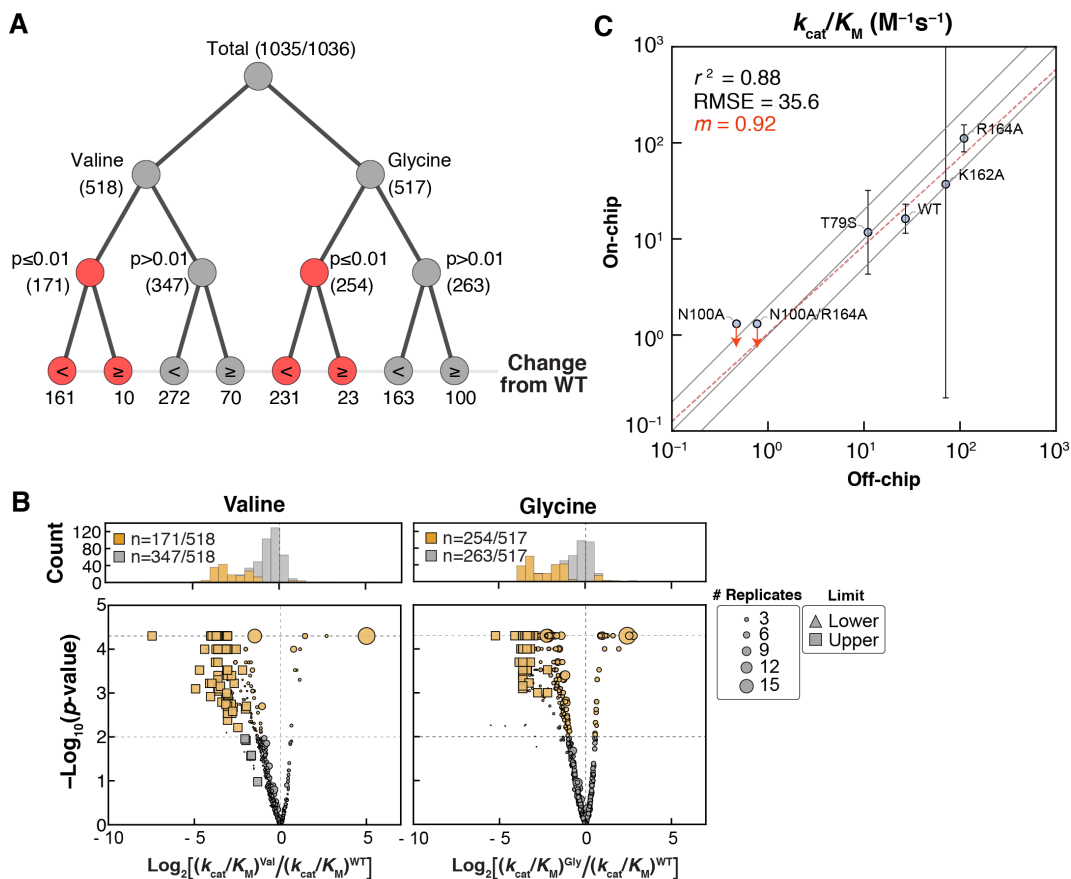


Fig. S49. Summary of measured k_{cat}/K_M for MecMUP across all mutants. (A) Tree diagram summarizing fraction of mutations with changes in activity from WT ($p < 0.01$) for valine and glycine mutant libraries. The p -values were determined from bootstrap hypothesis testing (see **Materials and Methods**). (B) Volcano plots showing effect size vs. p -value (as calculated from bootstrap hypothesis testing) for valine (left) and glycine (right) mutants; mutants with MecUP k_{cat}/K_M values of $p < 0.01$ are colored gold. (C) Comparison of on- (eGFP-tagged) and off-chip (strepII-tagged) MecMUP k_{cat}/K_M measurements for WT PafA and 5 additional mutants. The r^2 and RMSE are given with respect to a 1:1 line, and m corresponds to the slope of the best fit line (red). Error bars correspond to standard deviations (for measurements with > 2 replicates) and red arrows denote limits.

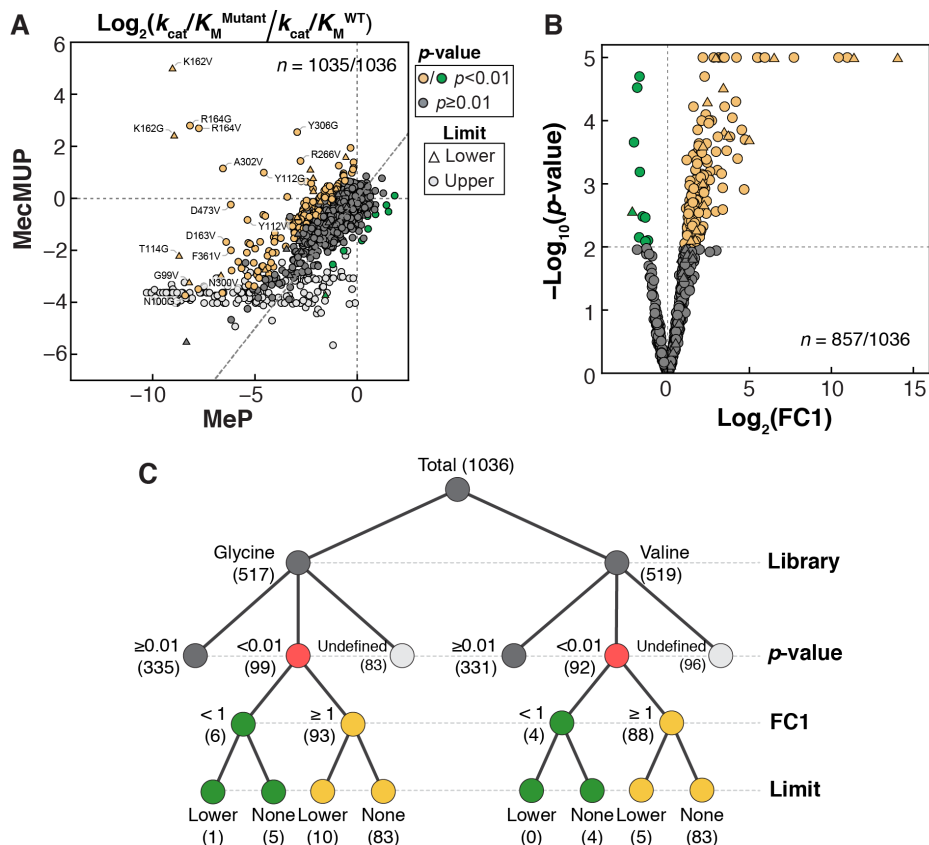


Fig. S50. Summary of Functional Component 1 (FC1) effects. (A) Mutational effects on k_{cat}/K_M of MecMUP and MeP hydrolysis. Mutants with $\text{FC1} > 1$ are colored yellow and those with $\text{FC1} < 1$ are colored green, if $p < 0.01$, determined from bootstrap hypothesis testing (see **Materials and Methods**). Upper FC1 limits (light gray points) arise for mutants whose MecMUP k_{cat}/K_M was below the dynamic range of the assay; lower FC1 limits are due to MeP k_{cat}/K_M measurements below the dynamic range (see **Materials and Methods**). (B) Volcano plot of FC1 effects. Upper limits are not shown in the figure as their FC1 effects cannot be determined (“Undefined” p -value). (C) Tree diagram summarizing fraction of mutations with FC1 effects ($p < 0.01$) and without FC1 effects, including upper limits (“Undefined” p -value) and lower limits as described in **Materials and Methods**.

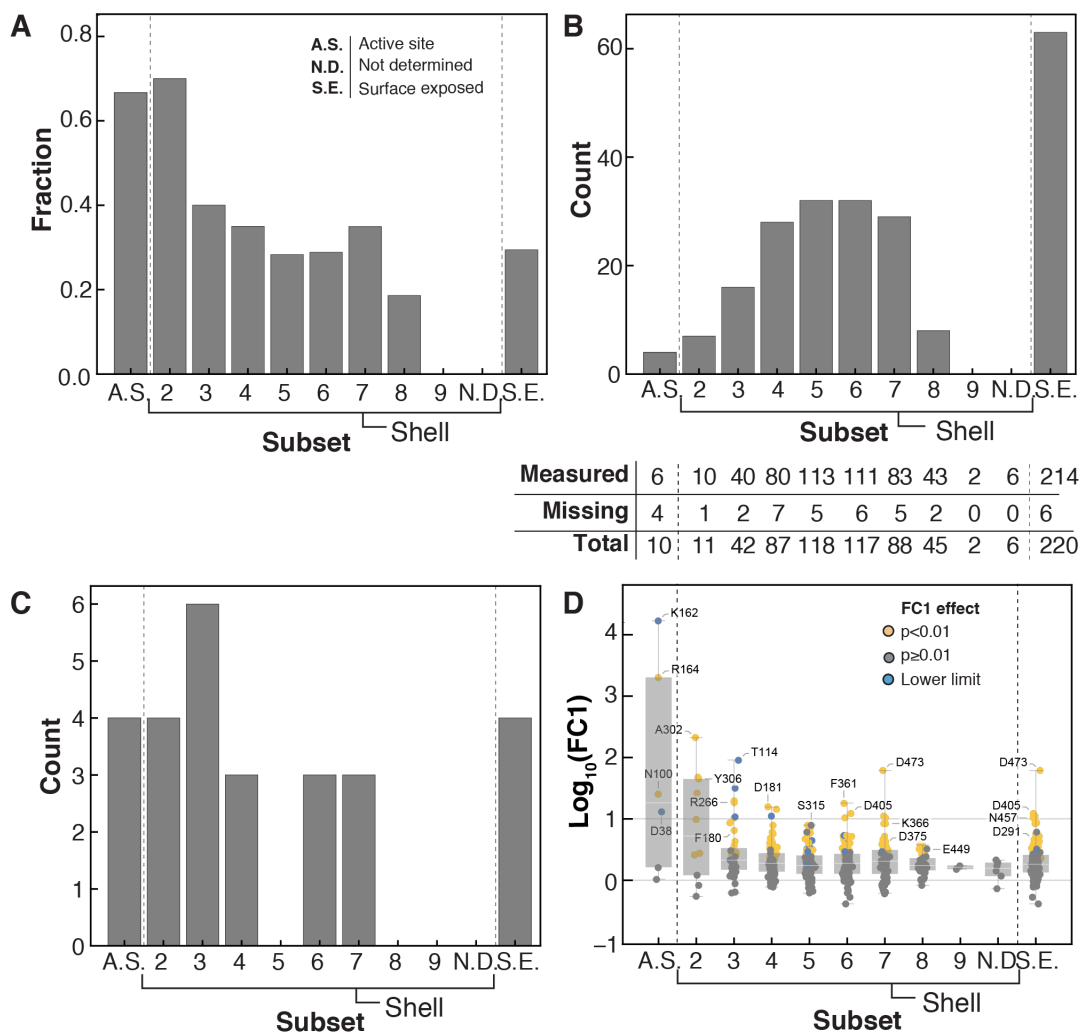
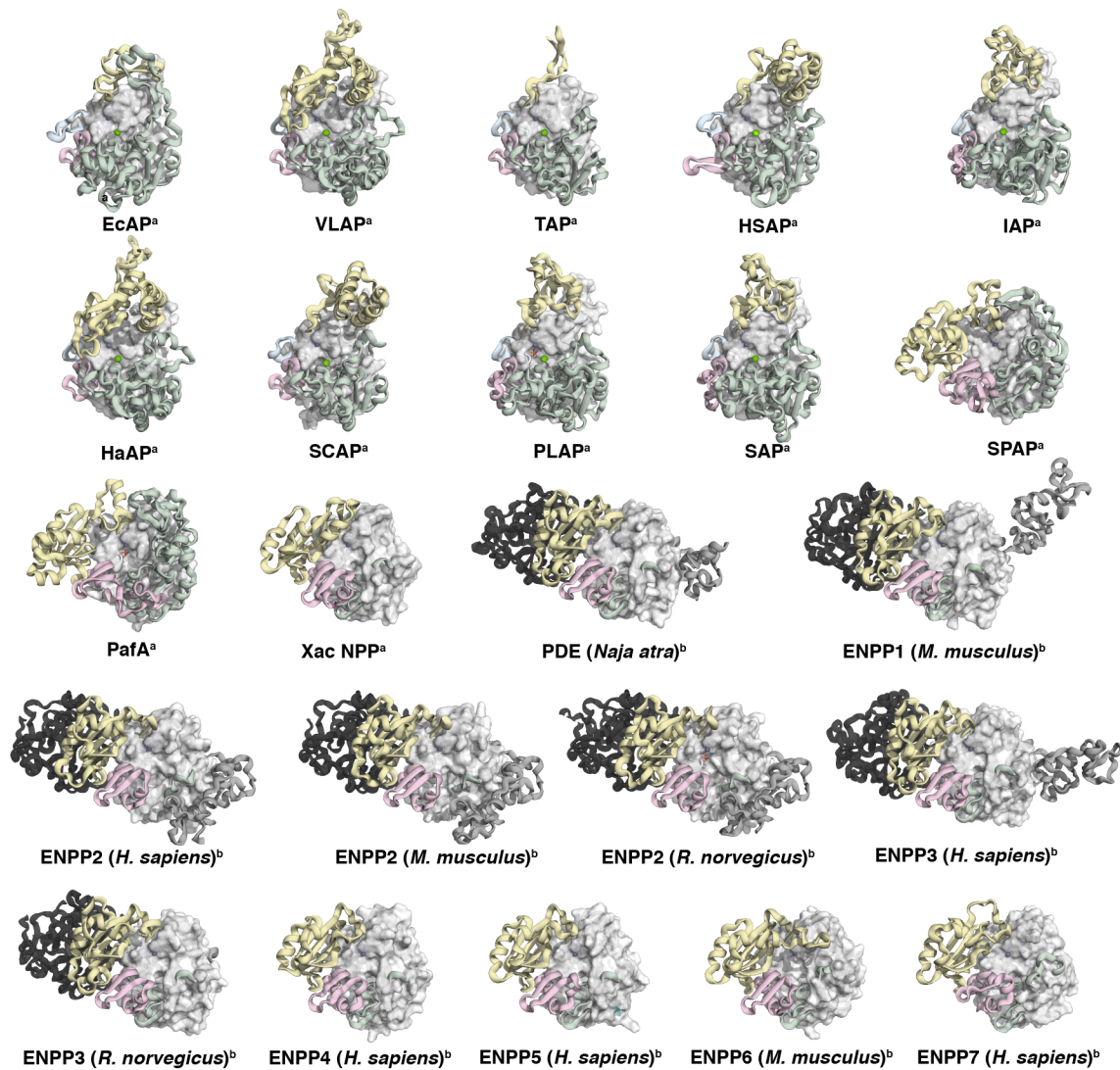


Fig. S51. Distributions of FC1 effects within the active site, each K162/R164 interaction shell, and the enzyme surface. (A) Fraction of measurable residues with FC1 effects within the active site (A.S.), each K162/R164 interaction shell, and for surface exposed (S.E.) residues (see **Materials and Methods**). (B) Number of residues with FC1 effects within the A.S., each K162/R164 interaction shell, and for surface-exposed residues. The table below gives the number of residues for which FC1 effects were not determined and the total number of residues within each subset. (C) Number of residues with >10-fold FC1 effects within the A.S., each K162/R164 interaction shell, and for surface-exposed residues. (D) Magnitude of FC1 effects within each shell for all residues that are either measurable or for which limits could be inferred. The horizontal lines denote 10-fold and WT-like FC1 effects, respectively.



Cognate reactivity

^aMonoesterase

^bDiesterase

Structural Domains

Color	Name	PafA Range	Color	Name	PafA Range
Gray	Auxiliary N-term	N-terminus-27	Yellow	Auxiliary 4	356-485
Light Blue	Auxiliary 1	Not Present	White	Rossmann Core	Remainder
Pink	Auxiliary 2	91-137	Black	Auxiliary C-term	Not Present
Light Green	Auxiliary 3	159-275			

Fig. S52. Core and auxiliary domain assignments of unique structurally-characterized alkaline phosphatase (AP) superfamily phosphate monoesterases and diesterases (*cf.* **Table S12**). The Rossmann core is shown as a gray surface and the auxiliary domains are shown as cartoons and colored.

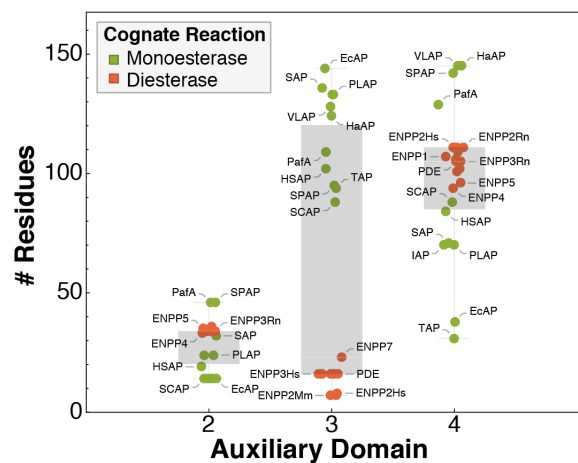


Fig. S53. Lengths of auxiliary domains 2–4 for AP superfamily monoesterase and diesterase orthologues.

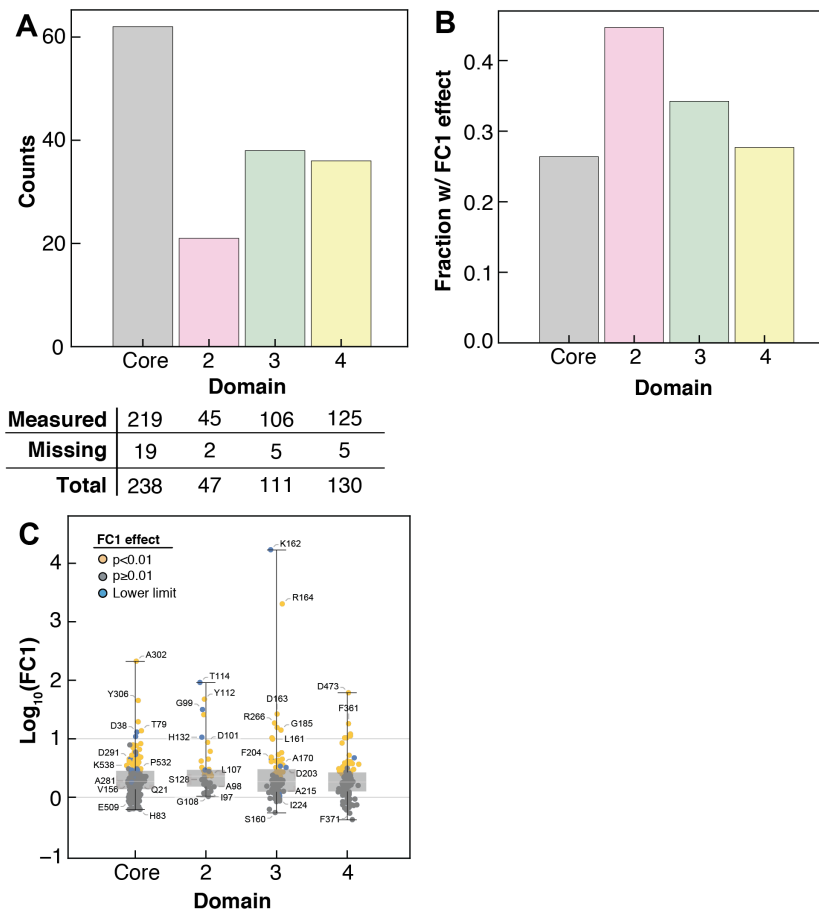


Fig. S54. Distributions of FC1 effects within the Rossmann fold core and auxiliary domains. (A) Number of residues with FC1 effects ($p < 0.01$, Val or Gly mutant) within Rossmann core and auxiliary domains. (B) Fraction of residues with FC1 effects within Rossmann core and auxiliary domains. (C) Magnitude of FC1 effects within the Rossmann core and each auxiliary domain, for all residues either measurable or for which limits could be inferred. The horizontal lines denote 10-fold and WT-like FC1 effects, respectively.

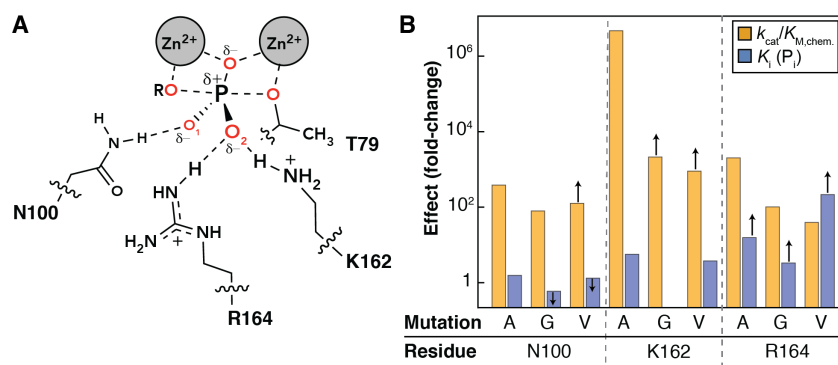


Fig. S55. Catalytic and $K_i(P_i)$ effects for mutations of residues making active site O1 and O2 contacts. (A) Active site schematic of PafA showing the three active site residues making contacts to the phosphoryl O1 and O2 oxygen atoms, the T79 nucleophile, and the catalytic Zn^{2+} ions. (B) Measured k_{cat}/K_M of MeP hydrolysis (assuming full catalytic effect of valine and glycine mutations, as established for the alanine mutants) and $K_i(P_i)$ effects for mutations to the O1- and O2-contacting residues. Effects are reported as fold-changes in k_{cat}/K_M of MeP hydrolysis and $K_i(P_i)$ relative to the wild-type values. To facilitate co-plotting, values >1 correspond to a deleterious effect on k_{cat}/K_M and an increase in $K_i(P_i)$. The k_{cat}/K_M and $K_i(P_i)$ values for the alanine mutants were taken from ref. (16) as the on-chip measurements of K162A and R164A k_{cat}/K_M were upper limits. Up and down arrows denote lower and upper limits, respectively.

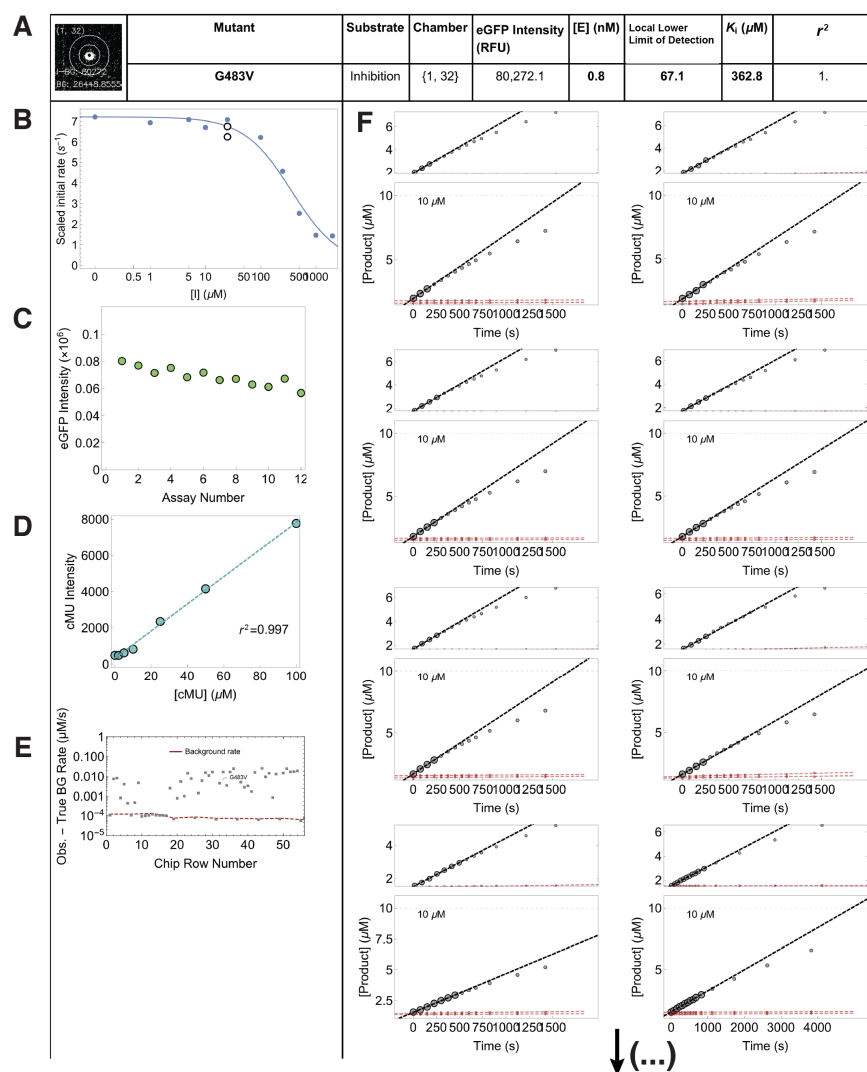


Fig. S56. Example data report for a single chamber after an HT-MEK experiment measuring hydrolysis of cMUP in the presence of increasing P_i concentrations to quantify $K_i(P_i)$ (12 assays, with the first 6 shown in this example). Each experiment returns 1,568 unique per-chamber reports containing: (A) Mutant identity, with image of immobilized enzyme in the eGFP channel, experimental parameters (chamber column and row, eGFP intensity, enzyme concentration, the rate compared to the local background (LLoD), K_i and r^2); (B) Competitive inhibition fits to scaled initial rates (blue) with initial rates from replicate assays (white); (C) Measured eGFP intensity for each assay; (D) Per-chamber product fluorescence standard curve and fit r^2 ; (E) Comparison of fitted rates (gray points) with the interpolated local lower limit of detection (LLoD, red dashed line) within this chamber's full column; (F) Full reaction progress curves (lower panels) and expanded plots (upper panels) for each P_i concentration, with fitted initial rates shown as dashed black lines. Large gray points were used to determine the linear fit; small gray points were measured but outside the linear region and not used to fit initial rates. Red points and lines denote the progress curves and linear fits from the nearest upstream and downstream background chambers used to determine the local background.

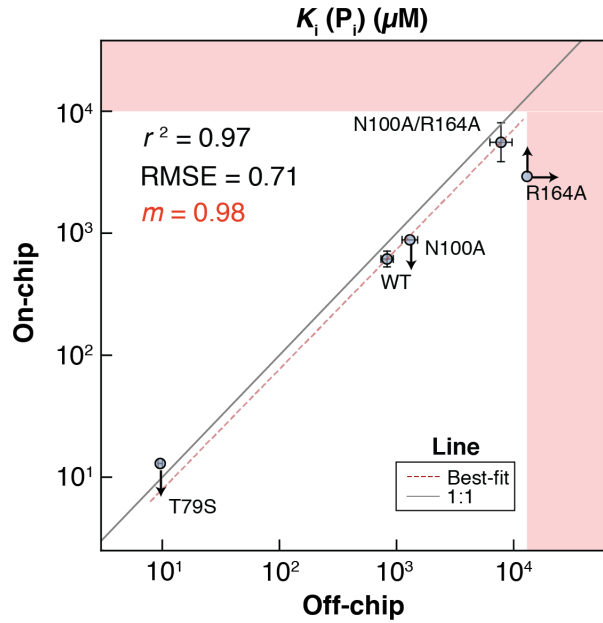


Fig. S57. Comparison of on- (eGFP-tagged) and off-chip (strepII-tagged) $K_i(P_i)$ measurements for WT PafA and 4 active site mutants. Reported r^2 and RMSE (\log_{10} -transformed values) are given for the 1:1 line, and m corresponds to the slope of the best fit line fitted to the mutants for which K_i for P_i was not a limit (WT and N100A/R164A). Pink shaded regions denote the upper limits of dynamic range for K_i for P_i , determined based on the highest $[P_i]$ concentrations used in the assays; arrows denote upper and lower limits in $K_i(P_i)$. Vertical error bars denote standard deviations of on-chip measurements; horizontal error bars are from ref. (16).

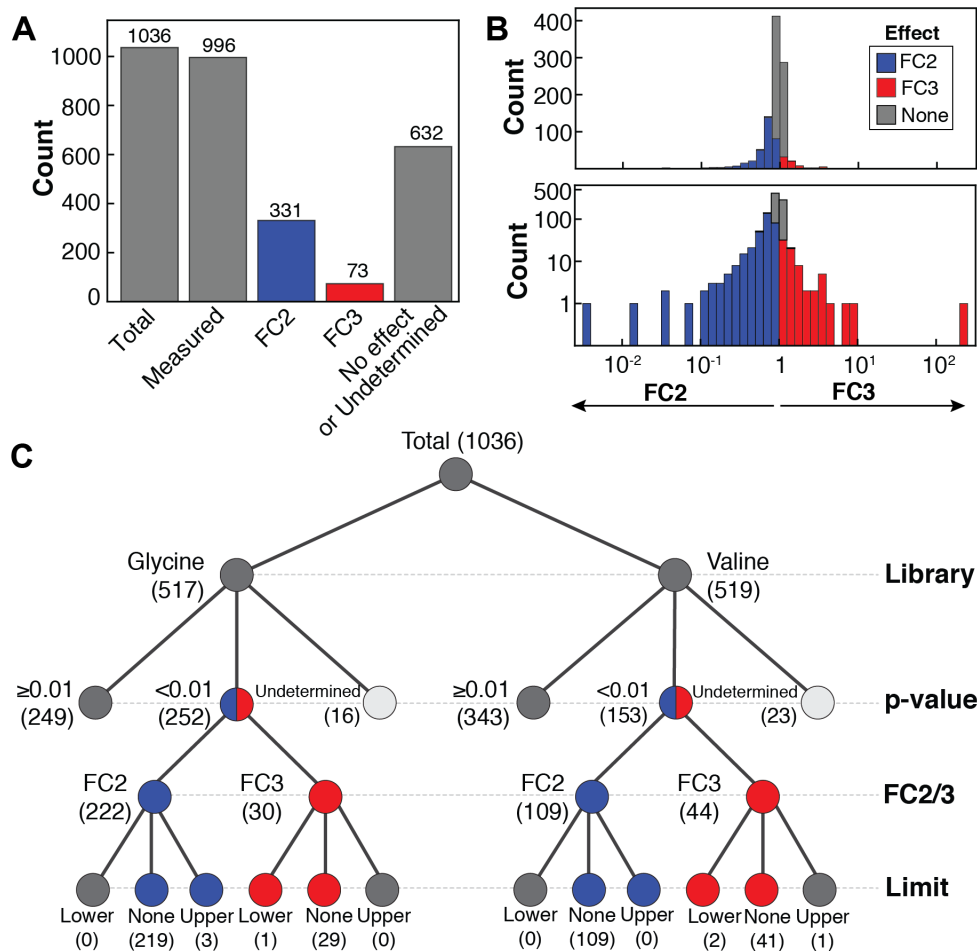


Fig. S58. Functional Component (FC) 2 and 3 effects within the glycine and valine scanning libraries. (A) Number of residues found to have FC2 or FC3 effects ($p < 0.01$). “No effect or Undetermined” mutants also includes one mutant with an upper limit in FC3 effect (considered “Undefined”). (B) Distribution of measured FC2 and FC3 values, with counts displayed on a linear (top) and logarithmic scale (bottom). (C) Tree diagram summarizing the number of mutations with FC2 or FC3 effects ($p < 0.01$) for the glycine and valine mutant libraries, including upper and lower limits as described in **Materials and Methods**. Mutants whose FC2 and FC3 values are lower and upper limits, respectively, cannot be distinguished from WT due to the direction of the limit.

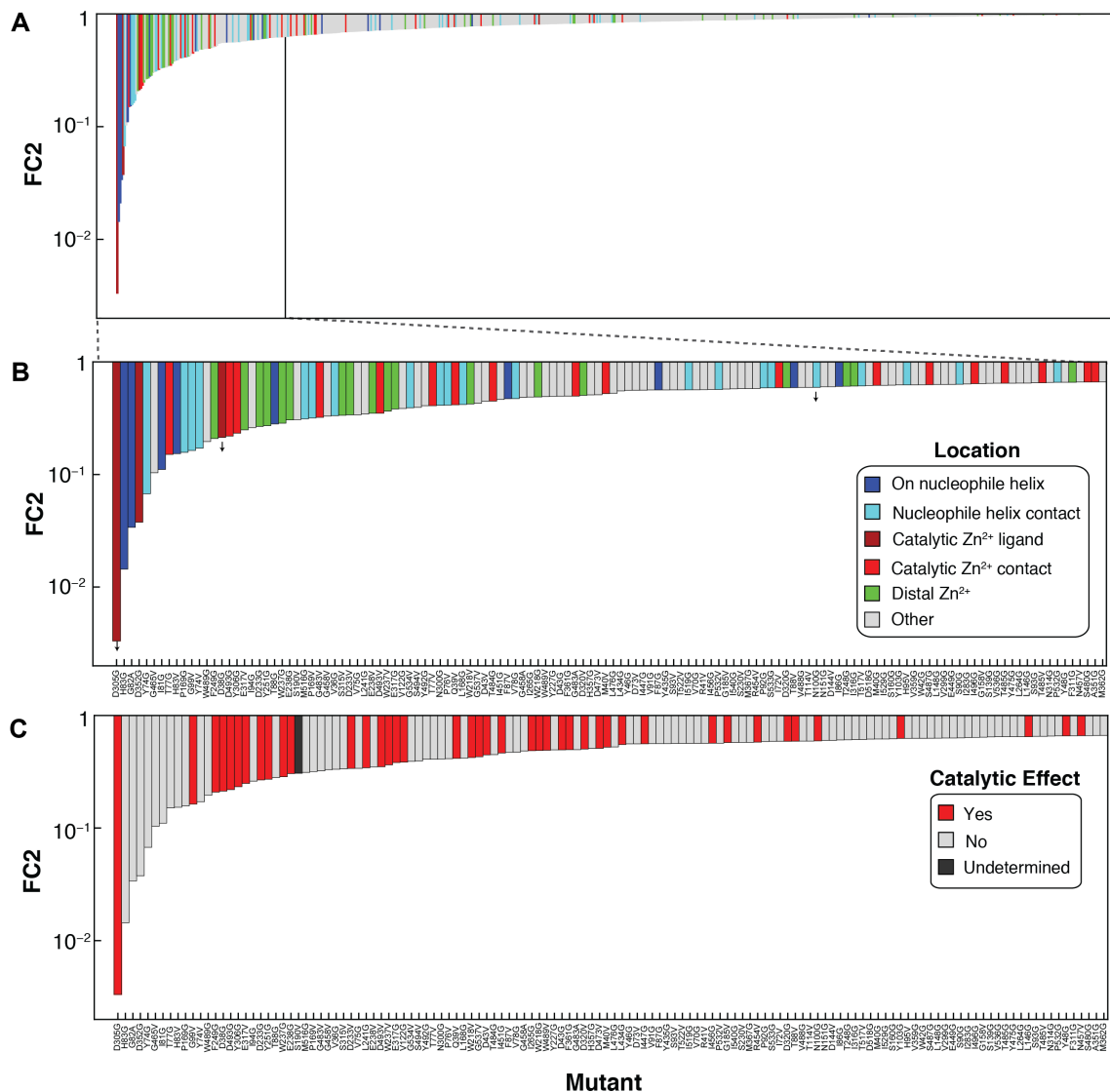


Fig. S59. Structural location and magnitudes of the largest FC2 effects. (A) Bar chart of all FC2 effects ($K_i^{\text{mutant}} < K_i^{\text{WT}}$ for P_i), sorted by magnitude and colored by their location in PafA. Arrows denote upper limits of FC2 measurements. (B) Same as panel A, but for the mutants with FC2 effects greater than 1.5-fold from wild-type. (C) Same as panel B, with bars colored by the presence of a catalytic effect ($k_{\text{cat}}/K_M^{\text{chem}}$) ($p < 0.05$).

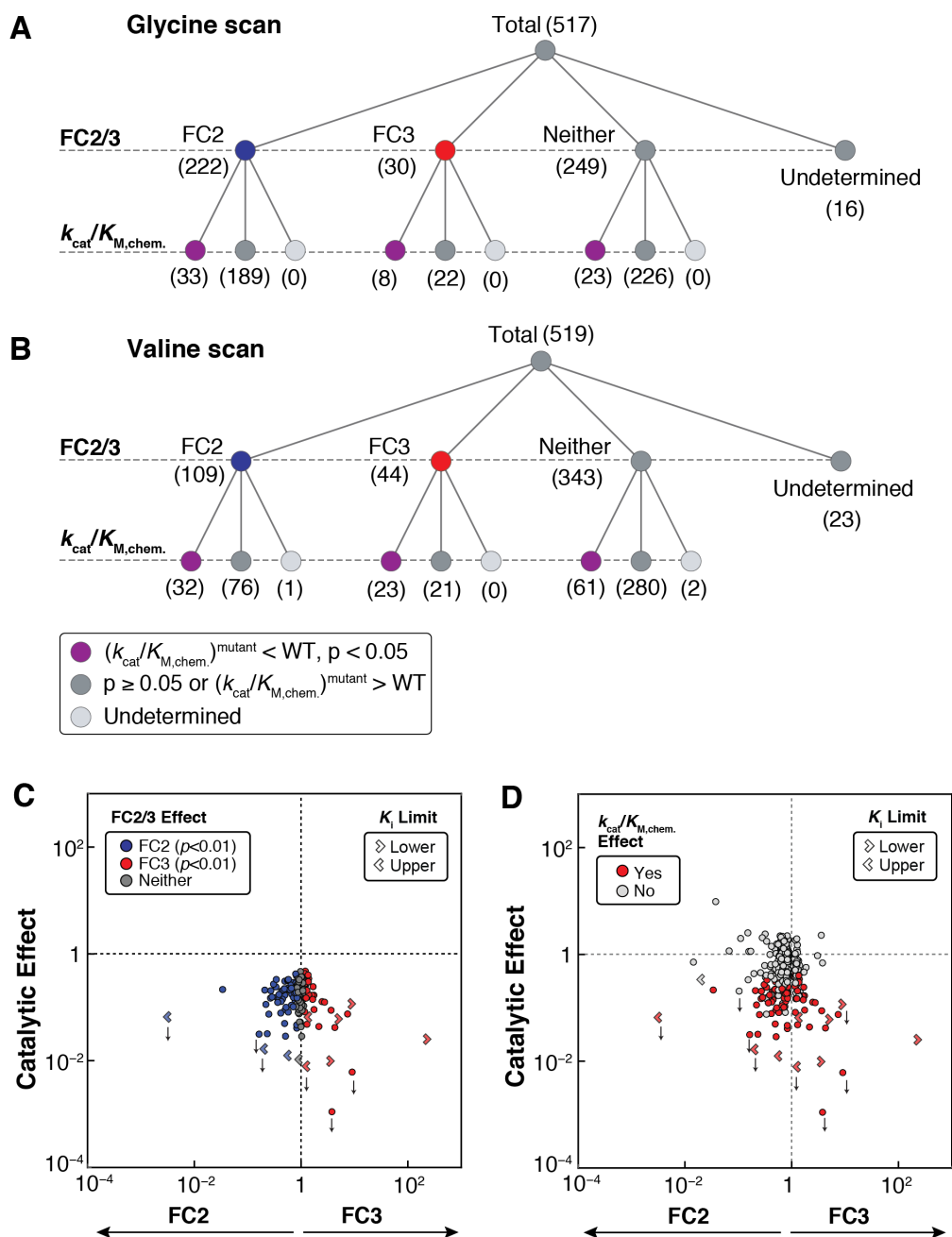


Fig. S60. Intersections of FC2/3 and catalytic (k_{cat}/K_M^{chem}) effects. (A) Tree with counts of residues with catalytic and FC2/3 effects, for the glycine scanning library. (B) Tree with counts of residues with catalytic and FC2/3 effects, for the valine scanning library. (C) Scatter plot of catalytic and FC2/3 effects for mutants with catalytic effects ($p < 0.05$ and $(k_{cat}/K_M^{chem})_{mutant} < (k_{cat}/K_M^{chem})_{WT}$), colored by FC2/3 effects. (D) Scatter plot of catalytic and FC2/3 for mutants with FC2/3 effects ($p < 0.01$), colored by catalytic effect.

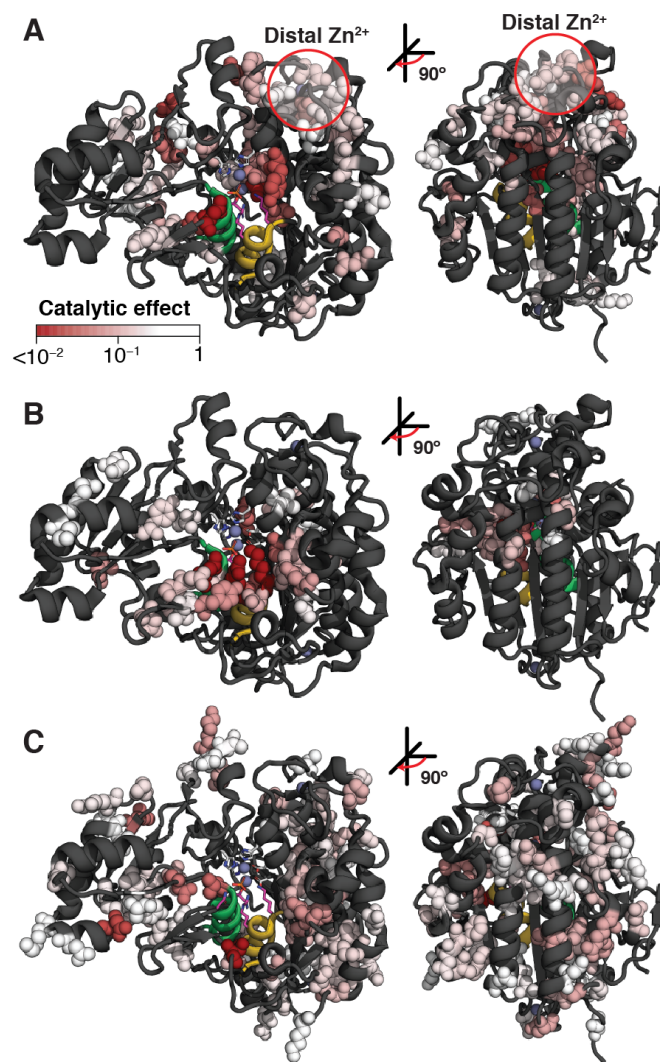


Fig. S61. Catalytic effects ($k_{\text{cat}}/K_{\text{M}}^{\text{chem}}$, fold-change relative to WT) for residues with FC2 or FC3 effects shown as spheres on the PafA structure and colored by the magnitude of the catalytic effect. (A) Positions (55 residues; 65 mutants) with FC2 and catalytic effects ($p < 0.01$). (B) Positions (27 positions; 31 mutants) with FC3 and catalytic effects ($p < 0.01$). (C) Positions (83 residues; 84 mutants) with catalytic effects ($p < 0.01$) and no FC2/3 effects ($p \geq 0.01$).

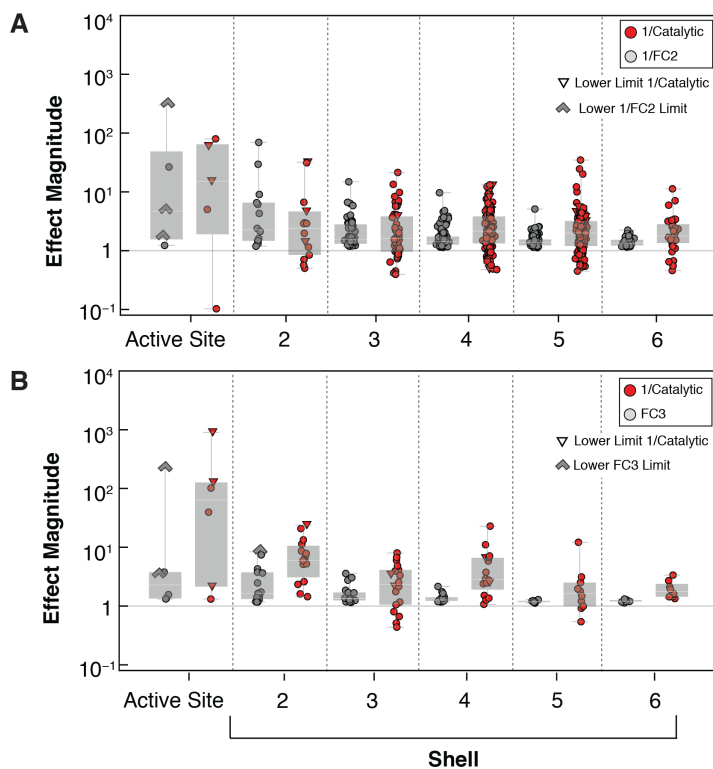


Fig. S62. Comparison of the relative magnitudes of catalytic and FC2/3 effects as a function of active site interaction shell. (A) Relative magnitude of FC2 (gray points) and catalytic ($k_{\text{cat}}/K_{\text{M}}^{\text{chem}}$; red points) effects for residues with FC2 effects ($p < 0.01$). (B) Relative magnitude of FC3 (gray points) and catalytic ($k_{\text{cat}}/K_{\text{M}}^{\text{chem}}$; red points) effects for residues with FC3 effects ($p < 0.01$).

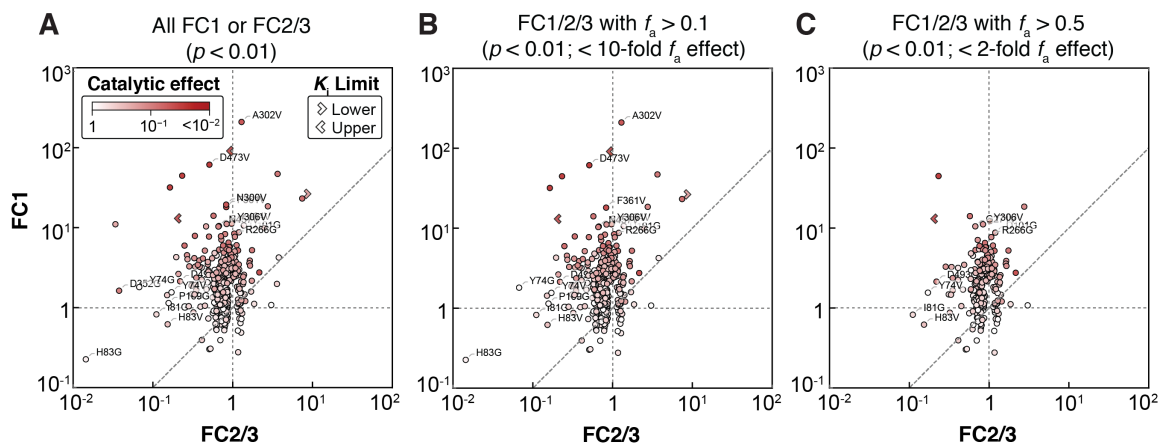


Fig. S63. Relative magnitudes of effects of mutations of FC1, FC2, FC3, catalysis ($k_{\text{cat}}/K_{\text{M}}^{\text{chem}}$), and fraction active (f_a). (A) Scatter plot showing FC1 effects vs. FC2/3 effects for all mutants for which all FCs were measurable, colored by $k_{\text{cat}}/K_{\text{M}}^{\text{chem}}$. (B) Subset of mutations with f_a effects < 10 -fold from WT. (C) Subset of mutations with f_a effects < 2 -fold from WT.

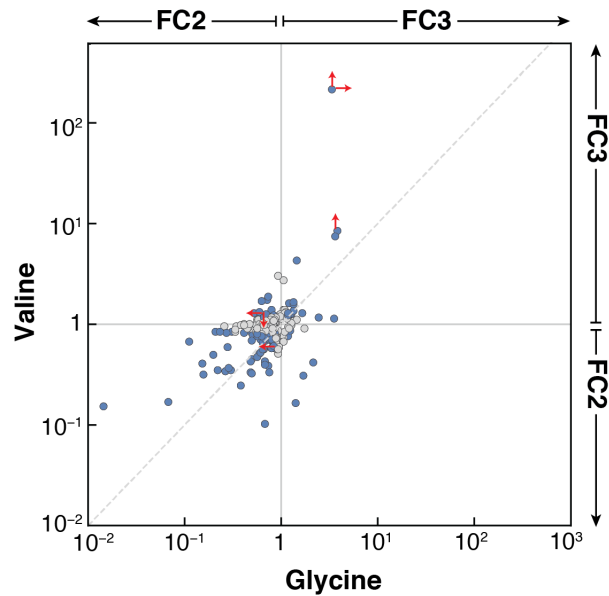


Fig. S64. Comparison of FC2/3 effects for valine or glycine substitutions. Residues with an FC2/3 effect ($p < 0.01$) when mutated to either valine or glycine are shown in gray, and those with FC2/3 effects for both substitutions are shown in blue. Upper and lower limits are denoted by red arrows.

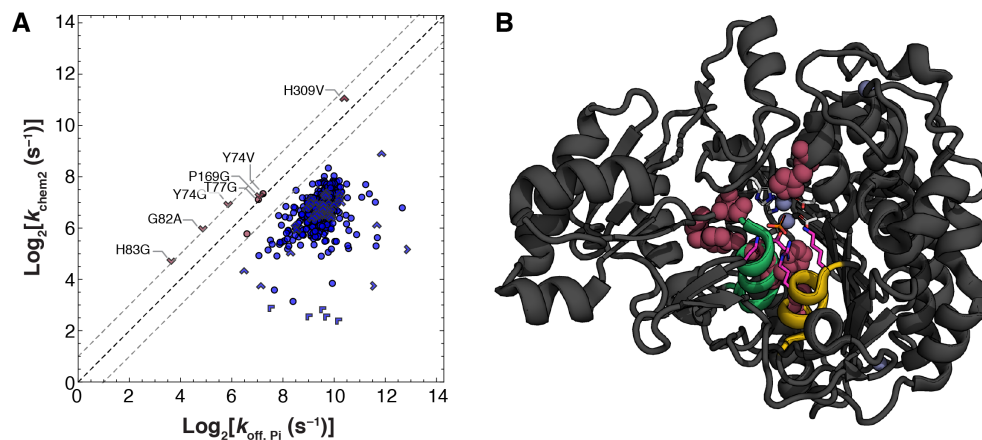


Fig. S65. Mutations with phospho-enzyme hydrolysis likely to be partially or fully rate limited by phosphate release. (A) Scatter plot of $k_{\text{chem},2}$ vs. $k_{\text{off},\text{P}_i}$ for Val and Gly scanning mutants. Limits are denoted by chevrons pointing in the direction of or quadrant containing the point. Mutants partially or fully rate-limited by P_i -release are highlighted (burgundy points, $k_{\text{off},\text{P}_i} < 2 \times k_{\text{chem},2}$). (B) Positions of mutants partially or fully rate-limited by P_i -release upon mutation as spheres on the PafA structure.

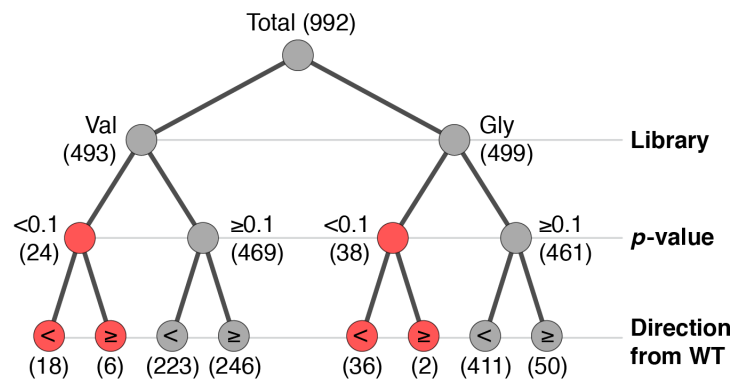


Fig. S66. Counts of mutational effects on the rate of phospho-enzyme intermediate hydrolysis ($k_{\text{chem},2}$).

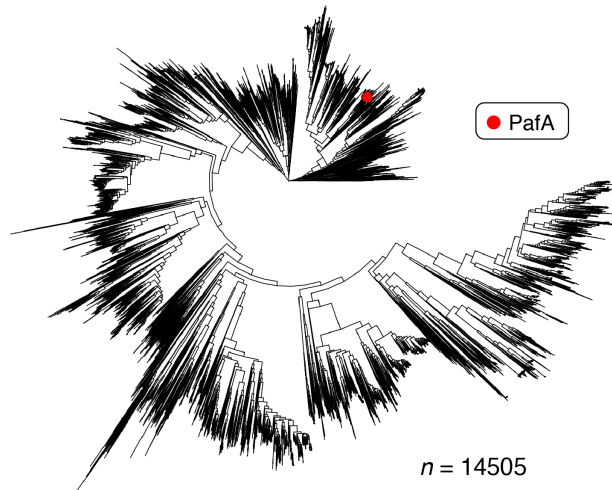


Fig. S67. A maximum-likelihood tree inferred from a multiple sequence alignment of 14,505 metagenomic and public database PafA-like AP superfamily members.

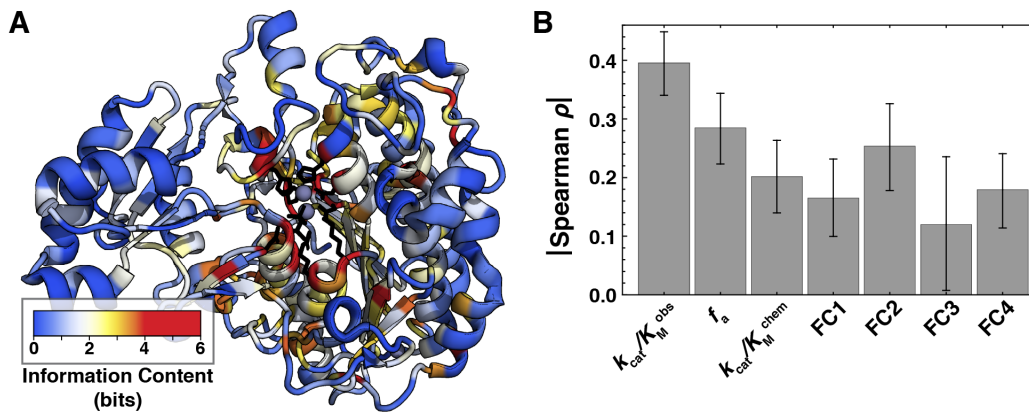


Fig. S68. Spatial pattern of PafA conservation and ability of conservation to predict mutational effects (A) Conservation of residues across a broad metagenomic alignment of PafA-like AP superfamily members. (B) Spearman's rank correlation coefficients for comparisons of functional parameters against residue conservation (information content). Error bars denote bootstrap 95% CIs.

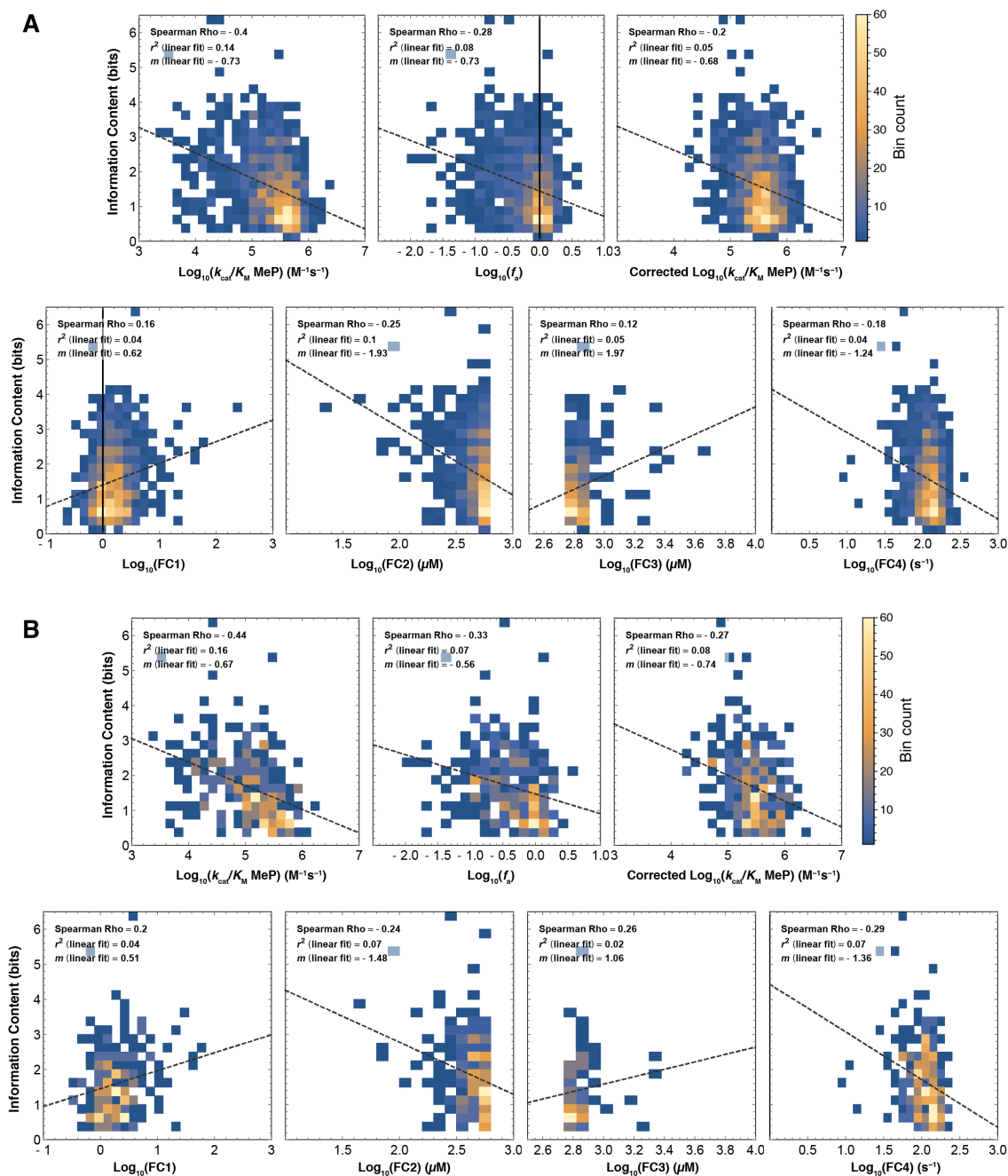


Fig. S69. Correlations between phylogenetic conservation and HT-MEK measured parameters and FCs. (A) Correlations (Spearman's rank, ρ ; linear fit r^2) between conservation and $k_{\text{cat}}/K_M^{\text{obs}}$ MeP, f_a , $k_{\text{cat}}/K_M^{\text{chem}}$ MeP, and FCs 1–4 for all valine and glycine mutants. (B) Correlations (Spearman rank, ρ ; linear fit r^2) between conservation and $k_{\text{cat}}/K_M^{\text{obs}}$ MeP, f_a , $k_{\text{cat}}/K_M^{\text{chem}}$ MeP, and measured FCs 1–4 only for mutations likely to dramatically alter biochemical properties at a given position (with a BLOSUM62 score of substitution <-2 when considering the difference between the WT and mutant residue identities).

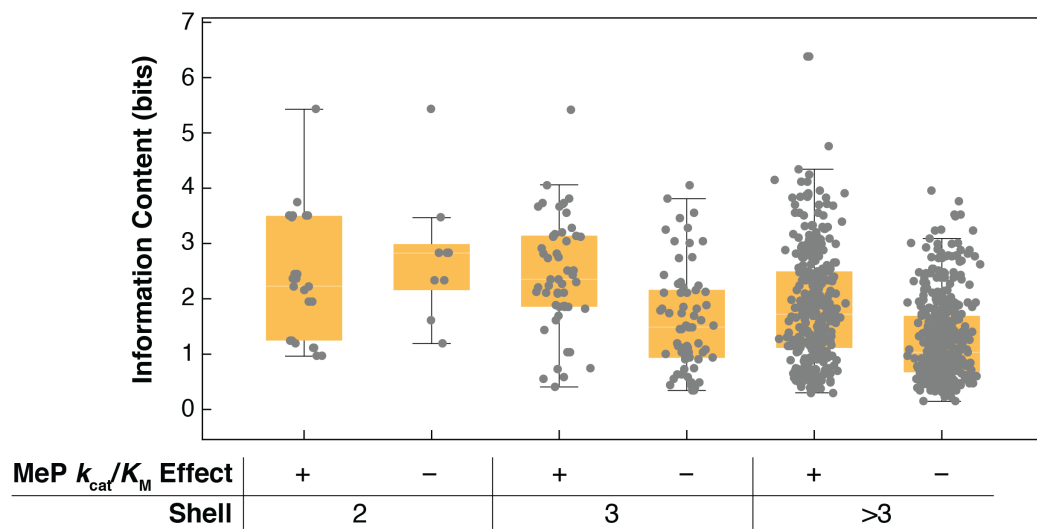


Fig. S70. Conservation is not sufficient to accurately predict effects of particular mutations near the active site. Conservation (Information Content) of residues with and without significant observed MeP (k_{cat}/K_M) effects when mutated for residues in the second and third interaction shells around the active site residues K162 and R164, and in all other shells.

Tables S1 to S17

PafA Variant StrepII-tagged expressed <i>in vivo</i>	Substrate	Parameter		
		k_{cat} (s^{-1})	K_M (μM)	k_{cat}/K_M ($\text{M}^{-1}\text{s}^{-1}$)
WT	pNPP	3.0×10^2	190	1.6×10^6
	cMUP	3.2×10^2	110	3.0×10^6
R164A	pNPP	6.6	51	1.3×10^5
	cMUP	4.7	32	1.4×10^5
T79S	pNPP	1.8	2.9	6.3×10^5
	cMUP	9.7×10^{-1}	1.0	9.2×10^5
N100A	pNPP	3.9×10^{-1}	0.51	7.6×10^5
	cMUP	9.9×10^{-1}	0.75	9.0×10^5
N100A/R164A	pNPP	–	–	–
	cMUP	9.2×10^{-1}	190	5.0×10^3
K162A	pNPP	3.0×10^{-2}	230	1.3×10^2
	cMUP	2.8×10^{-2}	89	2.8×10^2

Table S1. Measured Michaelis-Menten parameters for hydrolysis of pNPP and cMUP by PafA active site mutants. All measurements were performed with the Strep-tag bearing (non eGFP-fusion) constructs expressed in *E. coli*. pNPP hydrolysis parameters are reproduced from (16) and cMUP parameter estimates are means of two or more replicates and were measured herein (see **Materials and Methods**).

			Chambers		Unique Variants			
Tier	Print	Library	Empty & T79G	All	Val	Gly	A.S.	Median # reps
-	A.S.	A.S.	1248	7	0	1	6	50
I	Val I	Val, A.S.	68	532	519	7	6	2
I	Val II	Val, A.S.	126	506	497	3	6	2
I	Gly	Gly, A.S.	298	523	0	517	6	2
II	Slow	All	350	211	65	140	6	4
II	Slow MeP	All	768	43	32	6	5	16
III	Slowest	All	1028	61	26	30	5	8
All	-	All	-	1042	519	517	6	-

Table S2. Summary of tiered measurement strategy. Skipped chambers were those lacking printed plasmid, and “A.S.” denotes Active Site.

Substrate		PafA Variant		Michaelis-Menten Parameters					
				off-chip (<i>E. coli</i> expressed, StrepII-tagged)			on-chip (IVTT expressed, eGFP tagged)		
				k_{cat} (s^{-1})	K_M (μM)	k_{cat}/K_M ($M^{-1}s^{-1}$)	k_{cat} (s^{-1})	K_M (μM)	k_{cat}/K_M ($M^{-1}s^{-1}$)
cMUP ^a	WT	3.2×10^2	1.1×10^2	3.0×10^6	1.2×10^2	102	1.2×10^6		
	R164A	4.7	32	1.4×10^5	3.3	27	1.2×10^5		
	T79S	0.97	1.0	9.2×10^5	0.7	1.4	5.0×10^5		
	N100A	0.99	0.75	9.0×10^5	0.32	2.0	1.6×10^5		
	N100A/R164A	0.92	1.9×10^2	5.0×10^3	0.36	1.5×10^2	2.5×10^3		
	K162A	2.8×10^{-2}	89	2.8×10^2	1.8×10^{-2}	55	3.4×10^2		
MeP ^b	WT	–	–	1.9×10^6	–	–	6.1×10^5		
	R164A	–	–	3.8×10^2	–	–	$\leq 7.2 \times 10^3$		
	T79S	–	–	7.9×10^4	–	–	3.2×10^4		
	N100A	–	–	3.3×10^3	–	–	2.2×10^3		
	N100A/R164A	–	–	30	–	–	$\leq 7.0 \times 10^3$		
	K162A	–	–	–	–	–	$\leq 1.2 \times 10^4$		
MecMUP	WT	–	–	32	–	–	16		
	R164A	–	–	1.1×10^2	–	–	1.1×10^2		
	T79S	–	–	12	–	–	≥ 12		
	N100A	–	–	0.50	–	–	≤ 1.3		
	N100A/R164A	–	–	0.77	–	–	≤ 1.3		
	K162A	–	–	73	–	–	37		

Inhibitor		Competitive Inhibition Constant K_i (μM)	
		off-chip (<i>E. coli</i> expressed, StrepII-tagged)	on-chip (IVTT expressed, eGFP tagged)
P _i ^c	WT	8.3×10^2	6.1×10^2
	R164A	$> 13 \times 10^3$	$\geq 2.9 \times 10^3$
	T79S	9.6	≤ 13
	N100A	1.3×10^3	$\leq 8.8 \times 10^2$
	N100A/R164A	7.8×10^3	5.6×10^3
	K162A	4.7×10^3	–

^aOn-chip cMUP estimates were from the Active Site experiment for all variants except K162A, an estimate for which was obtained from Tiers I–III. ^bMeP turnover measurements off-chip were made using the Phosphate Sensor under low ionic strength conditions, as performed on-chip. ^cOff-chip K_i ; P_i parameters are those reported previously (16), except for N100A/R164A, which was measured herein as described previously (16).

Table S3. Comparisons of PafA Active Site variant activities and inhibition off- and on-chip. (A) Michaelis-Menten parameters for Active Site variant hydrolysis of phosphate monoesters cMUP and MeP, and phosphate diester MecMUP. Unmeasured or un-resolvable (under substrate concentrations used) parameters are denoted by dashes, and limits are denoted by inequalities. (B) Competitive inhibition constants of inorganic phosphate for WT and Active Site PafA variants. On-chip inhibition of K162A was un-resolvable, denoted by the dash. Limits are denoted by the inequalities, with lower limits arising on-chip from upper limits in K_M .

Mutant	k_{cat}/K_M ($M^{-1}s^{-1}$)		k_{rel} (off/on-chip)
	pNPP, off-chip	cMUP, on-chip	
WT	2.20×10^6	1.42×10^6	1.5
Y52G	1.47×10^6	8.39×10^5	1.7
K58V	1.86×10^6	1.08×10^6	1.7
A80V	5.52×10^5	2.02×10^5	2.7
F87G	1.77×10^6	1.99×10^6	0.9
T88V	7.01×10^5	7.51×10^5	0.9
S90V	2.90×10^5	2.65×10^5	1.1
G108A	1.83×10^6	1.33×10^6	1.4
G130V	6.40×10^5	7.68×10^5	0.8
R164A	3.30×10^5	2.64×10^5	1.3
T189G	4.80×10^5	2.83×10^5	1.7
S190G	2.80×10^5	3.97×10^5	0.7
P198V	2.27×10^6	1.86×10^6	1.2
R266V	2.10×10^6	1.63×10^6	1.3
Y306V	1.90×10^6	8.69×10^5	2.2
A330G	2.43×10^6	2.33×10^6	1.0
L349G	5.89×10^5	1.13×10^5	5.2
R463V	1.44×10^6	4.51×10^5	3.2
L499G	9.71×10^5	1.12×10^6	0.9

Table S4. Library variants (17 Val and Gly, 1 Active Site, and the WT) expressed *in vitro* and characterized off-chip to test for chip-specific expression effects (all constructs were eGFP-tagged).

Variant	On-chip k_{cat}/K_M ($M^{-1}s^{-1}$)		$(k_{\text{cat}}/K_M^{\text{MeP, WT}})/(k_{\text{cat}}/K_M^{\text{MeP, variant}})$	$(k_{\text{cat}}/K_M^{37^\circ\text{C}})/(k_{\text{cat}}/K_M^{23^\circ\text{C}})$ (WT-normalized)	
	cMUP	MeP		On-chip	Off-chip
F87G	1.99×10^6	6.65×10^5	0.9	4.7	2.6
A330G	2.33×10^6	4.28×10^5	1.4	3.1	1.7
G108A	1.33×10^6	2.58×10^5	2.4	2.8	1.9
K58V	1.08×10^6	2.14×10^5	2.9	5.9	2.0
L499G	1.12×10^6	1.34×10^5	4.6	30	8.5
Y52G	8.39×10^5	1.19×10^5	5.1	20	6.5
F180V	1.91×10^6	1.00×10^5	6.1	0.9	2.5
T304V	1.19×10^5	9.96×10^4	6.1	1.8	2.1
N173V	3.78×10^5	9.94×10^4	6.1	1.7	2.2
R266V	1.63×10^6	8.92×10^4	6.8	1.6	0.8
S90V	2.65×10^5	8.48×10^4	7.2	3.6	4.2
S190G	3.97×10^5	7.97×10^4	7.7	2.1	2.8
T189G	2.83×10^5	7.01×10^4	8.7	7.4	3.0
D182G	1.48×10^6	5.92×10^4	10.3	2.4	3.8
Y306V	8.69×10^5	5.70×10^4	10.7	4.0	1.2
V433G	1.56×10^5	3.42×10^4	17.9	9.7	1.5
Y103G	2.82×10^5	2.61×10^4	23	14	4.9
W218G	2.17×10^5	2.09×10^4	29	4.3	1.9
A80V	2.02×10^5	1.48×10^4	41	1.2	3.2
R164A	2.64×10^5	7.16×10^3	85	0.8	0.5
WT	1.42×10^6	6.10×10^5	1	1	1

Table S5. Library PafA variants (19 Val and Gly, 1 Active Site, and WT) characterized off chip and expressed *in vivo* to test for expression-temperature-dependent activity changes (all constructs were eGFP-tagged).

	Expression	<i>in vivo</i> ^a						<i>in vitro</i>		
	eGFP Tag	+			-			+		
	Temperature (°C)	23	37	-	23	37	-	23	37	-
	Parameter	k_{cat}/K_M ($M^{-1} s^{-1}$)		Temp. effect	v_i (100 μ M) / [E] (s^{-1})		Temp. effect	k_{cat}/K_M ($M^{-1} s^{-1}$)		Temp. effect
Variant	Y103G	3.9×10^5	6.7×10^4	5	2.5×10^2	0.96	3.0×10^2	4.0×10^4	$< 1.5 \times 10^3$	> 13
	WT	3.1×10^6	1.8×10^6	1	2.3×10^2	2.6×10^2	1	4.1×10^5	2.1×10^6	1

^a*In vivo* activity measurements were made using pNPP, a convenient chromogenic substrate, diffusion-limited like cMUP (see **Materials and Methods**).

Table S6. Comparison of activities and temperature effects (ratio of WT-normalized activities at 23 °C and 37 °C., see **Eq. 9**) *in vivo* vs. *in vitro* and with and without an eGFP tag.

Technique	PafA Variant	Expression Temperature (°C)	% Content	
			α -helix	β -Sheet
X-ray Crystallography (RCSB PDB ID)	WT (5TJ3)	30	34	16
	pruned ^a (5TOO)	23	34	16
Circular Dichroism	WT	23	32	14
		37	31	14
	Y103G	23	32	15
		37	20	17

^a“Pruned” PafA bears the following mutations: T79S, N100A, K162A, and R164A (116).

Table S7. Secondary structure content of PafA variants calculated from previously published crystallographic data and circular dichroism (CD) data collected herein. Content was calculated for CD data with the K2D3 web server and for crystallographic data with DSSP (117, 118).

Distance from active site (Å)	Catalytic Effect ($k_{\text{cat}}/K_{\text{M}}^{\text{MeP, chem. mutant}}/k_{\text{cat}}/K_{\text{M}}^{\text{MeP, WT}}$)					
	$p < 0.05$			$p \geq 0.05$	Undefined p -value	All p -values
	< 0.1	≥ 0.1 & < 0.2	≥ 0.2 & < 1	Any	Undefined	All
0–5	12	13	8	68	9	110
5–10	6	13	17	140	4	180
10–15	6	20	25	225	10	286
15–20	5	8	26	201	4	244
20–25	0	2	9	107	3	121
25–30	1	0	4	26	1	32
30–35	0	0	1	9	0	10
35–40	0	0	0	2	0	2
N.D. ^a	0	0	0	12	0	12

^aN.D. denotes mutations of residues for which the minimum distance from the active site cannot be determined, as these residues are unmodeled in the PafA crystal structure (PDB ID: 5TJ3, (16); see **Materials and Methods**).

Table S8. Catalytic effects of all non-active-site variants ($k_{\text{cat}}/K_{\text{M}}^{\text{MeP, chem. mutant}}/k_{\text{cat}}/K_{\text{M}}^{\text{MeP, WT}} < 1$) as a function of minimum distance from the active site, binned by magnitude of effect and p -value.

A	Scan				Contact ^a			
	Glycine		Valine		K162	R164	Zn ²⁺	O _n
	FC1	<i>p</i> -value	FC1	<i>p</i> -value				
Y112	4.7 × 10 ¹	<1.0 × 10 ⁻⁵	2.3 × 10 ¹	1.4 × 10 ⁻⁴	–	sc	–	–
C113	2.5	3.9 × 10 ⁻³	1.4	0.28	–	sc	–	–
S160	0.5	5.7 × 10 ⁻²	–	–	bb	–	–	–
L161	9.9	6.9 × 10 ⁻⁴	1.6	2.8 × 10 ⁻²	bb	–	–	–
D163	4.2	7.9 × 10 ⁻⁴	2.6 × 10 ¹	2.0 × 10 ⁻⁴	–	bb	–	–
A165	1.2	0.62	–	–	sc	–	–	–
S166	2.8	1.6 × 10 ⁻⁴	1.8	8.9 × 10 ⁻²	sc	–	–	–
L168	–	–	0.8	0.55	–	bb	–	–
W179	–	–	–	–	bb	–	–	–
A302	3.9	1.1 × 10 ⁻²	2.1 × 10 ²	<1.0 × 10 ⁻⁵	sc	–	–	–
Y306	4.5 × 10 ¹	<1.0 × 10 ⁻⁵	1.1 × 10 ¹	1.0 × 10 ⁻⁵	sc	–	–	–

B	Scan				Contact ^a			
	Glycine		Valine		K162	R164	Zn ²⁺	O _n
	FC1	<i>p</i> -value	FC1	<i>p</i> -value				
N100	2.6 × 10 ¹	1.2 × 10 ⁻³	–	–	–	sc	–	1
K162	>2.7 × 10 ³	<1.0 × 10 ⁻⁵	>1.7 × 10 ⁴	<1.0 × 10 ⁻⁵	–	sc	–	2
R164	2.0 × 10 ³	<1 × 10 ⁻⁵	1.4 × 10 ³	<1.0 × 10 ⁻⁵	sc	–	–	2
D38	>1.3 × 10 ¹	1.7 × 10 ⁻⁴	–	–	sc	–	–	–
D305	–	–	–	–	sc	–	1	–
H309	–	–	–	–	–	–	1	–
H486	–	–	–	–	–	–	1	–
T79	–	–	–	–	–	sc	2	–
H353	–	–	1.0	0.9	–	–	2	–
D352	1.6	0.12	–	–	–	–	2	–

^aDenotes interactions between each residue and K162, R164, either active site Zn²⁺ ion (Zn1 denoted by “1” and Zn2 denoted by “2”) or a substrate phosphoryl oxygen (O1 denoted by “1” and O2 denoted by “2”). Interactions with the K162 or R164 side chain or backbone atoms are denoted by “sc” and “bb,” respectively.

Table S9. FC1 effects for glycine and valine mutations of the (A) 2nd shell and (B) active site residues.

Mutant	FC1			
	On-chip		Off-chip	
	Median	<i>p</i> -value	MecMUP:MeP ^a	MepNPP:MeP ^b
T79S	1.4 × 10 ¹	0.0005	7.6	0.9
N100A	–	–	6.2	2.5
K162A	>1.1 × 10 ²	<1.0 × 10 ⁻⁵	–	3.6 × 10 ⁶
R164A	>5.8 × 10 ²	<1.0 × 10 ⁻⁵	1.6 × 10 ⁴	1.7 × 10 ³

^aSee **Materials and Methods** for assay conditions. ^bFC1 using MepNPP and MeP calculated from ref. (16).

Table S10. Comparison of on- and off-chip FC1 measurements for active site mutants.

Shell	FC1 ^a					
	$p < 0.01$			$p \geq 0.01$	Undefined p -value	All p -values
	> 10	> 5 & < 10	< 5	Any	Undefined	Any
Active Site	4	0	0	2	4	10
2	4	1	2	3	1	11
3	6	2	8	24	2	42
4	3	3	22	52	7	87
5	0	4	28	81	5	118
6	3	5	24	79	6	117
7	3	3	23	54	5	88
8	0	0	8	35	2	45
9	0	0	0	2	0	2
N.D. ^b	0	0	0	6	0	6
Surface Exposed ^c	4	6	53	151	6	220

^aFC1 and p -values for each residue were determined from the larger FC1 effect of the valine and glycine library variants.

^bN.D. denotes mutations of residues for which the interaction shell cannot be determined, as these are residues are unmodeled in the PafA crystal structure (PDB ID: 5TJ3, (16); see **Materials and Methods**). ^cSee **Materials and Methods** for details of determining surface exposure.

Table S11. Distribution of FC1 effect magnitudes for residues within the active site, each K162/R164 interaction shell, and within the subset of residues that are surface exposed.

Name	Organism	Abbreviation	PDB ID	Cognate Reaction	Auxiliary Domain						
					N-terminal	1	2	3.1	3.2	4	C-terminal
Alkaline phosphatase	<i>Escherichia coli</i>	EcAP	3TG0	Phosphomonoesterase	N-terminus:P41	A88:V99	K114:D128	V146:A200	G207:P297	A373:E411	-
Alkaline phosphatase	<i>Halobacterium salinarum</i>	HSAP	2X98	Phosphomonoesterase	-	P105:T112	K127:V146	I163:P199	Q206:N272	G350:G434	-
Cold-active alkaline phosphatase	<i>Shewanella sp. AP1</i>	SCAP	3A52	Phosphomonoesterase	-	P48:V55	K70:P84	A102:A137	G144:N197	G273:G361	-
Alkaline phosphatase	<i>Vibrio sp. G15-21</i>	VLAP	3E2D	Phosphomonoesterase	-	P57:V62	Y77:H91	V109:A144	G151:S244	G319:T464	-
Alkaline phosphatase	<i>Halomonas sp. #593</i>	HsAP	3WBH	Phosphomonoesterase	-	P57:V62	Y77:P91	V109:P144	G151:T240	G315:T460	-
Intestinal-type alkaline phosphatase 1	<i>Rattus norvegicus</i>	IAP	4KJG	Phosphomonoesterase	N-terminus:S32	N84:V89	K104:E128	V146:I196	G203:P286	V361:T431	-
Alkaline phosphatase PhoK	<i>Sphingomonas sp.</i>	SPAP	3Q3Q	Phosphomonoesterase	N-terminus:P39	-	R101:L147	V168:A183	G190:T270	G348:T490	-
Alkaline phosphatase PafA	<i>Elizabethkingia meningoseptica</i>	PafA	5T13	Phosphomonoesterase	N-terminus:P27	-	V91:L137	V159:P174	D181:T275	A356:T485	-
Alkaline phosphatase, placental type	<i>Homo sapiens</i>	PLAP	3MK1	Phosphomonoesterase	N-terminus:A32	N84:V89	K104:E128	V146:I196	G203:P286	V361:T431	-
Alkaline phosphatase	<i>Pandanus borealis</i>	SAP	1SHQ	Phosphomonoesterase	N-terminus:Q27	N78:V83	A92:F124	V142:F196	G203:P285	T360:T431	-
Alkaline phosphatase	Antarctic bacterium TAB5	TAP	2IUC	Phosphomonoesterase	-	S76:V81	K96:A110	V128:L163	G170:N229	G305:G336	-
Phosphodiesterases-nucleotide pyrophosphatase	<i>Xanthomonas axonopodis pv. Citri</i>	XacNPP	2RH6	Phosphodiesterase	N-terminus:A42	-	R102:G136	W154:P168	K176:V178	A261:S362	-
Venom phosphodiesterase	<i>Naja atra</i>	PDE	5GZ5	Phosphodiesterase	N-terminus:F136	-	Y197:G231	Y249:P263	K271:T273	E356:T461	P525:C-terminus
Ectonucleotide pyrophosphatase/phosphodiesterase family member 1	<i>Mus musculus</i>	ENPP1	4B56	Phosphodiesterase	N-terminus:F189	-	Y250:K284	Y302:P316	G324:V326	E409:F516	P580:C-terminus
Ectonucleotide pyrophosphatase/phosphodiesterase family member 2	<i>Homo sapiens</i>	ENPP2	4ZG7	Phosphodiesterase	N-terminus:F161	-	Y222:G256	F275:P281	V278:I280	E363:D474	N538:C-terminus
Ectonucleotide pyrophosphatase/phosphodiesterase family member 2	<i>Rattus norvegicus</i>	ENPP2	5DLT	Phosphodiesterase	N-terminus:F160	-	Y221:G255	F274:I279	V277:I279	E362:D473	N537:C-terminus
Ectonucleotide pyrophosphatase/phosphodiesterase family member 2	<i>Mus musculus</i>	ENPP2	3NKR	Phosphodiesterase	N-terminus:F160	-	Y221:G255	F274:I279	V277:I279	E362:D473	N537:C-terminus
Ectonucleotide pyrophosphatase/phosphodiesterase family member 3	<i>Homo sapiens</i>	ENPP3	6C01	Phosphodiesterase	N-terminus:F156	-	Y217:H251	Y269:P283	G291:V293	D376:N482	P546:C-terminus
Ectonucleotide pyrophosphatase/phosphodiesterase family member 3	<i>Rattus norvegicus</i>	ENPP3	6F2T	Phosphodiesterase	N-terminus:F157	-	Y218:S252	Y270:P284	N292:V294	D377:T482	P546:C-terminus
Big(S'-adenosyl)-triphosphatase ENPP4	<i>Homo sapiens</i>	ENPP4	4LOY	Phosphodiesterase	-	-	Y82:E115	A134:S148	S156:V158	T241:D335	-
Ectonucleotide pyrophosphatase/phosphodiesterase family member 5	<i>Homo sapiens</i>	ENPP5	5VEM	Phosphodiesterase	N-terminus:L24	-	F84:E119	A137:P151	E159:V161	T242:N338	-
Glycerophosphocholine cholinephosphodiesterase ENPP6	<i>Mus musculus</i>	ENPP6	5EGH	Phosphodiesterase	-	-	H83:G119	Y137:P151	T159:P161	T244:W353	-
Ectonucleotide pyrophosphatase/phosphodiesterase family member 7	<i>Homo sapiens</i>	ENPP7	5TCD	Phosphodiesterase	-	-	Y87:G122	F140:V154	I162:E171	T250:E352	-

Table S12. Unique structurally characterized AP superfamily phosphate monoesterases and diesterases and definitions for their non-conserved “Auxiliary Domains.”

FC1						
Domain	$p < 0.01$			$p \geq 0.01$	Undefined p -value	All p -values
	>10	>5 & <10	<5	Any	Undefined	Any
Rossmann core	5	11	45	157	20	238
Aux. 2	5	2	14	24	2	47
Aux. 3	7	3	28	68	5	111
Aux. 4	6	2	28	89	5	130

Table S13. Number and magnitudes of FC1 effects within the Rossmann fold core and the three Auxiliary (“Aux.”) Domains.

Region	Effect			
	FC2 ^a	Catalytic ^b	FC2 ^a & Catalytic ^b	None
Nucleophile helix	0.69	0.063	0.13	0.13
Nucleophile helix contact	0.52	0.15	0.05	0.28
Catalytic Zn ²⁺ ligand	0.16	0	0.5	0.33
Catalytic Zn ²⁺ contact	0.47	0.14	0.16	0.23
“Distal” Zn ²⁺ contact	0.27	0.02	0.27	0.44
Other	0.23	0.12	0.04	0.61

^aFC2 effects defined as having $p < 0.01$ as determined from bootstrap hypothesis testing.

^bCatalytic effects defined as having $p < 0.05$ as determined from bootstrap hypothesis testing, and $(k_{\text{cat}}/K_{\text{M}}^{\text{chem}})_{\text{mutant}} < (k_{\text{cat}}/K_{\text{M}}^{\text{chem}})^{\text{WT}}$.

Table S14. Fraction of measurable mutants with catalytic ($k_{\text{cat}}/K_{\text{M}}^{\text{chem}}$) effects, FC2 effects, and mutants with both catalytic and FC2 effects within different PafA regions. See **Table S15** for counts of mutants in each category.

Region	Effect					
	Total	FC2 ^a	Catalytic ^b	FC2 ^a & Catalytic ^b	None	Undetermined
Nucleophile helix	19	11	1	2	2	3
Nucleophile helix contact	65	31	9	3	17	5
Catalytic Zn ²⁺	12	1	0	3	2	6
Catalytic Zn ²⁺ contact	44	20	6	7	10	1
“Distal” Zn ²⁺ contact	48	13	1	13	21	0
Other	848	190	98	36	497	27

^aFC2 effects defined as having $p < 0.01$ as determined from bootstrap hypothesis testing. ^bCatalytic effects defined as having $p < 0.05$ as determined from bootstrap hypothesis testing, and $(k_{\text{cat}}/K_{\text{M}}^{\text{chem}})_{\text{mutant}} < (k_{\text{cat}}/K_{\text{M}}^{\text{chem}})^{\text{WT}}$.

Table S15. Number of measurable mutants with significant catalytic ($k_{\text{cat}}/K_{\text{M}}^{\text{chem}}$) effects, FC2 effects, and mutants with both catalytic and FC2 effects within different PafA regions.

Overlap of mutants with FC4 effects ($p < 0.1$)			
Parameter or FC	p -value Threshold	Count	FC4 Intersection Count (% of FC4 at $p < 0.1$)
k_{cat}/K_M^{chem}	0.05	185	38 (70)
FC1	0.01	181	29 (54)
FC2	0.01	331	36 (67)
FC3	0.01	73	8 (15)
FC4	0.1	54	54 (100)

Table S16. Overlap of FC4 effects ($p < 0.1$) with those on other parameters and FCs.

Term	Type	Definition	Description	<i>p</i> -value	Units	Eq.
k_1	constant	$1.42 \times 10^6 = (k_{cat}/K_M)^{cMUP,WT}$	Second order rate constant for substrate binding to PafA, assumed to be the apparent second order rate constant of cMUP hydrolysis by WT PafA (which is binding-limited)	–	$M^{-1}s^{-1}$	–
f_c	constant	776 ± 126 $(k_{chem,1}^{cMUP}/k_{chem,1}^{MeP})$	Fit relative first order rate constants of MeP vs. cMUP substrate hydrolysis on the enzyme	–	–	30
T-Effect	parameter	$\frac{[(k_{cat}/K_M)^{mutant}/(k_{cat}/K_M)^{WT}]^{23^\circ C}}{[(k_{cat}/K_M)^{mutant}/(k_{cat}/K_M)^{WT}]^{37^\circ C}}$	Fold-change in WT-normalized activity upon expression at 23°C vs. 37°C	–	–	9
Zn-Effect	parameter	$\frac{[(k_{cat}/K_M)^{mutant}/(k_{cat}/K_M)^{WT}]^{1000 \mu M Zn^{2+}}}{[(k_{cat}/K_M)^{mutant}/(k_{cat}/K_M)^{WT}]^{10 \mu M Zn^{2+}}}$	Fold-change in WT-normalized activity upon expression at 1000 $\mu M Zn^{2+}$ vs. 10 $\mu M Zn^{2+}$	–	–	10
f_a	parameter	$\frac{(f_s - 1)(k_{cat}/K_M)^{MeP,obs}(k_{cat}/K_M)^{cMUP,obs}}{k_1[f_c(k_{cat}/K_M)^{MeP,obs} - (k_{cat}/K_M)^{cMUP,obs}]}$	The fraction of apparent enzyme that is active (correctly folded) assuming a two-state model	< 0.01	–	32
Catalytic Effect	parameter	$\frac{(k_{cat}/K_M)^{MeP,chem}}{(k_{cat}/K_M)^{WT}}$	Mutational effect on intrinsic catalytic efficiency (corrected for the f_a , the active fraction of enzyme)	< 0.05	–	36
FC1	FC	$\frac{[(k_{cat}/K_M)^{MecMUP,mutant}/(k_{cat}/K_M)^{MecMUP,WT}]}{[(k_{cat}/K_M)^{MeP,mutant}/(k_{cat}/K_M)^{MeP,WT}]}$	The ratio of WT-normalized change in activity towards MecMUP to that of MeP. This value is f_a independent.	< 0.01	–	12 & 13
FC2	FC	$(K_i P_i)^{mutant}/(K_i P_i)^{WT}$ where $(K_i P_i)^{mutant} < (K_i P_i)^{WT}$	The fold-change of K_i for P_i from WT PafA, where K_i for P_i is tighter than that of the WT	< 0.01	–	–
FC3	FC	$(K_i P_i)^{mutant}/(K_i P_i)^{WT}$ where $(K_i P_i)^{mutant} \geq (K_i P_i)^{WT}$	The fold-change of K_i for P_i from WT PafA, where K_i for P_i is weaker than that of the WT	< 0.01	–	–
FC4	FC	$\frac{k_{on,P_i}K_{i,P_i}^{cMUP,obs}}{f_a k_{on,P_i}K_{i,P_i} - k_{cat}^{cMUP,obs}}$ where $k_{on,P_i} = k_1$	An estimate for $k_{chem,2}$, the first-order rate constant for E- P_i intermediate hydrolysis (a potential k_{cat} rate limiting step). The definition was made using a rate law obtained by the method of net rate constants.	< 0.1 or < 0.05	s^{-1}	40

Table S17. Definitions and descriptions of a subset constants, parameters, and functional components (FCs) discussed herein. Defined *p*-values thresholds are used to delineate mutants with strong evidence for effects on parameters and FCs.

Captions for Auxiliary Supplementary Materials, Data S1 and S2

1. **Data S1.** Kinetic and thermodynamic parameter table, CSV
(AuxiliarySupplementaryMaterials_S1.csv)
2. **Data S2.** Kinetic and thermodynamic parameter tables, PDF
(AuxiliarySupplementaryMaterials_S2.pdf)

OSF Repository Data

The Open Science Foundation repository for this study is located at: <https://doi.org/10.17605/OSF.IO/QRN3C>. The repository contains the following components:

1. **Code.** Code used to obtain and process images, and fit kinetic and thermodynamic parameters.
2. **Sequences and parameter summary.** Summary files of fit kinetic and thermodynamic parameters and Functional Components, and PafA residue biophysical parameters.
3. **Kinetic data (multiple components).** Each kinetic data component contains the following individual CSV files for experiments of a specific type (*e.g.* hydrolysis of cMUP, MeP, MecMUP, or inhibition by phosphate).
 - (a) Aggregate summaries of kinetic and thermodynamic constants measured for each mutant as well as a data dictionary defining the columns within each aggregate CSV summary.
 - (b) Per-experiment data. CSV files summarizing the data from each experiment.
4. **Structural representations.** PyMOL files corresponding to all Main Text figures containing structural information.

References and Notes

1. Q. Wang, E. Pierce-Hoffman, B. B. Cummings, J. Alföldi, L. C. Francioli, L. D. Gauthier, A. J. Hill, A. H. O'Donnell-Luria, K. J. Karczewski, D. G. MacArthur, Genome Aggregation Database Production Team, Genome Aggregation Database Consortium, Landscape of multi-nucleotide variants in 125,748 human exomes and 15,708 genomes. *Nat. Commun.* **11**, 2539 (2020). [doi:10.1038/s41467-019-12438-5](https://doi.org/10.1038/s41467-019-12438-5) [Medline](#)
2. M. Claussnitzer, J. H. Cho, R. Collins, N. J. Cox, E. T. Dermitzakis, M. E. Hurles, S. Kathiresan, E. E. Kenny, C. M. Lindgren, D. G. MacArthur, K. N. North, S. E. Plon, H. L. Rehm, N. Risch, C. N. Rotimi, J. Shendure, N. Soranzo, M. I. McCarthy, A brief history of human disease genetics. *Nature* **577**, 179–189 (2020). [doi:10.1038/s41586-019-1879-7](https://doi.org/10.1038/s41586-019-1879-7) [Medline](#)
3. M. Lek, K. J. Karczewski, E. V. Minikel, K. E. Samocha, E. Banks, T. Fennell, A. H. O'Donnell-Luria, J. S. Ware, A. J. Hill, B. B. Cummings, T. Tukiainen, D. P. Birnbaum, J. A. Kosmicki, L. E. Duncan, K. Estrada, F. Zhao, J. Zou, E. Pierce-Hoffman, J. Berghout, D. N. Cooper, N. Deflaux, M. DePristo, R. Do, J. Flannick, M. Fromer, L. Gauthier, J. Goldstein, N. Gupta, D. Howrigan, A. Kiezun, M. I. Kurki, A. L. Moonshine, P. Natarajan, L. Orozco, G. M. Peloso, R. Poplin, M. A. Rivas, V. Ruano-Rubio, S. A. Rose, D. M. Ruderfer, K. Shakir, P. D. Stenson, C. Stevens, B. P. Thomas, G. Tiao, M. T. Tusie-Luna, B. Weisburd, H.-H. Won, D. Yu, D. M. Altshuler, D. Ardissino, M. Boehnke, J. Danesh, S. Donnelly, R. Elosua, J. C. Florez, S. B. Gabriel, G. Getz, S. J. Glatt, C. M. Hultman, S. Kathiresan, M. Laakso, S. McCarroll, M. I. McCarthy, D. McGovern, R. McPherson, B. M. Neale, A. Palotie, S. M. Purcell, D. Saleheen, J. M. Scharf, P. Sklar, P. F. Sullivan, J. Tuomilehto, M. T. Tsuang, H. C. Watkins, J. G. Wilson, M. J. Daly, D. G. MacArthur, Exome Aggregation Consortium, Analysis of protein-coding genetic variation in 60,706 humans. *Nature* **536**, 285–291 (2016). [doi:10.1038/nature19057](https://doi.org/10.1038/nature19057) [Medline](#)
4. A. Stein, D. M. Fowler, R. Hartmann-Petersen, K. Lindorff-Larsen, Biophysical and mechanistic models for disease-causing protein variants. *Trends Biochem. Sci.* **44**, 575–588 (2019). [doi:10.1016/j.tibs.2019.01.003](https://doi.org/10.1016/j.tibs.2019.01.003) [Medline](#)
5. J. B. Kinney, D. M. McCandlish, Massively parallel assays and quantitative sequence-function relationships. *Annu. Rev. Genomics Hum. Genet.* **20**, 99–127 (2019). [doi:10.1146/annurev-genom-083118-014845](https://doi.org/10.1146/annurev-genom-083118-014845) [Medline](#)
6. C. Blanco, E. Janzen, A. Pressman, R. Saha, I. A. Chen, Molecular fitness landscapes from high-coverage sequence profiling. *Annu. Rev. Biophys.* **48**, 1–18 (2019). [doi:10.1146/annurev-biophys-052118-115333](https://doi.org/10.1146/annurev-biophys-052118-115333) [Medline](#)
7. J. Weile, F. P. Roth, Multiplexed assays of variant effects contribute to a growing genotype-phenotype atlas. *Hum. Genet.* **137**, 665–678 (2018). [doi:10.1007/s00439-018-1916-x](https://doi.org/10.1007/s00439-018-1916-x) [Medline](#)
8. G. P. Lisi, J. P. Loria, Allosterity in enzyme catalysis. *Curr. Opin. Struct. Biol.* **47**, 123–130 (2017). [doi:10.1016/j.sbi.2017.08.002](https://doi.org/10.1016/j.sbi.2017.08.002) [Medline](#)
9. K. A. Reynolds, R. N. McLaughlin, R. Ranganathan, Hot spots for allosteric regulation on protein surfaces. *Cell* **147**, 1564–1575 (2011). [doi:10.1016/j.cell.2011.10.049](https://doi.org/10.1016/j.cell.2011.10.049) [Medline](#)

10. D. A. Keedy, Z. B. Hill, J. T. Biel, E. Kang, T. J. Rettenmaier, J. Brandão-Neto, N. M. Pearce, F. von Delft, J. A. Wells, J. S. Fraser, An expanded allosteric network in PTP1B by multitemperature crystallography, fragment screening, and covalent tethering. *eLife* **7**, e36307 (2018). [doi:10.7554/eLife.36307](https://doi.org/10.7554/eLife.36307) [Medline](#)
11. D. M. Fowler, C. L. Araya, S. J. Fleishman, E. H. Kellogg, J. J. Stephany, D. Baker, S. Fields, High-resolution mapping of protein sequence-function relationships. *Nat. Methods* **7**, 741–746 (2010). [doi:10.1038/nmeth.1492](https://doi.org/10.1038/nmeth.1492) [Medline](#)
12. C. L. Araya, D. M. Fowler, Deep mutational scanning: Assessing protein function on a massive scale. *Trends Biotechnol.* **29**, 435–442 (2011). [doi:10.1016/j.tibtech.2011.04.003](https://doi.org/10.1016/j.tibtech.2011.04.003) [Medline](#)
13. J. K. Lassila, J. G. Zalatan, D. Herschlag, Biological phosphoryl-transfer reactions: Understanding mechanism and catalysis. *Annu. Rev. Biochem.* **80**, 669–702 (2011). [doi:10.1146/annurev-biochem-060409-092741](https://doi.org/10.1146/annurev-biochem-060409-092741) [Medline](#)
14. P. M. Fordyce, D. Gerber, D. Tran, J. Zheng, H. Li, J. L. DeRisi, S. R. Quake, De novo identification and biophysical characterization of transcription-factor binding sites with microfluidic affinity analysis. *Nat. Biotechnol.* **28**, 970–975 (2010). [doi:10.1038/nbt.1675](https://doi.org/10.1038/nbt.1675) [Medline](#)
15. S. J. Maerkl, S. R. Quake, A systems approach to measuring the binding energy landscapes of transcription factors. *Science* **315**, 233–237 (2007). [doi:10.1126/science.1131007](https://doi.org/10.1126/science.1131007) [Medline](#)
16. F. Sunden, I. AlSadhan, A. Y. Lyubimov, S. Ressler, H. Wiersma-Koch, J. Borland, C. L. Brown Jr., T. A. Johnson, Z. Singh, D. Herschlag, Mechanistic and evolutionary insights from comparative enzymology of phosphomonoesterases and phosphodiesterases across the alkaline phosphatase superfamily. *J. Am. Chem. Soc.* **138**, 14273–14287 (2016). [doi:10.1021/jacs.6b06186](https://doi.org/10.1021/jacs.6b06186) [Medline](#)
17. M. M. Santoro, D. W. Bolen, Unfolding free energy changes determined by the linear extrapolation method. 1. Unfolding of phenylmethanesulfonyl α -chymotrypsin using different denaturants. *Biochemistry* **27**, 8063–8068 (1988). [doi:10.1021/bi00421a014](https://doi.org/10.1021/bi00421a014) [Medline](#)
18. M. Brune, J. L. Hunter, J. E. T. Corrie, M. R. Webb, Direct, real-time measurement of rapid inorganic phosphate release using a novel fluorescent probe and its application to actomyosin subfragment 1 ATPase. *Biochemistry* **33**, 8262–8271 (1994). [doi:10.1021/bi00193a013](https://doi.org/10.1021/bi00193a013) [Medline](#)
19. P. J. O'Brien, D. Herschlag, Alkaline phosphatase revisited: Hydrolysis of alkyl phosphates. *Biochemistry* **41**, 3207–3225 (2002). [doi:10.1021/bi012166y](https://doi.org/10.1021/bi012166y) [Medline](#)
20. R. M. Addabbo, M. D. Dalphin, M. F. Mecha, Y. Liu, A. Staikos, V. Guzman-Luna, S. Cavagnero, Complementary role of co- and post-translational events in de novo protein biogenesis. *J. Phys. Chem. B* **124**, 6488–6507 (2020). [doi:10.1021/acs.jpcc.0c03039](https://doi.org/10.1021/acs.jpcc.0c03039) [Medline](#)
21. J. M. Sturtevant, M. H. Yu, C. Haase-Pettingell, J. King, Thermostability of temperature-sensitive folding mutants of the P22 tailspike protein. *J. Biol. Chem.* **264**, 10693–10698 (1989). [doi:10.1016/S0021-9258\(18\)81678-7](https://doi.org/10.1016/S0021-9258(18)81678-7) [Medline](#)

22. M. Guo, Y. Xu, M. Gruebele, Temperature dependence of protein folding kinetics in living cells. *Proc. Natl. Acad. Sci. U.S.A.* **109**, 17863–17867 (2012). [doi:10.1073/pnas.1201797109](https://doi.org/10.1073/pnas.1201797109) [Medline](#)
23. D. H. Smith, J. King, Temperature-sensitive mutants blocked in the folding or subunit assembly of the bacteriophage P22 tail spike protein. III. Intensive polypeptide chains synthesized at 39°C. *J. Mol. Biol.* **145**, 653–676 (1981). [doi:10.1016/0022-2836\(81\)90308-9](https://doi.org/10.1016/0022-2836(81)90308-9) [Medline](#)
24. D. Baker, J. L. Sohl, D. A. Agard, A protein-folding reaction under kinetic control. *Nature* **356**, 263–265 (1992). [doi:10.1038/356263a0](https://doi.org/10.1038/356263a0) [Medline](#)
25. H. Im, M.-S. Woo, K. Y. Hwang, M.-H. Yu, Interactions causing the kinetic trap in serpin protein folding. *J. Biol. Chem.* **277**, 46347–46354 (2002). [doi:10.1074/jbc.M207682200](https://doi.org/10.1074/jbc.M207682200) [Medline](#)
26. C. Park, S. Marqusee, Probing the high energy states in proteins by proteolysis. *J. Mol. Biol.* **343**, 1467–1476 (2004). [doi:10.1016/j.jmb.2004.08.085](https://doi.org/10.1016/j.jmb.2004.08.085) [Medline](#)
27. S. Thompson, Y. Zhang, C. Ingle, K. A. Reynolds, T. Kortemme, Altered expression of a quality control protease in *E. coli* reshapes the in vivo mutational landscape of a model enzyme. *eLife* **9**, e53476 (2020). [doi:10.7554/eLife.53476](https://doi.org/10.7554/eLife.53476) [Medline](#)
28. T. Gidalevitz, V. Prahlad, R. I. Morimoto, The stress of protein misfolding: From single cells to multicellular organisms. *Cold Spring Harb. Perspect. Biol.* **3**, a009704–a009704 (2011). [doi:10.1101/cshperspect.a009704](https://doi.org/10.1101/cshperspect.a009704) [Medline](#)
29. J. L. Sohl, S. S. Jaswal, D. A. Agard, Unfolded conformations of α -lytic protease are more stable than its native state. *Nature* **395**, 817–819 (1998). [doi:10.1038/27470](https://doi.org/10.1038/27470) [Medline](#)
30. S. S. Jaswal, J. L. Sohl, J. H. Davis, D. A. Agard, Energetic landscape of α -lytic protease optimizes longevity through kinetic stability. *Nature* **415**, 343–346 (2002). [doi:10.1038/415343a](https://doi.org/10.1038/415343a) [Medline](#)
31. A. L. Watters, P. Deka, C. Corrent, D. Callender, G. Varani, T. Sosnick, D. Baker, The highly cooperative folding of small naturally occurring proteins is likely the result of natural selection. *Cell* **128**, 613–624 (2007). [doi:10.1016/j.cell.2006.12.042](https://doi.org/10.1016/j.cell.2006.12.042) [Medline](#)
32. F. Bemporad, J. Gsponer, H. I. Hopearuoho, G. Plakoutsi, G. Stati, M. Stefani, N. Taddei, M. Vendruscolo, F. Chiti, Biological function in a non-native partially folded state of a protein. *EMBO J.* **27**, 1525–1535 (2008). [doi:10.1038/emboj.2008.82](https://doi.org/10.1038/emboj.2008.82) [Medline](#)
33. R. E. Jefferson, T. M. Blois, J. U. Bowie, Membrane proteins can have high kinetic stability. *J. Am. Chem. Soc.* **135**, 15183–15190 (2013). [doi:10.1021/ja407232b](https://doi.org/10.1021/ja407232b) [Medline](#)
34. J. G. Zalatan, T. D. Fenn, D. Herschlag, Comparative enzymology in the alkaline phosphatase superfamily to determine the catalytic role of an active-site metal ion. *J. Mol. Biol.* **384**, 1174–1189 (2008). [doi:10.1016/j.jmb.2008.09.059](https://doi.org/10.1016/j.jmb.2008.09.059) [Medline](#)
35. L. D. Andrews, T. D. Fenn, D. Herschlag, Ground state destabilization by anionic nucleophiles contributes to the activity of phosphoryl transfer enzymes. *PLoS Biol.* **11**, e1001599 (2013). [doi:10.1371/journal.pbio.1001599](https://doi.org/10.1371/journal.pbio.1001599) [Medline](#)

36. D. Hilvert, Design of protein catalysts. *Annu. Rev. Biochem.* **82**, 447–470 (2013). [doi:10.1146/annurev-biochem-072611-101825](https://doi.org/10.1146/annurev-biochem-072611-101825) [Medline](#)
37. M. I. Freiberger, A. B. Guzovsky, P. G. Wolynes, R. G. Parra, D. U. Ferreira, Local frustration around enzyme active sites. *Proc. Natl. Acad. Sci. U.S.A.* **116**, 4037–4043 (2019). [doi:10.1073/pnas.1819859116](https://doi.org/10.1073/pnas.1819859116) [Medline](#)
38. K. L. Morley, R. J. Kazlauskas, Improving enzyme properties: When are closer mutations better? *Trends Biotechnol.* **23**, 231–237 (2005). [doi:10.1016/j.tibtech.2005.03.005](https://doi.org/10.1016/j.tibtech.2005.03.005) [Medline](#)
39. O. Dagliyan, N. V. Dokholyan, K. M. Hahn, Engineering proteins for allosteric control by light or ligands. *Nat. Protoc.* **14**, 1863–1883 (2019). [doi:10.1038/s41596-019-0165-3](https://doi.org/10.1038/s41596-019-0165-3) [Medline](#)
40. J. W. McCormick, D. Pincus, O. Resnekov, K. A. Reynolds, Strategies for engineering and rewiring kinase regulation. *Trends Biochem. Sci.* **45**, 259–271 (2020). [doi:10.1016/j.tibs.2019.11.005](https://doi.org/10.1016/j.tibs.2019.11.005) [Medline](#)
41. K. Gunasekaran, B. Ma, R. Nussinov, Is allostery an intrinsic property of all dynamic proteins? *Proteins* **57**, 433–443 (2004). [doi:10.1002/prot.20232](https://doi.org/10.1002/prot.20232) [Medline](#)
42. J. A. Hardy, J. A. Wells, Searching for new allosteric sites in enzymes. *Curr. Opin. Struct. Biol.* **14**, 706–715 (2004). [doi:10.1016/j.sbi.2004.10.009](https://doi.org/10.1016/j.sbi.2004.10.009) [Medline](#)
43. G. R. Bowman, E. R. Bolin, K. M. Hart, B. C. Maguire, S. Marqusee, Discovery of multiple hidden allosteric sites by combining Markov state models and experiments. *Proc. Natl. Acad. Sci. U.S.A.* **112**, 2734–2739 (2015). [doi:10.1073/pnas.1417811112](https://doi.org/10.1073/pnas.1417811112) [Medline](#)
44. F. Sunden, A. Peck, J. Salzman, S. Ressler, D. Herschlag, Extensive site-directed mutagenesis reveals interconnected functional units in the alkaline phosphatase active site. *eLife* **4**, e06181 (2015). [doi:10.7554/eLife.06181](https://doi.org/10.7554/eLife.06181) [Medline](#)
45. P. J. Carter, G. Winter, A. J. Wilkinson, A. R. Fersht, The use of double mutants to detect structural changes in the active site of the tyrosyl-tRNA synthetase (*Bacillus stearothermophilus*). *Cell* **38**, 835–840 (1984). [doi:10.1016/0092-8674\(84\)90278-2](https://doi.org/10.1016/0092-8674(84)90278-2) [Medline](#)
46. P. Carter, J. A. Wells, Dissecting the catalytic triad of a serine protease. *Nature* **332**, 564–568 (1988). [doi:10.1038/332564a0](https://doi.org/10.1038/332564a0) [Medline](#)
47. D. Herschlag, A. Natarajan, Fundamental challenges in mechanistic enzymology: Progress toward understanding the rate enhancements of enzymes. *Biochemistry* **52**, 2050–2067 (2013). [doi:10.1021/bi4000113](https://doi.org/10.1021/bi4000113) [Medline](#)
48. W. P. Jencks, Mechanism of enzyme action. *Annu. Rev. Biochem.* **32**, 639–676 (1963). [doi:10.1146/annurev.bi.32.070163.003231](https://doi.org/10.1146/annurev.bi.32.070163.003231) [Medline](#)
49. A. R. Fersht, *Enzyme Structure and Mechanism* (W.H. Freeman and Co., ed. 2, 1985).
50. W. P. Jencks, Binding energy, specificity, and enzymic catalysis: The Circe effect. *Adv. Enzymol. Relat. Areas Mol. Biol.* **43**, 219–410 (1975). [doi:10.1002/9780470122884.ch4](https://doi.org/10.1002/9780470122884.ch4) [Medline](#)

51. L. D. Andrews, H. Deng, D. Herschlag, Isotope-edited FTIR of alkaline phosphatase resolves paradoxical ligand binding properties and suggests a role for ground-state destabilization. *J. Am. Chem. Soc.* **133**, 11621–11631 (2011). [doi:10.1021/ja203370b](https://doi.org/10.1021/ja203370b) [Medline](#)
52. W. J. Albery, J. R. Knowles, Evolution of enzyme function and the development of catalytic efficiency. *Biochemistry* **15**, 5631–5640 (1976). [doi:10.1021/bi00670a032](https://doi.org/10.1021/bi00670a032) [Medline](#)
53. F. M. Menger, Analysis of ground-state and transition-state effects in enzyme catalysis. *Biochemistry* **31**, 5368–5373 (1992). [doi:10.1021/bi00138a018](https://doi.org/10.1021/bi00138a018) [Medline](#)
54. J. D. McCarter, M. J. Adam, S. G. Withers, Binding energy and catalysis. Fluorinated and deoxygenated glycosides as mechanistic probes of Escherichia coli (lacZ) β -galactosidase. *Biochem. J.* **286**, 721–727 (1992). [doi:10.1042/bj2860721](https://doi.org/10.1042/bj2860721) [Medline](#)
55. S. A. Moore, W. P. Jencks, Formation of active site thiol esters of CoA transferase and the dependence of catalysis on specific binding interactions. *J. Biol. Chem.* **257**, 10893–10907 (1982). [doi:10.1016/S0021-9258\(18\)33908-5](https://doi.org/10.1016/S0021-9258(18)33908-5) [Medline](#)
56. A. Whitty, C. A. Fierke, W. P. Jencks, Role of binding energy with coenzyme A in catalysis by 3-oxoacid coenzyme A transferase. *Biochemistry* **34**, 11678–11689 (1995). [doi:10.1021/bi00037a005](https://doi.org/10.1021/bi00037a005) [Medline](#)
57. Y.-L. Zhang, F. Hollfelder, S. J. Gordon, L. Chen, Y.-F. Keng, L. Wu, D. Herschlag, Z.-Y. Zhang, Impaired transition state complementarity in the hydrolysis of O-arylphosphorothioates by protein-tyrosine phosphatases. *Biochemistry* **38**, 12111–12123 (1999). [doi:10.1021/bi990836j](https://doi.org/10.1021/bi990836j) [Medline](#)
58. W. E. Hull, S. E. Halford, H. Gutfreund, B. D. Sykes, Phosphorus-31 nuclear magnetic resonance study of alkaline phosphatase: The role of inorganic phosphate in limiting the enzyme turnover rate at alkaline pH. *Biochemistry* **15**, 1547–1561 (1976). [doi:10.1021/bi00652a028](https://doi.org/10.1021/bi00652a028) [Medline](#)
59. E. E. Wrenbeck, L. R. Azouz, T. A. Whitehead, Single-mutation fitness landscapes for an enzyme on multiple substrates reveal specificity is globally encoded. *Nat. Commun.* **8**, 15695 (2017). [doi:10.1038/ncomms15695](https://doi.org/10.1038/ncomms15695) [Medline](#)
60. J. R. Klesmith, J.-P. Bacik, E. E. Wrenbeck, R. Michalczyk, T. A. Whitehead, Trade-offs between enzyme fitness and solubility illuminated by deep mutational scanning. *Proc. Natl. Acad. Sci. U.S.A.* **114**, 2265–2270 (2017). [doi:10.1073/pnas.1614437114](https://doi.org/10.1073/pnas.1614437114) [Medline](#)
61. P. Bandaru, N. H. Shah, M. Bhattacharyya, J. P. Barton, Y. Kondo, J. C. Cofsky, C. L. Gee, A. K. Chakraborty, T. Kortemme, R. Ranganathan, J. Kuriyan, Deconstruction of the Ras switching cycle through saturation mutagenesis. *eLife* **6**, e27810 (2017). [doi:10.7554/eLife.27810](https://doi.org/10.7554/eLife.27810) [Medline](#)
62. C. M. Dobson, Protein folding and misfolding. *Nature* **426**, 884–890 (2003). [doi:10.1038/nature02261](https://doi.org/10.1038/nature02261) [Medline](#)
63. M. S. Faber, E. E. Wrenbeck, L. R. Azouz, P. J. Steiner, T. A. Whitehead, Impact of in vivo protein folding probability on local fitness landscapes. *Mol. Biol. Evol.* **36**, 2764–2777 (2019). [doi:10.1093/molbev/msz184](https://doi.org/10.1093/molbev/msz184) [Medline](#)

64. V. Zhao, W. M. Jacobs, E. I. Shakhnovich, Effect of protein structure on evolution of cotranslational folding. *Biophys. J.* **119**, 1123–1134 (2020). [doi:10.1016/j.bpj.2020.06.037](https://doi.org/10.1016/j.bpj.2020.06.037) [Medline](#)
65. N. Halabi, O. Rivoire, S. Leibler, R. Ranganathan, Protein sectors: Evolutionary units of three-dimensional structure. *Cell* **138**, 774–786 (2009). [doi:10.1016/j.cell.2009.07.038](https://doi.org/10.1016/j.cell.2009.07.038) [Medline](#)
66. O. Rivoire, K. A. Reynolds, R. Ranganathan, Evolution-based functional decomposition of proteins. *PLOS Comput. Biol.* **12**, e1004817 (2016). [doi:10.1371/journal.pcbi.1004817](https://doi.org/10.1371/journal.pcbi.1004817) [Medline](#)
67. V. H. Salinas, R. Ranganathan, Coevolution-based inference of amino acid interactions underlying protein function. *eLife* **7**, e34300 (2018). [doi:10.7554/eLife.34300](https://doi.org/10.7554/eLife.34300) [Medline](#)
68. T. Teşileanu, L. J. Colwell, S. Leibler, Protein sectors: Statistical coupling analysis versus conservation. *PLOS Comput. Biol.* **11**, e1004091 (2015). [doi:10.1371/journal.pcbi.1004091](https://doi.org/10.1371/journal.pcbi.1004091) [Medline](#)
69. P. Creixell, J. P. Pandey, A. Palmeri, M. Bhattacharyya, M. Creixell, R. Ranganathan, D. Pincus, M. B. Yaffe, Hierarchical organization endows the kinase domain with regulatory plasticity. *Cell Syst.* **7**, 371–383.e4 (2018). [doi:10.1016/j.cels.2018.08.008](https://doi.org/10.1016/j.cels.2018.08.008) [Medline](#)
70. P. M. Fordyce, D. Pincus, P. Kimmig, C. S. Nelson, H. El-Samad, P. Walter, J. L. DeRisi, Basic leucine zipper transcription factor Hac1 binds DNA in two distinct modes as revealed by microfluidic analyses. *Proc. Natl. Acad. Sci. U.S.A.* **109**, E3084–E3093 (2012). [doi:10.1073/pnas.1212457109](https://doi.org/10.1073/pnas.1212457109) [Medline](#)
71. D. D. Le, T. C. Shimko, A. K. Aditham, A. M. Keys, S. A. Longwell, Y. Orenstein, P. M. Fordyce, Comprehensive, high-resolution binding energy landscapes reveal context dependencies of transcription factor binding. *Proc. Natl. Acad. Sci. U.S.A.* **115**, E3702–E3711 (2018). [doi:10.1073/pnas.1715888115](https://doi.org/10.1073/pnas.1715888115) [Medline](#)
72. A. K. Aditham, C. J. Markin, D. A. Mokhtari, N. DelRosso, P. M. Fordyce, High-throughput affinity measurements of transcription factor and DNA mutations reveal affinity and specificity determinants. *Cell Syst.* **12**, 112–127.e11 (2021). [doi:10.1016/j.cels.2020.11.012](https://doi.org/10.1016/j.cels.2020.11.012) [Medline](#)
73. K. Brower, R. Puccinelli, C. J. Markin, T. C. Shimko, S. A. Longwell, B. Cruz, R. Gomez-Sjoberg, P. M. Fordyce, An open-source, programmable pneumatic setup for operation and automated control of single- and multi-layer microfluidic devices. *HardwareX* **3**, 117–134 (2018). [doi:10.1016/j.ohx.2017.10.001](https://doi.org/10.1016/j.ohx.2017.10.001) [Medline](#)
74. C. J. Markin *et al.*, Revealing enzyme functional architecture via high-throughput microfluidic enzyme kinetics. Open Science Repository (2021); [doi:10.17605/OSF.IO/QRN3C](https://doi.org/10.17605/OSF.IO/QRN3C).
75. A. Untergasser, I. Cutcutache, T. Koressaar, J. Ye, B. C. Faircloth, M. Remm, S. G. Rozen, Primer3—New capabilities and interfaces. *Nucleic Acids Res.* **40**, e115–e115 (2012). [doi:10.1093/nar/gks596](https://doi.org/10.1093/nar/gks596) [Medline](#)

76. J. Cline, J. C. Braman, H. H. Hogrefe, PCR fidelity of pfu DNA polymerase and other thermostable DNA polymerases. *Nucleic Acids Res.* **24**, 3546–3551 (1996). [doi:10.1093/nar/24.18.3546](https://doi.org/10.1093/nar/24.18.3546) [Medline](#)
77. A. Edelstein, N. Amodaj, K. Hoover, R. Vale, N. Stuurman, Computer control of microscopes using μ Manager. *Curr. Protoc. Mol. Biol.* **92**, 14201–142017 (2010). [doi:10.1002/0471142727.mb1420s92](https://doi.org/10.1002/0471142727.mb1420s92) [Medline](#)
78. S. A. Longwell, P. M. Fordyce, micrIO: An open-source autosampler and fraction collector for automated microfluidic input-output. *Lab Chip* **20**, 93–106 (2020). [doi:10.1039/C9LC00512A](https://doi.org/10.1039/C9LC00512A) [Medline](#)
79. M. Model, Intensity calibration and flat-field correction for fluorescence microscopes. *Curr. Protoc. Cytom.* **68**, 1–10 (2014). [doi:10.1002/0471142956.cy1014s68](https://doi.org/10.1002/0471142956.cy1014s68) [Medline](#)
80. S. A. Ba-Saif, A. Williams, Transfer of the diethoxyphosphoryl group [(EtO)₂PO] between imidazole and aryloxy anion nucleophiles. *J. Org. Chem.* **53**, 2204–2209 (1988). [doi:10.1021/jo00245a015](https://doi.org/10.1021/jo00245a015)
81. Q. Zhu, M. Uttamchandani, D. Li, M. L. Lesaichere, S. Q. Yao, Enzymatic profiling system in a small-molecule microarray. *Org. Lett.* **5**, 1257–1260 (2003). [doi:10.1021/ol034233h](https://doi.org/10.1021/ol034233h) [Medline](#)
82. A. J. Kirby, M. Younas, The reactivity of phosphate esters. Reactions of diesters with nucleophiles. *J. Chem. Soc. B* **1970**, 1165 (1970). [doi:10.1039/j29700001165](https://doi.org/10.1039/j29700001165)
83. G. Bradski, The OpenCV library. *Dr. Dobb's J. Sofw. Tools* **25**, 120–125 (2000).
84. B. Efron, R. J. Tibshirani, *An Introduction to the Bootstrap* (CRC Press, 1994).
85. Y. Benjamini, Y. Hochberg, Controlling the false discovery rate: A practical and powerful approach to multiple testing. *J. R. Stat. Soc. B* **57**, 289–300 (1995). [doi:10.1111/j.2517-6161.1995.tb02031.x](https://doi.org/10.1111/j.2517-6161.1995.tb02031.x)
86. S. Schnell, C. Mendoza, Closed form solution for time-dependent enzyme kinetics. *J. Theor. Biol.* **187**, 207–212 (1997). [doi:10.1006/jtbi.1997.0425](https://doi.org/10.1006/jtbi.1997.0425)
87. P. J. A. Cock, T. Antao, J. T. Chang, B. A. Chapman, C. J. Cox, A. Dalke, I. Friedberg, T. Hamelryck, F. Kauff, B. Wilczynski, M. J. L. de Hoon, Biopython: Freely available Python tools for computational molecular biology and bioinformatics. *Bioinformatics* **25**, 1422–1423 (2009). [doi:10.1093/bioinformatics/btp163](https://doi.org/10.1093/bioinformatics/btp163) [Medline](#)
88. M. Z. Tien, A. G. Meyer, D. K. Sydykova, S. J. Spielman, C. O. Wilke, Maximum allowed solvent accessibilities of residues in proteins. *PLOS ONE* **8**, e80635 (2013). [doi:10.1371/journal.pone.0080635](https://doi.org/10.1371/journal.pone.0080635) [Medline](#)
89. B. Rost, C. Sander, Conservation and prediction of solvent accessibility in protein families. *Proteins* **20**, 216–226 (1994). [doi:10.1002/prot.340200303](https://doi.org/10.1002/prot.340200303) [Medline](#)
90. M. F. Sanner, A. J. Olson, J. C. Spehner, Reduced surface: An efficient way to compute molecular surfaces. *Biopolymers* **38**, 305–320 (1996). [doi:10.1002/\(SICI\)1097-0282\(199603\)38:3<305:AID-BIP4>3.0.CO;2-Y](https://doi.org/10.1002/(SICI)1097-0282(199603)38:3<305:AID-BIP4>3.0.CO;2-Y) [Medline](#)
91. UniProt Consortium, UniProt: A worldwide hub of protein knowledge. *Nucleic Acids Res.* **47** (D1), D506–D515 (2019). [doi:10.1093/nar/gky1049](https://doi.org/10.1093/nar/gky1049) [Medline](#)

92. I. Sillitoe, N. Dawson, T. E. Lewis, S. Das, J. G. Lees, P. Ashford, A. Tolulope, H. M. Scholes, I. Senatorov, A. Bujan, F. Ceballos Rodriguez-Conde, B. Dowling, J. Thornton, C. A. Orengo, CATH: Expanding the horizons of structure-based functional annotations for genome sequences. *Nucleic Acids Res.* **47**, D280–D284 (2019). [doi:10.1093/nar/gky1097](https://doi.org/10.1093/nar/gky1097) [Medline](#)
93. R. D. Finn, T. K. Attwood, P. C. Babbitt, A. Bateman, P. Bork, A. J. Bridge, H.-Y. Chang, Z. Dosztányi, S. El-Gebali, M. Fraser, J. Gough, D. Haft, G. L. Holliday, H. Huang, X. Huang, I. Letunic, R. Lopez, S. Lu, A. Marchler-Bauer, H. Mi, J. Mistry, D. A. Natale, M. Necci, G. Nuka, C. A. Orengo, Y. Park, S. Pesseat, D. Piovesan, S. C. Potter, N. D. Rawlings, N. Redaschi, L. Richardson, C. Rivoire, A. Sangrador-Vegas, C. Sigrist, I. Sillitoe, B. Smithers, S. Squizzato, G. Sutton, N. Thanki, P. D. Thomas, S. C. E. Tosatto, C. H. Wu, I. Xenarios, L.-S. Yeh, S.-Y. Young, A. L. Mitchell, InterPro in 2017-beyond protein family and domain annotations. *Nucleic Acids Res.* **45**, D190–D199 (2017). [doi:10.1093/nar/gkw1107](https://doi.org/10.1093/nar/gkw1107) [Medline](#)
94. S. El-Gebali, J. Mistry, A. Bateman, S. R. Eddy, A. Luciani, S. C. Potter, M. Qureshi, L. J. Richardson, G. A. Salazar, A. Smart, E. L. L. Sonnhammer, L. Hirsh, L. Paladin, D. Piovesan, S. C. E. Tosatto, R. D. Finn, The Pfam protein families database in 2019. *Nucleic Acids Res.* **47**, D427–D432 (2019). [doi:10.1093/nar/gky995](https://doi.org/10.1093/nar/gky995) [Medline](#)
95. L. Jeske, S. Placzek, I. Schomburg, A. Chang, D. Schomburg, BRENDA in 2019: A European ELIXIR core data resource. *Nucleic Acids Res.* **47**, D542–D549 (2019). [doi:10.1093/nar/gky1048](https://doi.org/10.1093/nar/gky1048) [Medline](#)
96. U. Wittig, R. Kania, M. Golebiewski, M. Rey, L. Shi, L. Jong, E. Alga, A. Weidemann, H. Sauer-Danzwith, S. Mir, O. Krebs, M. Bittkowski, E. Wetsch, I. Rojas, W. Müller, SABIO-RK—Database for biochemical reaction kinetics. *Nucleic Acids Res.* **40**, D790–D796 (2012). [doi:10.1093/nar/gkr1046](https://doi.org/10.1093/nar/gkr1046) [Medline](#)
97. E. Akiva, S. Brown, D. E. Almonacid, A. E. Barber 2nd, A. F. Custer, M. A. Hicks, C. C. Huang, F. Lauck, S. T. Mashiyama, E. C. Meng, D. Mischel, J. H. Morris, S. Ojha, A. M. Schnoes, D. Stryke, J. M. Yunes, T. E. Ferrin, G. L. Holliday, P. C. Babbitt, The structure–function linkage database. *Nucleic Acids Res.* **42**, D521–D530 (2014). [doi:10.1093/nar/gkt1130](https://doi.org/10.1093/nar/gkt1130) [Medline](#)
98. S. T. Mashiyama, M. M. Malabanan, E. Akiva, R. Bhosle, M. C. Branch, B. Hillerich, K. Jagessar, J. Kim, Y. Patskovsky, R. D. Seidel, M. Stead, R. Toro, M. W. Vetting, S. C. Almo, R. N. Armstrong, P. C. Babbitt, Large-scale determination of sequence, structure, and function relationships in cytosolic glutathione transferases across the biosphere. *PLOS Biol.* **12**, e1001843 (2014). [doi:10.1371/journal.pbio.1001843](https://doi.org/10.1371/journal.pbio.1001843) [Medline](#)
99. E. Akiva, J. N. Copp, N. Tokuriki, P. C. Babbitt, Evolutionary and molecular foundations of multiple contemporary functions of the nitroreductase superfamily. *Proc. Natl. Acad. Sci. U.S.A.* **114**, E9549–E9558 (2017). [doi:10.1073/pnas.1706849114](https://doi.org/10.1073/pnas.1706849114) [Medline](#)
100. A. Hendler, E. Akiva, M. Sandhu, D. Goldberg, E. Arbely, C. J. Jackson, A. Aharoni, Human SIRT1 multi-specificity is modulated by active-site vicinity substitutions during natural evolution. *Mol. Biol. Evol.* **38**, 545–556 (2021). [doi:10.1093/molbev/msaa244](https://doi.org/10.1093/molbev/msaa244) [Medline](#)

101. L. Fu, B. Niu, Z. Zhu, S. Wu, W. Li, CD-HIT: Accelerated for clustering the next-generation sequencing data. *Bioinformatics* **28**, 3150–3152 (2012). [doi:10.1093/bioinformatics/bts565](https://doi.org/10.1093/bioinformatics/bts565) [Medline](#)
102. S. Mirarab, N. Nguyen, S. Guo, L.-S. Wang, J. Kim, T. Warnow, PASTA: Ultra-large multiple sequence alignment for nucleotide and amino-acid sequences. *J. Comput. Biol.* **22**, 377–386 (2015). [doi:10.1089/cmb.2014.0156](https://doi.org/10.1089/cmb.2014.0156) [Medline](#)
103. I. A. Chen, K. Chu, K. Palaniappan, M. Pillay, A. Ratner, J. Huang, M. Huntemann, N. Varghese, J. R. White, R. Seshadri, T. Smirnova, E. Kirton, S. P. Jungbluth, T. Woyke, E. A. Elie-Fadrosh, N. N. Ivanova, N. C. Kyrpides, IMG/M v.5.0: An integrated data management and comparative analysis system for microbial genomes and microbiomes. *Nucleic Acids Res.* **47**, D666–D677 (2019). [doi:10.1093/nar/gky901](https://doi.org/10.1093/nar/gky901) [Medline](#)
104. N. P. Nguyen, S. Mirarab, K. Kumar, T. Warnow, Ultra-large alignments using phylogeny-aware profiles. *Genome Biol.* **16**, 124 (2015). [doi:10.1186/s13059-015-0688-z](https://doi.org/10.1186/s13059-015-0688-z) [Medline](#)
105. K. Katoh, K. Misawa, K. Kuma, T. Miyata, MAFFT: A novel method for rapid multiple sequence alignment based on fast Fourier transform. *Nucleic Acids Res.* **30**, 3059–3066 (2002). [doi:10.1093/nar/gkf436](https://doi.org/10.1093/nar/gkf436) [Medline](#)
106. M. N. Price, P. S. Dehal, A. P. Arkin, FastTree 2—Approximately maximum-likelihood trees for large alignments. *PLOS ONE* **5**, e9490 (2010). [doi:10.1371/journal.pone.0009490](https://doi.org/10.1371/journal.pone.0009490) [Medline](#)
107. G. Yu, D. K. Smith, H. Zhu, Y. Guan, T. T.-Y. Lam, ggtree: An r package for visualization and annotation of phylogenetic trees with their covariates and other associated data. *Methods Ecol. Evol.* **8**, 28–36 (2017). [doi:10.1111/2041-210X.12628](https://doi.org/10.1111/2041-210X.12628)
108. M. Auton, D. W. Bolen, Application of the transfer model to understand how naturally occurring osmolytes affect protein stability. *Methods Enzymol.* **428**, 397–418 (2007). [doi:10.1016/S0076-6879\(07\)28023-1](https://doi.org/10.1016/S0076-6879(07)28023-1) [Medline](#)
109. A. Peck, F. Sunden, L. D. Andrews, V. S. Pande, D. Herschlag, Tungstate as a transition state analog for catalysis by alkaline phosphatase. *J. Mol. Biol.* **428**, 2758–2768 (2016). [doi:10.1016/j.jmb.2016.05.007](https://doi.org/10.1016/j.jmb.2016.05.007) [Medline](#)
110. L. D. Andrews, J. G. Zalatan, D. Herschlag, Probing the origins of catalytic discrimination between phosphate and sulfate monoester hydrolysis: Comparative analysis of alkaline phosphatase and protein tyrosine phosphatases. *Biochemistry* **53**, 6811–6819 (2014). [doi:10.1021/bi500765p](https://doi.org/10.1021/bi500765p) [Medline](#)
111. P. J. O'Brien, J. K. Lassila, T. D. Fenn, J. G. Zalatan, D. Herschlag, Arginine coordination in enzymatic phosphoryl transfer: Evaluation of the effect of Arg166 mutations in *Escherichia coli* alkaline phosphatase. *Biochemistry* **47**, 7663–7672 (2008). [doi:10.1021/bi800545n](https://doi.org/10.1021/bi800545n) [Medline](#)
112. W. W. Cleland, Partition analysis and the concept of net rate constants as tools in enzyme kinetics. *Biochemistry* **14**, 3220–3224 (1975). [doi:10.1021/bi00685a029](https://doi.org/10.1021/bi00685a029) [Medline](#)
113. S. W. Lockless, R. Ranganathan, Evolutionarily conserved pathways of energetic connectivity in protein families. *Science* **286**, 295–299 (1999). [doi:10.1126/science.286.5438.295](https://doi.org/10.1126/science.286.5438.295) [Medline](#)

114. M. Sjodt, K. Brock, G. Dobihal, P. D. A. Rohs, A. G. Green, T. A. Hopf, A. J. Meeske, V. Srisuknimit, D. Kahne, S. Walker, D. S. Marks, T. G. Bernhardt, D. Z. Rudner, A. C. Kruse, Structure of the peptidoglycan polymerase RodA resolved by evolutionary coupling analysis. *Nature* **556**, 118–121 (2018). [doi:10.1038/nature25985](https://doi.org/10.1038/nature25985) [Medline](#)
115. G. M. Süel, S. W. Lockless, M. A. Wall, R. Ranganathan, Evolutionarily conserved networks of residues mediate allosteric communication in proteins. *Nat. Struct. Biol.* **10**, 59–69 (2003). [doi:10.1038/nsb881](https://doi.org/10.1038/nsb881) [Medline](#)
116. F. Sunden, I. AlSadhan, A. Lyubimov, T. Doukov, J. Swan, D. Herschlag, Differential catalytic promiscuity of the alkaline phosphatase superfamily bimetallo core reveals mechanistic features underlying enzyme evolution. *J. Biol. Chem.* **292**, 20960–20974 (2017). [doi:10.1074/jbc.M117.788240](https://doi.org/10.1074/jbc.M117.788240) [Medline](#)
117. C. Louis-Jeune, M. A. Andrade-Navarro, C. Perez-Iratxeta, Prediction of protein secondary structure from circular dichroism using theoretically derived spectra. *Proteins* **80**, 374–381 (2012). [doi:10.1002/prot.23188](https://doi.org/10.1002/prot.23188) [Medline](#)
118. W. Kabsch, C. Sander, Dictionary of protein secondary structure: Pattern recognition of hydrogen-bonded and geometrical features. *Biopolymers* **22**, 2577–2637 (1983). [doi:10.1002/bip.360221211](https://doi.org/10.1002/bip.360221211) [Medline](#)